Magnetic and structural properties of $CoFe_2O_4$ and $NiFe_2O_4$ thin films and heterostructures

Peter D. B. Mills

PhD

University of York
Physics

December 2022

0.1 Abstract

Thin film heterostructures, combining layers of materials with different magnetic properties, have received high levels of attention as they often exhibit new behaviour not seen in the individual layers. In particular, heterostructures utilizing ferrites have shown modified magnetic properties, and have found applications in spin-filtering magnetic tunnel junctions and insulator spintronics. In this work, we investigate pulsed laser deposition grown $CoFe_2O_4$ (CFO) and $NiFe_2O_4$ (NFO) single films and heterostructures. NFO is of interest due to its large exchange splitting, its ability to form insulating or conducting phases depending on its growth conditions, and the possibility to control its magnetic anisotropy through strain. CFO, on the other hand, exhibits a large positive cubic magnetocrystalline anisotropy constant compared to other ferrites, high magnetostriction, and low conductivity. The difference in the magnetic anisotropy and electronic properties between NFO and CFO, but similar crystal structure, provides the motivation to combine them into a heterostructure. For this purpose, we have studied single films of CFO and NFO as well as bilayers of NFO/CFO and CFO/NFO grown on Al_2O_3 [001] with different thicknesses. Here we present how interfacial effects, such as exchange coupling and strain, affect the magnetic properties and structural properties of single films and heterostructures. Polarised neutron reflectivity (PNR), X-ray reflectivity (XRR), X-ray diffraction (XRD) and vibrational sample magnetometry (VSM) have been used to characterise samples' magnetic and structural properties. Of particular importance, PNR was utilized to measure magnetic profiles as a function of depth across the chemically different layers.

We first study [111] orientated CFO and NFO single films to investigate their growth on the strained ALO substrate and to have reference magnetic properties for later comparison to heterostructures. Both films showed a lower than bulk magnetisation, indicating anti-phase boundaries (APBs) defects play a large role in their magnetisation. A difference in chemical and magnetic profiles between NFO and CFO indicated a differing strength of effect from the ALO [001] interface on the density of APBs .

We have then investigated bilayer samples of [111] orientated bilayers of CFO and NFO. Modified hysteresis loops and coercive field (H_c) values of the bilayers show evidence of exchange coupling. Certain magnetic properties of the bilayers depend on the layer thickness and growth order, i.e. CFO/NFO or NFO/CFO, on the ALO substrate. The measurements show an overall relative increased magnetization of NFO when grown on top of CFO, and depending on the layer order of the bilayer CFO and NFO show different H_c values. The changes in moment imply strain-related effects from the highly lattice mismatched substrate. The changes in Hc can be explained by a combination of strain-related effects, exchange coupling and layer thickness.

0.2 Acknowledgements

Firstly to my two supervisors. I thank Dr Thomas Saerbeck, at times he went above and beyond to help support me and the work in this thesis. His consistency and dedication have played a large part in the success of this project. It has been a pleasure working closely with him in the past 4 years. I thank Prof. Vlado Lazarov for giving me the opportunity of this PhD and continuing to support me throughout. He pastorally supervised my undergraduate degree at the University of York and has been a constant figure in my life for over seven years, for which I am very grateful. I would not have taken this PhD without his guidance.

I would like to thank Dr. Stuart A. Cavill. The samples he grew are the main focus of the thesis and without him, this work would not have been possible. I thank Kalvin Buckley for his support and company during the XRD and XRR measurements. To Didier Dufeu, thank you for your support with the SQUID VSM and for helping ensure I got the measurements I needed.

I'm very grateful to the Institut Laue-Langevin (ILL) for funding this PhD project. It has been an amazing opportunity, and I feel privileged to have spent my PhD there.

To Marta, Angel, Mortiz, Xaver, Antonio, Erik, Aljoša, Palme, Gaccomo, Andrea, Sebastian, Mohammed, and all of my other friends at ILL. I thank you for the help over the years, either through fruitful scientific conversations or by simply going for some beers and helping to unload some stress, I'm truly grateful.

To Claire, thank you for your unwavering support and motivation. You have made my time in Grenoble so much more enjoyable. Merci de tout cœur.

I'd likely to thank my family for supporting me and my quick decision to move countries and live so far away. They have offered nothing but support during my PhD.

To Dad, thank you for your support since the day I was born. You were always a loving and caring father. You encouraged me to take my own path and were proud no-matter what I chose to do. I love you and miss you.

0.3 Declaration

I declare that the work presented in this thesis is based purely on my own research unless otherwise stated, and has not been submitted for a degree in either this or any other university. All sources are acknowledged as references.

List of Tables

List of Figures

Contents

Chapter 1

Introduction

1.1 Motivation and thesis overview

Combining thin films, which host different physical properties, into heterostructures has received high levels of attention as they often exhibit new properties not seen in the individual materials. Heterostructures utilizing ferrites have been discussed for applications in spin-filtering magnetic tunnel junctions [1, 2], insulator spintronics [3–5] and in particular have shown modified magnetic properties [6–8].

In this thesis, we investigate pulsed laser deposition (PLD) grown $CoFe_2O_4$ (CFO) and $NiFe_2O_4$ (NFO) heterostructures. NFO is interesting due to its large exchange splitting, ability to be grown insulating or conducting [9] and its soft ferrimagnetic behaviour [10, 11]. CFO has been selected due to its low conductivity, large magnetostriction and high magneto-crystalline anisotropy constant when compared to other ferrites [12, 13] ($K_1 \approx +20 \times 10^{-5}\,\mathrm{erg/cm^3}$). CFO and NFO are highly suited for growth as heterostructures as they both have inverse spinel crystal structures and almost matching lattice constants (a_{CFO}= 8.383 Å [14] and a_{NFO}=8.346 Å [15]).

The relative hard/soft magnetisations of CFO and NFO make these systems good candidates for exploring the physics of exchange coupling and exchange-spring reversal processes. In these systems, if twice the soft layer thickness (t_s) is less than the hard magnetic Bloch wall length then the two layers are rigidly coupled and nucleate at the same field [16–18]. For larger values of t_s the soft layer is able to nucleate at lower applied fields but remains strongly pinned to the hard layer at the interface, causing a canting of magnetic moments within the layer [19]. Similar ferrite hard/soft heterostructures of CFO and Fe_3O_4 have reported exchange spring behaviour at temperatures of 20 K [20] and 10 K, [21] with a critical soft layer thickness of 80 Å.

In addition to the compatibility of the two materials, the substrate often plays an important role. Depending on the structural mismatch and different growth modes, strain can be observed which can lead to the accumulation of defects and modified properties

overall or near the interface [22, 23]. One such defect is anti-phase boundaries (APBs) which lead to antiferromagnetic coupling between magnetic sublattices [22, 24]. Here, Al_2O_3 [001](ALO) was selected as a substrate due to an 8% mismatch on the O-O sublattice with the [111] plane in NFO and CFO, leading to tensile strain [7, 25]. When grown on a strained substrate both CFO and NFO have been shown to present APBs [1, 7, 13, 26]. It is expected that the AF interactions at APBs will induce very large saturation fields in CFO and NFO [27]. Due to CFOs large polycrystalline saturation magnetostriction constant [12] ($\lambda_s^P \approx -110 \times 10^{-6}$), the 8% lattice mismatch with ALO means there will also be a large stress anisotropy energy contribution [13, 28, 29].

Chapter 1 is split into two main sections. The first outlines fundamental magnetic properties needed to understand the results presented in Chapters 3 and 4. It discusses ferromagnetism and the different types of anisotropies, particularly the ones present in thin films, and the effects of exchange coupling in thin film composite magnetic heterostructures. The second section discusses ferrites. This includes their crystal structure and how this is linked to their magnetism. Specific properties of the ferrites used in this thesis are mentioned. We also discuss some examples of ferrites in composite magnetic structures.

Chapter 2 outlines the techniques we used to characterise our thin films and heterostructures. It is broken down into three main sections. A long discussion of reflectivity, including PNR, details the background physics of the technique and shows how it can be used to characterise magnetic thin films. X-ray diffraction is discussed to explain how we plan to characterise the crystal structures of our samples. The technique of VSM is outlined and how the data from this technique is reduced.

Chapter 3 discusses or initial investigation CFO and NFO single films grown on ALO. Before combining CFO and NFO into bilayers, it was important to have a good understanding of the magnetic and structural properties of the single film growths.

Chapter 4 outlines our investigations into the bilayers of CFO and NFO. In this chapter, we demonstrate how growth in a bilayer, layer thickness, layer order and magnetic exchange coupling has modified the magnetic properties of the films.

Finally, Chapter 5 summarises the work of this thesis and indicates potential future work related to this research.

1.2 Magnetism

In this section, we discuss the important magnetic interactions needed to understand the results presented in this thesis. Magnetism is a well-studied topic and several excellent books exist. The interested reader is directed towards the following references [12, 30–33].

1.2.1 Exchange interaction

Magnetic exchange interaction effects were discovered independently by both Heisenberg [34] and Dirac [35] in 1926. For two atoms situated in close proximity, each having one electron moving about one proton, the electrons are indistinguishable and can exchange places. Classically the atoms should repel each other via electrostatic forces. However, there is an additional energy term due to the electron's spin and the Pauli exclusion principle. This means it is energetically more favourable for two electrons with spin to occupy the same space if the spins are aligned anti-parallel vs parallel. This additional term is known as the exchange energy. If two atoms i and j have spin angular momentum $\mathbf{S}_i h/2\pi$ and $\mathbf{S}_j h/2\pi$ respectively, then the exchange energy between them is given by,

$$E_{ex} = -2J_{ex}\mathbf{S}_i\mathbf{S}_j = -2J_{ij}\mathbf{S}_i\mathbf{S}_j\cos\phi, \tag{1.1}$$

where J_{ex} is the exchange integral, which occurs in the calculation of the exchange effect and ϕ is the angle between spins. If J_{ex} is negative, then E_{ex} is minimised by anti-parallel spins ($\phi = 180$, $\cos\phi = -1$). Interestingly, in certain elements such as Ni, Co and Fe, J_{ex} is positive, meaning E_{ex} is minimised by parallel spins ($\phi = 0$, $\cos\phi = 1$) [36].

1.2.2 Ferromagnetism and anti-ferromagnetism

In a material where the atoms have an overall magnetic moment and where J_{ex} is positive, the alignment of spins leads to an internal magnetic field, known as the molecular field H_m. This field leads to spontaneous magnetisation even without the presence of an externally applied field, H. These materials are classified as ferromagnets.

Despite H_m, all of the spins in a ferromagnet are not always aligned in the same direction. A ferromagnet's magnetisation can break down into domains. A magnetic domain is a region in which the magnetic spins of atoms or molecules are aligned. Each domain is separated by narrow zones called domain walls in which the spins change orientation from one domain to the next. In a de-magnetised state, where there is no applied field, a ferromagnet will present multiple magnetic domains which have no overall orientation. Magnetisation reversal can also lead to domain formation. To create a single domain state where all spins in the ferromagnet are aligned, a saturating field H_S must be applied. At or above H_S a material will present its saturation magnetisation M_s [36]. Magnetisation curves of ferromagnetic iron, cobalt and nickel, are shown in 1.1. It can be seen that both M_s and the magnetisation dynamics are dependent on the specific material.

Another type of magnetic material is an anti-ferromagnet (AMF). AFMs were first discovered by Néel in 1948 [37], and are a class of materials that have local atomic spins/magnetic moments, but due a negative J_{ex}, align anti-parallel, giving the material

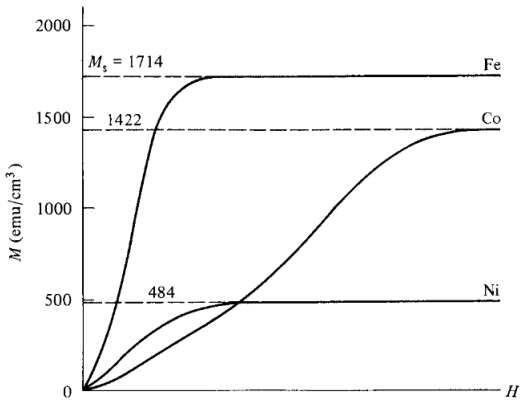

Figure 1.1: Magnetization curves of iron, cobalt and nickel at room temperature [36].

an overall net zero magnetisation.

1.2.3 Magnetic anisotropy

Physical properties of a material which vary as a function of direction are said to exhibit anisotropy. Magnetic anisotropy is the preference of magnetisation in a crystal to lie in a particular crystallographic direction or plane. The preferred direction is referred to as the easy axis, which typically requires lower saturating fields, and has a high remanent magnetisation (magnetisation present at zero field after being magnetically saturated). Directions at some angle away from the easy axis are known as hard magnetic axes, which typically require higher saturating fields and have lower remanent magnetisations compared to the easy axis. The origin of anisotropy in epitaxial thin films is mainly a combination of three effects, magneto-crystalline anisotropy, shape anisotropy and stress anisotropy. More complete descriptions of magnetic anisotropy can be found in the following references [30–32, 38].

Magneto-crystalline anisotropy

Figure 1.2 shows the difference in easy and hard directions for bulk ferromagnetic Fe, Ni and Co. This magnetic anisotropy, which reflects the crystal symmetry, is known as magneto-crystalline anisotropy. This effect is caused by both the crystal field interaction and spin-orbit coupling [30, 31]. We can represent the magneto-crystalline anisotropy of cubic systems as an energy density equation [30],

$$E_c = K_1(M_x^2M_y^2 + M_y^2M_z^2 + M_z^2M_x^2) + K_2M_x^2M_y^2M_z^2 + ..., \tag{1.2}$$

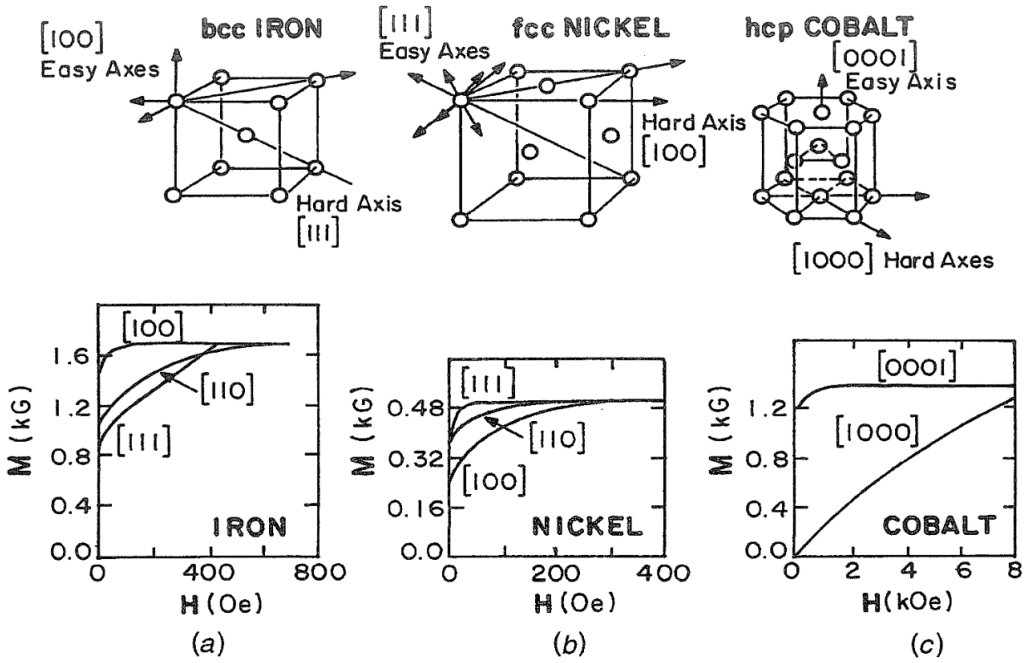

Figure 1.2: Bulk magnetisation in Fe, Co and Ni for applied fields in different directions showing anisotropy [32].

where K_1 and K_2 are anisotropy constants and the magnetisation unit vector is $\mathbf{m} = (M_x, M_y, M_z) = \mathbf{M}/|\mathbf{M}|$. In spherical coordinates this is,

$$E_c = K_1(\frac{1}{4}\sin^2\theta\sin^2 2\phi + \cos^2\theta)\sin^2\theta + \frac{K_2}{16}\sin^2 2\phi\sin^2 2\theta\sin^2\theta + ..., \tag{1.3}$$

where θ and ϕ are angles away from the easy axis. Magneto-crystalline anisotropy constants can be negative or positive values, typically in the range of $10^2 - 10^7$ Jm^{-3} [30].

Stress Anisotropy

Stress anisotropy is related to both the inherent property of a material known as magnetostriction, as well as the amount of stress the crystal is under. Linear magnetostriction was discovered by James Joule in nickel in 1842 [31, 39]. Magnetostriction describes a fractional change in the length of a material in the direction of its magnetisation, given by,

$$\lambda = \frac{\Delta l}{l}. \tag{1.4}$$

The value of λ measured at saturating field is known as saturation magnetostriction, λ_s. During magnetostriction, volume is conserved such that the total linear expansion is $\lambda_\parallel + 2\lambda_\perp = 0$ [31].

A single crystal in a demagnetised state will present magnetostriction along each domain's magnetisation direction, giving a demagnetized magnetostriction constant λ_{si}, sometimes referred to as the polycrystalline magnetostriction constant. When a crystal is magnetised along the $\langle 111 \rangle$ and $\langle 100 \rangle$ directions, this leads to magnetostriction constants in these directions given by,

$$\lambda_{si} = \lambda_{100} + 3(\lambda_{111} - \lambda_{100})(\alpha_1^2\alpha_2^2 + \alpha_2^2\alpha_3^2 + \alpha_3^2\alpha_1^2), \tag{1.5}$$

where α_1, α_2 and α_3 are the direction cosines in a cubic system [40]. These values in, for example, iron are $\lambda_{100} = 15 \times 10^{-6}$ and $\lambda_{111} = -21 \times 10^{-6}$ (the dimensionless unit of 10^{-6} is known as a microstrain) [31, 41].

The existence of magnetostriction means that applied mechanical stress can alter the domain structure and create a new source of magnetic anisotropy [40]. In a thin film, uniaxial stress can be applied via growth on a substrate where the lattice constants of substrate and film are not equivalent. The lattice constant of the film can be compressed (- ive compressive stress) or expanded (+ ive tensile stress) to match the crystal structure of the substrate. The uniaxial anisotropy energy induced in a thin film sample via uniaxial stress, σ, of isotropic magnetostriction ($\lambda_{si} = \lambda_{001} = \lambda_{111}$) is given by,

$$E_\sigma = \frac{3}{2}\sigma\lambda_{si}\sin^2\theta, \tag{1.6}$$

where θ is the angle between the magnetisation and the applied stress.

Depending on the material and crystallographic axis, the magnetostriction constants can have a positive or negative sign. The uniaxial stress can in a crystal be either tensile (+ive) or compressive (-ive). A system with compressive stress and negative magnetostriction would have an energy minimum and subsequent easy axis at 0^o and out-of-plane, but under tensile stress would have an easy axis at 90° in-plane. Therefore, strain anisotropy is dependent on the sign of the strain, the sign of the magnetostriction constant and the magnitude of magnetostriction.

Shape anisotropy

Shape anisotropy derives from a materials demagnetising field. In a uniformly magnetised thin film, the principle components of the demagnetisation field (N_x, N_y, N_z) contributions are (0,0,1), where z is normal to the sample surface. The magnetostatic energy in the z direction is then $-\frac{1}{2}\mu_0 M_S^2$ [31]. This results in a uniaxial shape anisotropy energy for thin films, given by,

$$E_S = \frac{1}{2}\mu_0 M_s^2 \cos^2\theta, \tag{1.7}$$

where θ is the angle between the film normal and M_s [31]. This factor means it is

energetically favourable for the magnetisation of the film to be in-plane [30, 40].

For thin films, there is an additional anisotropy arising from the surface. Surface anisotropy can be explained by the single ion theory [40] i.e. the coupling of surface atoms to the crystal field produced by their surroundings. This effect imposes a strong out-of-plane anisotropy but decays with $1/t$ where t is the film thickness, and so it is strongly felt in films below 10 Angstroms.

1.2.4 Exchange coupling effects in composite magnetic systems

A broad range of composite systems such as nanoparticles, nanowires and noncomposite magnetic thin films are studied for their surface and interface-induced exchange interactions [42–44]. Exchange coupling between materials has led to advanced permanent magnet applications [45], applications in spin filtering and magnetic tunnel junctions [7] and enhancements in the spin Seebeck effect [46]. Thin film magnetic multi-layers are particularly important as they are components of magnetic memories (e.g. magnetic random access memory) or sensors, systems which are important to the field of spintronics [47]. Exchange coupling in magnetic ferrite heterostructures have been studied in recent years as epitaxial bilayers [7, 20, 21] and in all oxide spin tunnel junctions [48–50]. Understanding exchange coupling in ferrite heterostructures will be crucial for the use of these materials in future devices and magnetic memories, for example.

Composite magnet systems were initially proposed to overcome the limits of permanent magnet systems. The quality of a permanent magnet is measured by its product $(BH)_{max}$, in effect, the largest area of a rectangle enclosed by its hysteresis loop. Kneller and Hawih [16] proposed to take hard magnets, which have a large anisotropy constant but typically lower M_s, and exchange couple them with a soft magnet, which has a small anisotropy constant but large M_S, to create a better permanent magnet with a larger $(BH)_{max}$. These magnets are known as exchange spring or exchange hardened magnets.

Several approaches have been applied to exchange coupled systems to relate key parameters such as layer dimensions, relative volume fractions and geometry of the soft and hard phases to the systems magnetisation, nucleation field and $(BH)_{max}$. They include deriving analytical expressions [42, 51], micromagnetic modeling [52], as well as first-principle calculations [53]. They find that a critical soft layer thickness exists, below which the soft layer is rigidly coupled to the hard layer. This thickness is found to be roughly twice the width of a domain wall, δ_k, in the hard phase [16, 42, 52],

$$\delta_h = \pi\sqrt{\frac{A_h}{K_h}}, \tag{1.8}$$

where A_h and K_h are the hard phase exchange and anisotropy constants, respectively.

Exchange coupling below the critical soft layer thickness

For exchange-coupled systems where the soft layer is less than δ_h, both layers nucleate at the same field during magnetisation reversal, but with a modified hysteresis loop when compared to the individual layers. Fullerton et all [19, 54, 55] performed experiments on single film Sm-Co and Sm-Co/Fe bilayer systems with varying Fe layer thickness, grown on MgO [110]. They performed vibrating sample magnetometry (VSM) measurements with H in-plane along the Sm-Co [001] easy axis direction, shown in figure 1.3. The Sm-Co single layer shows the expected square loop of a hard magnet. After adding a 25 Å layer of Fe, the sample showed a significant reduction in H_c but remained a square loop, indicating that these layers are strongly coupled and below the critical soft layer thickness.

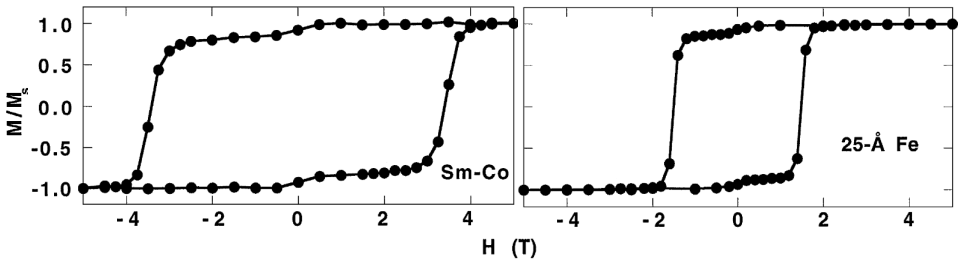

Figure 1.3: Room temperature hysteresis loops of a single Sm-Co film and Sm-Co/Fe bilayer [55].

The reduction in H_c shows that in rigidly coupled systems, magnetic properties still show a dependence on the material parameters of both layers. The H_c of a rigidly coupled system can be roughly predicted by the following equation,

$$H_c = \frac{2(t_h K_h + t_s K_s)}{t_h M_h + t_s M_s}, \tag{1.9}$$

where K_s is the soft layer anisotropy constant and t_h, t_s, M_h and M_s are the soft layer and hard layer thicknesses and saturation magnetisation, respectively [19].

Exchange coupling above the critical soft layer thickness

For systems where the soft layer is above the critical thickness, the two layers are not rigidly coupled, but the soft phase still cannot nucleate freely. Fullerton et al. studied Sm-Co/Fe bilayers of Fe layer thickness 200 Å [19, 54, 55], above the critical soft layer thickness for these systems. Their VSM measurement is shown figure 1.4. The square-shaped hysteresis of the hard phase has been lost and is replaced by a two-step hysteresis loop. The behaviour of the two magnetic layers during this loop can be described, as follows. Starting from $H = 0$, after saturation at a positive field, figure 1.4 a) shows the maximum applied field for which the soft layer remains parallel to the hard layer, called

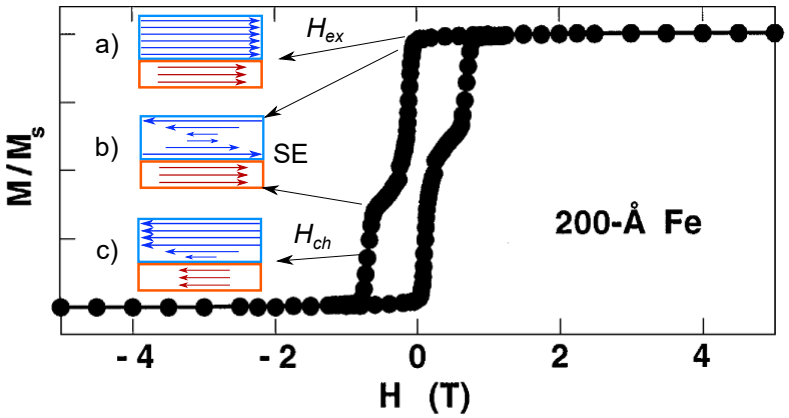

Figure 1.4: Room temperature magnetic hysteresis loop for a bilayer film of Sm-Co/Fe, with 200 Å of Fe. a) The two layers are rigidly coupled below H_{ex}. b) The soft layer is able to nucleate toward H, but is exchange coupled to the hard phase at the interface, resulting in an exchange spring interaction. c) H is now large enough to nucleate the hard phase, resulting in irreversible nucleation [55].

the exchange field $H = H_{ex}$. Assuming no soft phase anisotropy, this field is given by [51],

$$H_{ex} = \frac{\pi^2 A_s}{2 M_s t_s^2}, \tag{1.10}$$

with calculations including a finite soft layer anisotropy finding that the H_{ex} scales as $t_s^{-1.75}$ [52]. For fields larger than H_{ex}, the soft layer is still strongly pinned at the hard layer interface, but the magnetisation of the soft layer twists towards the applied field, shown in figure 1.4 b). This twisting behaves like a Bloch wall, with the angle of rotation increasing with distance from the hard phase interface. At this point, the hard phase is unaffected and the magnetisation of the system is completely reversible. This stage is known as an exchange spring interaction (ES) due to the spring-like twisting of the magnetisation in the soft layer. Once a sufficiently large field is applied H_{ch}, the hard layer begins to rotate irreversibly shown in figure 1.4 c).

Critical Bloch wall thickness

One solution for the critical soft layer thickness by Kneller and Hawih [16] is useful as it can be extended to an effective critical Bloch wall thickness in a soft layer for which the hard phase will begin to rotate irreversibly. Figure 1.5 a) shows along a z-axis, a hard and soft layer of length t_h and t_s, respectively, at remanence following saturating field. These materials are assumed to be magnetic single crystals, exchange coupled at the interface. The magnetocrystalline anisotropy will be assumed uniaxial, for simplification, in both phases. The easy direction is along the x-axis, perpendicular to z. The equation for

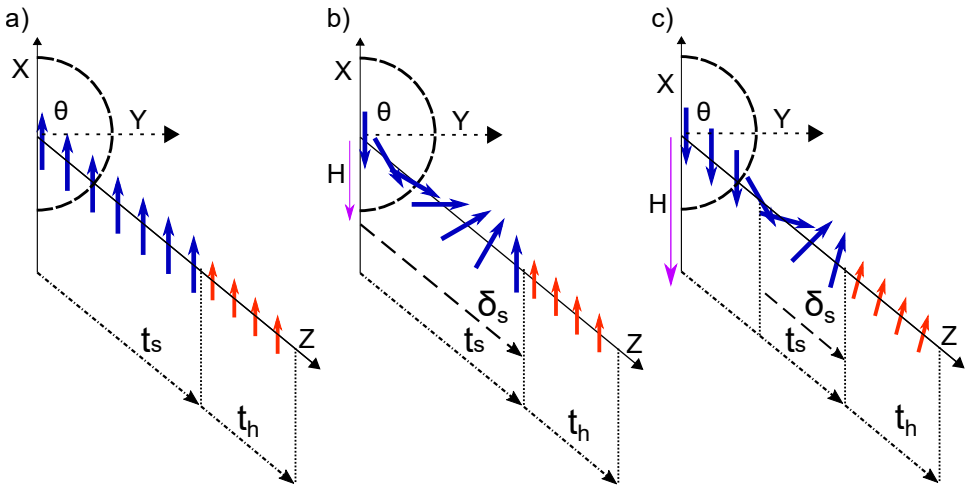

Figure 1.5: Ideal exchange-spring system showing a soft layer (blue) of length t_s and hard layer (red) of length t_h. a) Shows the system at remanence, b) with a small applied H creating a 180^o wall of length δ_m, and c) shows a H above the critical H_c field, compressing δ_m and rotating the hard layer.

uniaxial anisotropy energy density is,

$$E_k = Ksin^2\theta, \tag{1.11}$$

where θ is the angle between the magnetisation and the easy axis [31] and $K > 0$ so that the spins prefer to align along 0 and π. It should be noted that the ratio of K_h/K_s is of the order of 10^2 while M_h/M_s does not typically exceed 10 [16].

The exchange energy density is given by,

$$E_A = A(\frac{d\theta}{dx})^2, \tag{1.12}$$

where A is the exchange constant, which represents the effect of ferromagnetic exchange coupling between spins within the film, typically of the order 10^{-11} J/m.

Using equation 1.11 and 1.12, the energy per unit area of a 180^o Bloch wall in a homogeneous material is approximately,

$$\gamma \approx \delta K + \delta A(\frac{\pi}{\delta})^2, \tag{1.13}$$

where δ is the wall thickness [16]. This equation is essentially the Gibbs free energy per unit area of the wall, described also by Goto et al. [51], but neglecting the Zeeman energy $H \cdot J_s$, where J_s is the spontaneous polarisation of the ferromagnet. In equilibrium equation 1.13 is minimised by $d\gamma/d\delta = 0$, giving equilibrium values of

$$\delta_0 \approx \pi(\frac{A}{K})^{\frac{1}{2}}, \tag{1.14}$$

and

$$\gamma_0 \approx 2\pi(A \cdot K)^{\frac{1}{2}}. \tag{1.15}$$

We assume the hard layer is reasonably long i.e. $t_h \approx \delta_{0k} = \pi\sqrt{(A_h/K_h)}$ [16]. An in-plane field $H \leq 0$ is applied along the easy axis, causing the soft phase to rotate reversibly. At the beginning of the rotation, a 180^o wall will form in the soft layer, shown in figure 1.5 b). As H is decreased, this wall will be compressed toward the hard layer boundary. This decrease in the soft layer wall size increases its energy density $E_{\gamma s} = \gamma_s/\delta_s$. The hard phase will be relatively unchanged as $K_h \gg K_s$. The soft layer wall will continue to shrink with decreasing H until $E_{\gamma s}$ reaches the equilibrium energy of a wall in the hard layer [16],

$$E_{\gamma s} = \frac{\gamma_s}{\delta_s} = E_{\gamma 0h} = \frac{\gamma_{0h}}{\delta_{0h}} = 2K_h. \tag{1.16}$$

The critical soft layer wall thickness, δ_{cs}, where the hard layer will begin to rotate can be calculated. Using equation 1.13, the energy density of δ_{cs} is $E_{\gamma s} = K_s + \pi A_s/\delta_{cs}^2$, which when compared to $E_{\gamma 0h}$ gives

$$\delta_{cs} = \pi\sqrt{\frac{A_s}{2K_h}} \tag{1.17}$$

where $(K_h - K_s) \approx K_h$, meaning a vanishing soft layer anistropy is assumed. This result neglects the Zeeman energy term $H \cdot J_s$ and other analytical results arrive at a slightly different critical δ_{cs} of twice the width of the hard layer domain wall thickness given by $\delta_h = \pi\sqrt{A_h/K_h}$ [42, 51, 52]. Despite these issues, the result is similar to other calculations and importantly for us, relates the width of the soft-phase Block wall δ_s to the hard layer anisotropy constant.

Spring exchange soft layer thickness dependence

There is no direct solution which can predict the hard layer nucleation field H_{ch} of a hard magnet in an exchange spring system. Leineweber and Kronmüller attempt to indirectly analyse the dependence of H_{ch} against soft layer thickness [52]. They introduced the reduced field,

$$h \equiv \frac{H}{H_{ch}^0} = \frac{HJ^h}{2K^h}, \tag{1.18}$$

where H_{ch}^0 is the ideal nucleation field of the hard-magnetic material, H is the measured nucleation field and $K^h \equiv K_h$. In the equation, the field is restricted to $-1 < h < 0$. The indirect analysis showed that the magnetisation reversal exhibits a functional dependence

of the soft layer thickness $d_s \equiv d^s$,

$$h(2d^s) = \begin{cases} H^0_{ch}\,(\text{hard magnetic}), & \text{for } 2d^s \leq \pi\delta^h, \\ \text{rapid decrease}, & \text{for } \pi\delta^h < 2d^s < 8\pi\delta^h, \\ \propto (2d^s)^{-1.75}, & \text{for } 2d^s > 8\pi\delta^h, \end{cases} \tag{1.19}$$

where $\delta^h \equiv \delta_h$. These results were plotted for a hard/soft/hard α-Fe/Nd_2Fe_{14} sandwich in figure 1.6. They show that in exchange spring systems, the nucleation field of the hard layer is extremely sensitive to soft layer thickness variations on the length scale of a hard phase domain wall.

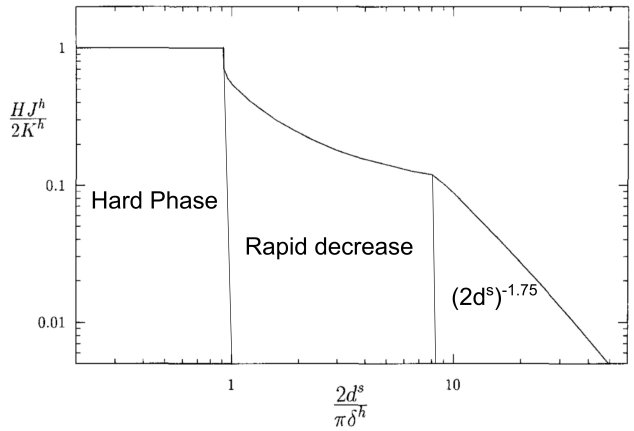

Figure 1.6: Reduced field of a hard/soft/hard α-Fe/Nd_2Fe_{14} magnetic thin film sandwich vs soft layer thickness. The thickness is given in units of the hard magnetic Bloch wall thickness, plotted against the nucleation field in units of the ideal hard magnetic nucleation field [52].

1.2.5 Exchange bias

Exchange bias is not observed in this thesis, but is important to the field of exchange coupling and so is discussed. In 1965 Meiklejohn and Bean reported a unidirectional anisotropy in FM/AFM Co/CoO nanoparticles [56, 57], which would later be known as exchange bias (EB). In these AFM/FM structures, the FM orders at the Curie temperature, T_C, which is greater than the Néel temperature, T_N of the AFM. If a field is applied to the system when it is between $T_C > T > T_N$ then the FM will align to the field, while the AFM remains paramagnetic. As the system is cooled to below T_N, the ordering net localized AFM spins will couple to the aligned FM spins, sharing their general alignment. Assuming the AFM has a high magnetocrystalline anisotropy, the AFM spins at the interface will not change their alignment direction due to applied fields [58]. The localized uncompensated AFM spins are exchange coupled to the FM spins at the interface and exert a strong torque, aligning the FM spins to the direction of the cooling field. The effect of this coupling can be seen in figure 1.7, with the EB system presenting an asym-

metry along the field axis of the hysteresis loop [59], characterized by the exchange bias field H_E.

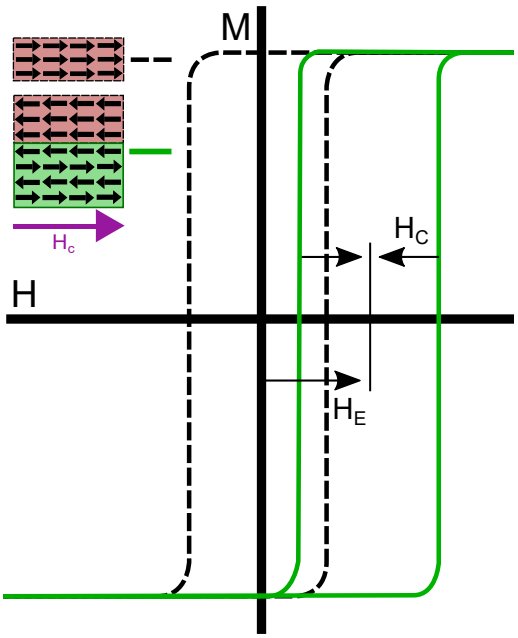

Figure 1.7: Dashed line shows a hysteresis loop of a normal ferromagnet. The green line shows the hysteresis loop for a FM/AFM heterostructure after field cooling through T_N, with a clear unidirectional anisotropy. The exchange bias field H_E and the coercivity H_C are given in the figure.

Exchange bias systems are still keenly investigated today due to their intrinsic complexity [60], applications in magnetic read heads and a potential future application in magnetic random access memory [61]. Various parameters have been studied to investigate their effect on EB systems, such as annealing temperature [62], AFM layer thickness [63], bulk properties [64], cooling field strength [65] and crucially interface roughness [66, 67]. Magnetic thin films are useful systems for exploring the physics of exchange bias materials as modern deposition techniques offer a high degree of control over the interface region where exchange coupling occurs. Understanding the exact mechanism of exchange bias remains a challenge as models of the phenomenon have failed to correctly predict the experimental observations of EB and coercivity [68]. Due to the complexity of EB, we discuss here only some key experiments, many more complete and useful resources on EB can be found elsewhere [59, 60, 69–71].

Multiple theoretical studies have been performed to explain the effects of interfaces and roughness on EB. Some studies have focused on how, as layered single-crystal structures, EB can be affected by crystal interface effects such as lattice mismatch, strains and defects [72, 73]. Others discuss the contribution of magnetic frustration associated with the interface in EB systems [74]. This frustration is principally caused by either uncompensated spins and/or interface roughness [71, 72]. It has also been suggested that

magnetic structures in the vicinity of the interface are not necessarily identical to the bulk magnetic ordering [75], affecting the EB system. Generally for oxide AFM systems, the trend is such that increasing interfacial roughness leads to a weaker H_E [59], however a complete theoretical model of EB that is able to accurately predict both H_E and H_c of a given FM/AFM system does not exist.

The lack of a theoretical model capable of predicting H_E and H_c of a given FM/AFM system as well as experimental studies highlighting the susceptibility of EB to interface roughens clearly demonstrates the need for more investigations.

1.3 Ferrites

Ferrites are a versatile group of materials which have attracted large attention in recent years due to a broad range of magnetic and electronic properties. In particular, their high Curie temperatures (T_C) and chemical stability make them popular choices for device applications. The very large resistance of ferrites means they do not produce significant eddy currents, making them promising candidates for high-frequency devices where power loss from eddy currents is minimized. Ferrites have been utilised in spintronics [1, 2, 9, 76–80], microwave devices [81] and magnetic field sensors [82].

Ferrites can show large changes to their electronic and magnetic properties due to various factors such as growth conditions, strain, and annealing. This can be seen as both useful and an obstacle. On the one hand, this means it is possible to tune the magnetic properties of ferrites, but on the other, it can often mean that these properties vary significantly. In this section, we discuss the crystal structure of ferrites and how this is linked to their magnetic properties, including the ferrites used in this thesis.

1.3.1 Crystal structure

The magnetic ferrites fall into two groups with different crystal structures [12]:

- *Cubic*. These are generally defined by XFe_2O_4, where X is a divalent metal ion like Mg, Co, Ni, Fe etc.
- *Hexagonal*. Some important examples are $BaO{\cdot}6\ Fe_2O_3$ and $SrO{\cdot}6\ Fe_2O_3$ which are magnetically hard.

The work presented here focuses solely on the cubic ferrites. Cubic ferrite materials share the spinel crystal structure (space group: $Fd\bar{3}m$). The spinel structure is large, containing eight formula units with 56 ions per unit cell, 32 O^{2-},16 Fe^{3+} and 8 X^{2+}. Oxygen ions form a face-centred cubic (FCC) sublattice, with the metal ions distributed in tetrahedral (A) and octahedra (B) interstitial sites. The crystallographic environments

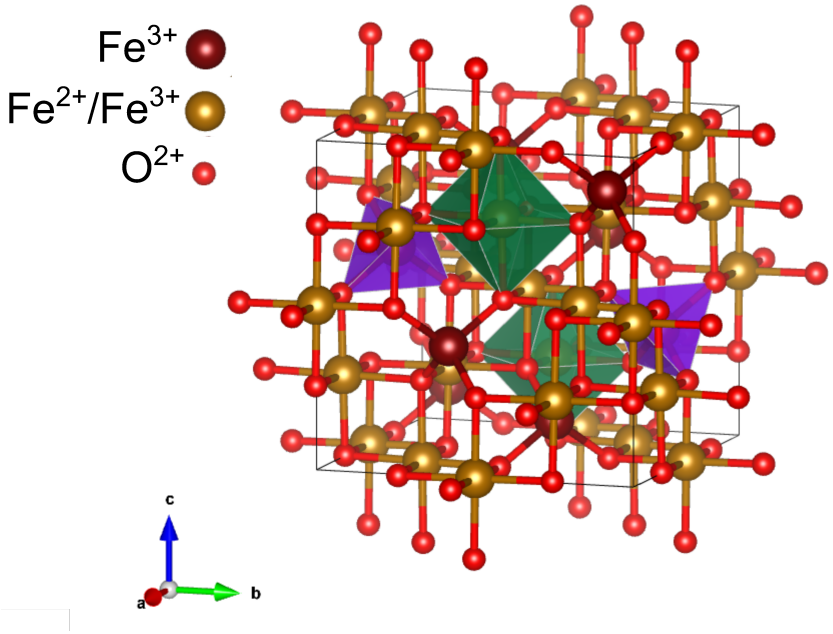

Figure 1.8: Inverse spinel crystal structure of Fe_3O_4 [86], with purple and green polyhedra showing tetrahedral (A) and octahedral (B) and interstitial sites, respectively. This figure was created using the VESTA software package [87].

of the interstitial sites are quite different. For a normal spinel, all the Fe^{3+} ions are in B sites and all X^{2+} ions are in A sites. The inverse spinel structure exists, where 1/8 of the A sites are occupied by the Fe^{3+} ions and 1/2 of the B sites are occupied equally by Fe^{3+} and X^{2+}. The general formula of the spinel structure is given by $[Fe_yX_{1-y}]_A[Fe_{2-y}X_y]_B$ where y is the inversion parameter [49]. Under certain conditions, it's possible for these trivalent ions to move between interstitial sites, creating intermediate states between normal and inverse spinel structures, modifying a ferrite's magnetic and electronic properties [83–85]. The structure of the inverse spinel Fe_3O_4 is shown in figure 1.8. The lattice parameters of cubic ferrites are typically similar, with 8.397 Å for Fe_3O_4 [86], 8.383 Å for $CoFe_2O_4$ [14] and 8.346 Å for $NiFe_2O_4$ [15].

1.3.2 Magnetic interactions in the crystal

Ferrites are ionic compounds, whose magnetic properties arise from the metal ions, as the O^{2-} ion has no net moment. The expected magnetisation of one formula unit (F.U.) of $CoFe_2O_4$ using Hund's rule is $3\,\mu_B$/atom from Co plus $5\,\mu_B$/atom per Fe, giving $13\,\mu_B$ per F.U.. When you compare CFO's magnetisation by adding the moment per atom to the measured bulk CFO M_s value of $3.3\,\mu_B$/F.U. [88], the per-atom calculation is much higher. This is because $CoFe_2O_4$ along with Fe_3O_4 and $NiFe_2O_4$ are ferrimagnetic. The magnetic ordering of these systems arises from several exchange couplings between the different cations [31]. Super exchange takes place between the Fe^{3+} and the X^{2+} ions via an overlap of their 3d orbitals with the 2p orbitals of an intermediate oxygen O^{2-}

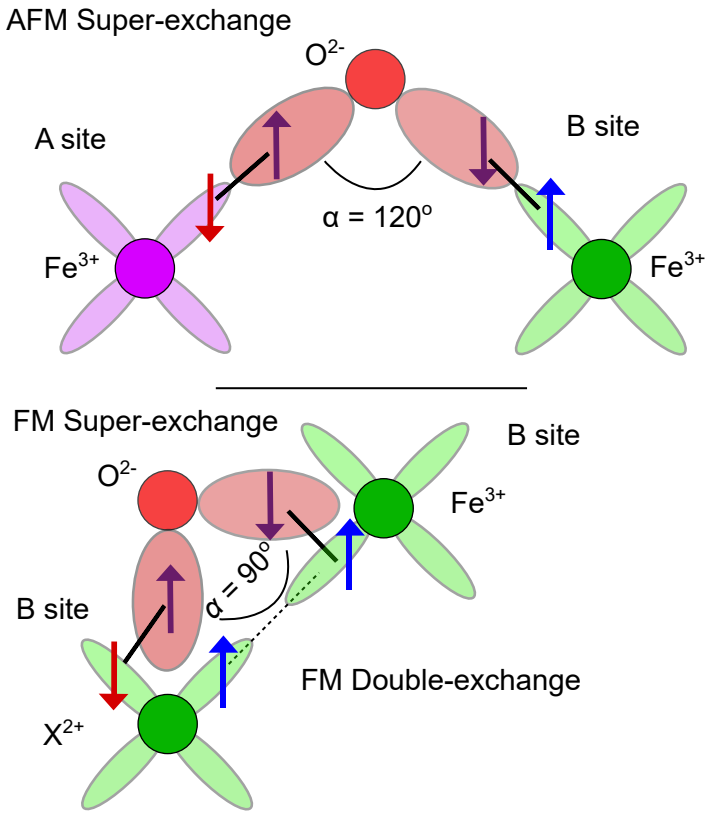

Figure 1.9: Super exchange interactions between A sites and B sites mediated via an O^{2-} ion. At $\alpha = 120°$ the interaction between A sites and B sites is AFM. At $\alpha = 90°$ the interactions between B sites is FM [49].

[49, 89–91]. If the angle between the two ions is more than 90^o then the interaction is AFM, whereas if the angle is equal to 90^o then the interaction is FM. Double exchange is also present, via the transfer of one electron from the X^{2+} ion, to the empty d-level in the Fe^{3+} ion. Double-exchange is weak and often masked by the FM super-exchange interaction [49]. Both Super-exchange and double exchange are shown in figure 1.9. The total interactions are as follows [49, 91]:

- The strong AFM super-exchange between A and B sites of energy $J_{AF} = -24k_B$.
- AFM super-exchange involving only Fe_A^{3+} cations via an O^{2-}A of energy $J_{AF} = -19k_B$.
- FM super-exchange interaction between B sites of energy $J_F = 4k_B$.
- Weak direct FM double-exchange between B sites.

The net magnetic moment per F.U. is calculated by adding up all of these interactions. For a perfect inverse spinel, the $5\mu_B$ of the $Fe_{A:B}^{3+}$ interactions are AFM, meaning the moment is determined by the X^{2+} ion [49]. The theoretical maximum moments of $NiFe_2O_4$, $CoFe_2O_4$ and Fe_3O_4 are $2\,\mu_B$/F.U., $3\,\mu_B$/F.U. and $4\,\mu_B$/F.U., respectively.

Antiphase boundaries in ferrites

An antiphase boundary (APB) separates two domains of the same ordered phase [92]. It results from symmetry breaking that occurs during ordering processes, which can start at different locations in a disordered lattice. An APB forms when two such regions contact so that they display wrong compositional bonds across the interface [93], shown in figure 1.10. APBs in ferrites lead to 180° super-exchange interactions, coupling adjacent domains antiferromagnetically [94], which can lead to extremely large saturating fields [27].

The formation of APBs in ferrite thin films can be a consequence of either higher symmetry of the substrate than the ferrite, leading to a large number of nucleation sites for film growth, or accommodation of misfit dislocations arising due to a large lattice mismatch [27, 95, 96]. APBs have been directly observed in thin film Fe_3O_4 [97].

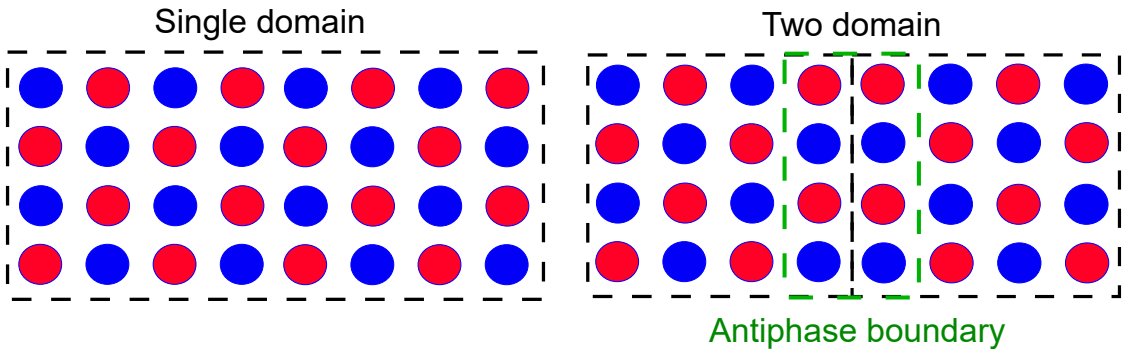

Figure 1.10: Single and two domain two-dimensional crystals. The two domain crystal presents an anti-phase boundary at the domain interface.

1.3.3 Materials

Here we discuss the magnetic and electronic properties of $CoFe_2O_4$, Fe_3O_4 and $NiFe_2O_4$.

$CoFe_2O_4$

A large amount of research is focused on $CoFe_2O_4$ (CFO) due to its large magnetocrystalline anisotropy constant when compared to other cubic ferrites ($K_1 \approx +20 \times 10^{-5}\,\mathrm{erg/cm^3}$) [12, 13], and large demagnetised magnetostriction constant [12, 98] ($\lambda_{si}^{P} \approx -110 \times 10^{-6}$), with single crystal magnetostricion constants of λ_s^{100}=(-223 to -590) and $\lambda_s^{111} \approx -1/5\lambda_s^{100}$ [99]. CFO presents an experimentally measured bulk magnetisation of $3.70\,\mu_B$/F.U.[12] and a magnetic easy axis in the [001] direction [98]. Inverse spinel CFO is insulating. Its electronic properties have been simulated by density functional theory [100] showing CFO has a theoretical band gap of 0.80 eV and presents exchange splitting ($2\Delta E_{ex}$) of 1.28 eV.

Several experiments have demonstrated control of CFO's magnetic properties in thin films via growth conditions, layer thickness [101, 102] and strain-induced anisotropy [26, 81, 103–108]. Typical choices of substrates are MgO, $SrTiO_3$ and Al_2O_3. The ability to modify CFO's magnetic properties makes it an interesting candidate to study in a single film system.

Fe_3O_4

Fe_3O_4 has not been studied in this thesis, but it's an important ferrite and so is discussed. This material is a soft ferrimagnet with one of the largest theoretical magnetisations of the cubic crystal ferrites, 4 μ_B/F.U.. It is a predicted half metal [100, 109], meaning it has 100% spin polarisation at the Fermi energy level. This material property has large potential applications in spintronics, for example, as a replacement for Fe in Fe/MgO magneto-tunnel junctions [110] (MTJs). Experimentally measured spin polarisation is always much lower [78, 79]. This decreased polarization is primarily accredited to the presence of crystal defects such as APBs and surface reconstruction [23, 24, 97].

Fe_3O_4 presents a phase transition below $\approx 130\,K$ leading to changes in its crystal structural (cubic to monoclinic), magnetic, electronic (half-metallic to insulating) and thermal properties [111–113] known as the Verwey transition.

This combination of half-metallicity, along with a temperature dependant Verwey transition, makes Fe_3O_4 an interesting candidate to study in magnetic heterostructures.

$NiFe_2O_4$

Inverse spinel $NiFe_2O_4$ (NFO) is typically a soft ferrimagnetic insulator. Bulk NFO has an experimentally measured magnetisation of $2.3\mu_B$/F.U. [12], cubic mangetocrystalline energy constant of $K_1 = -6.8\times10^{-6}\,\mathrm{erg/cm^3}$ and magnetic easy axis in the [111] direction [114]. Bulk NFO has single experimentally measured crsytal mgnetostrction constants $\lambda_{111} = -3.4 \times 10^{-6}$ to -9.7×10^{-6} and $\lambda_{100} = 35.9 \times 10^{-6}$ to -44.3×10^{-6} [115].

NFO's electronic properties have been simulated by density functional theory [100], finding NFO has a band gap of 0.98 eV and exchange splitting of 1.21 eV. Interestingly, experimental results have shown that ultra-thin NFO can be grown to be either insulating or conducting depending on the growth conditions [9]. In thin films, NFO's magnetic properties have been shown to be altered by strain, temperature, oxygen vacancies, cation inversion, APBs and twinning [95, 116, 116–121].

NFO's growth dependent magnetic and electronic properties make it an exciting candidate to investigate in both single films and in magnetic heterostructures.

Composite magnetic ferrite systems

Both CFO's and NFO's magnetic and electronic properties have led to the exploration of these ferrites in more complex magnetic systems. CFO has been used as a hard magnet to give a strong unidirectional exchange biasing on soft ferrite films [122]. Single film CFO has shown exchange bias via a suspected CoO layer in single film growth [123]. Inter-layer coupling between $Co_xFe_{1-x}O_4/Fe_3O_4$ and Fe_3O_4, separated by an insulating MgO layer, has been demonstrated [124]. CFO's large exchange splitting has led to experiments involving spin filtering, with several examples of room temperature devices [1, 76, 77]. Ferrite hard/soft heterostructures of CFO and Fe_3O_4 have been studied, showing exchange spring behaviour at temperatures of 20 K [20] and 10 K, [21] with a critical soft layer thickness of 80 Å. NFO exchange bias systems have shown promise for use in electric-field-control spintronic devices [125]. NFOs exchange splitting has led to large interest in use for spin-filtering devices [2, 9, 80] with Lüders *et al* [9] demonstrating two tunnelling magneto-resistance junctions using either insulating or conducting NFO. Despite the high level of interest in CFO and NFO, there has been no investigations into the magnetic or structural properties of combined CFO/NFO heterostructures.

Chapter 2

Methodologies

2.1 Thin films

Using thin films (on the order of less than a few 100 nm) as samples allow for several advantages. Thin film sample growths can be performed via physical vapour deposition techniques such as molecular beam epitaxy (MBE) or pulsed laser deposition (PLD). PLD has a slow deposition rate (<3000 nm/hour) which allows for epitaxial or highly crystalline growth [126]. Depositions are performed at high vacuum (HV, 10^{-8} mbar) greatly lowering the number of impurities in the sample. Thin films can be grown directly on top of each other, allowing for the growth of heterostructures. Substrates can be used to select the crystallographic orientation of film growth. Depending on the structural mismatch between films and substrate, strain can be observed which can lead to the accumulation of defects and modified properties overall or near the interface [22, 23]. More complete descriptions of MBE and PLD can be found in the following references [126–128].

All CFO and NFO films and bilayers have been grown using PLD at the University of York, School of Physics, Engineering and Technology by Dr. Stuart A. Cavill. A partial O_2 pressure of $3x10^{-5}$ mbar was used during all growths. To make the samples, metal-oxide NFO or CFO PLD targets have been used. Both CFO and NFO targets were prepared by sintering. Targets were rastered and rotated during ablation. Al_2O_3 [001](ALO) was selected as a substrate due to an 8% mismatch on the O-O sublattice with the [111] plane in NFO and CFO, leading to tensile strain [7, 25]. The substrates were heated to 500 °C in a partial O_2 pressure before, during and 20 minutes after growth. The laser source was a Nd:YAG laser, where the 4th harmonic was used to produce a 266 nm wavelength. The laser's repetition rate, energy density and distance between the target and substrate were maintained at 10Hz, 1 J/cm^2 and 150 mm.

2.2 Polarized neutron reflectivity

Magnetic neutron scattering is a bulk probe which is particularly useful in the investigation of spintronics and magnetic thin films. Polarised neutron reflectometry (PNR) probes the nuclear and magnetic profiles as a function of depth. This is due to both the wavelength of cold neutrons matching the thickness of thin films and the natural magnetic moment in neutrons. For magnetic thin films and multilayers, PNR can be used to characterise individual layer thickness, roughness, and magnetisation. It is this ability to probe magnetic profiles that distinguishes PNR from other magnetometry techniques such as vibrating sample magnetometry (VSM) which only measures the bulk volume magnetisation or the Magneto-optic Kerr effect (MOKE) which is only sensitive to magnetisations at a limited depth.

Various complete descriptions of polarised neutron reflectivity exist [37, 129–133]. Here we present the important theoretical results, alongside numerical simulations, to describe how we have used this technique to characterise magnetic thin film systems.

Scattering length

For neutrons, scattering occurs at the nucleus of an atom via the strong force. This scattering is isotropic in nature due to the difference in wavelength of thermal neutrons vs the strong interaction (10^{-10} vs 10^{-14}). The amount neutrons are scattered by a given element or isotope is given by the one-dimensional property scattering length, b_l^n (in fm). For nuclei where neutron absorption is likely, such as ^{103}Rh, ^{113}Cd or ^{157}Gd, the scattering length is complex and varies with wavelength due to resonant effects. In most cases b_l^n is invariant with λ. Figure 2.1 shows how scattering length varies by element, demonstrating that there is no real trend between neutron scattering length and element [134].

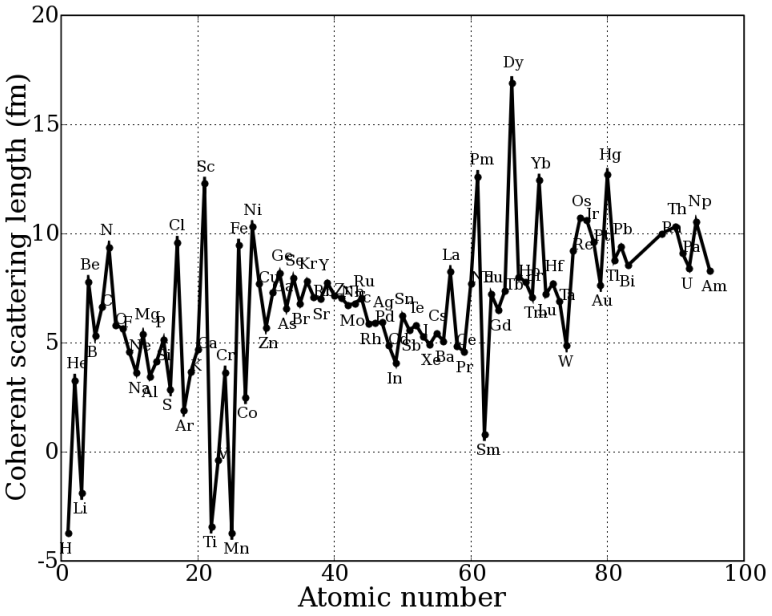

Figure 2.1: Coherent scattering lengths vs atomic nuclei [135]

For X-rays, scattering occurs via electromagnetic interactions with the orbital electrons. This means the scattering depends on the number of electrons (and therefore protons) of the atom and the area they occupy. For our experiments, we assume the scattering angles are sufficiently small such that the atoms behave as dipoles and therefore the form factor is independent of the angle [136]. The X-ray form factor for a collection of atoms needs to be modified by a correction term (a real number) dependent on the proximity of the impressed wavelength to the natural resonant frequency of the system and a loss term (an imaginary number) that is related to the damping factor for the resonant system [137], known as dispersion corrections. This gives a form factor,

$$f(\lambda, Z) = Zr_e + \Delta f'(\lambda, Z) + i\Delta f''(\lambda, Z), \tag{2.1}$$

where Z is the atomic number, r_e is the classical radius of the electron , $\Delta f'(\lambda, Z)$ is the real part of dispersion correction, and $\Delta f''(\lambda, Z)$ is the imaginary dispersion correction [136, 137]. Scattering lengths are then separated into real $b_l^x = Zr_e + \Delta f'(\lambda, Z)$ and imaginary components $b_l^i = i\Delta f''(\lambda, Z)$, and calculated from known tabulated values of the dispersion corrections for a given element and wavelength [137].

The difference in scattering location for X-rays and neutrons often leads to contrast between b_l^n and b_l^x, making it complementary to measure the same technique with both probes.

2.2.1 Grazing incidence scattering geometry

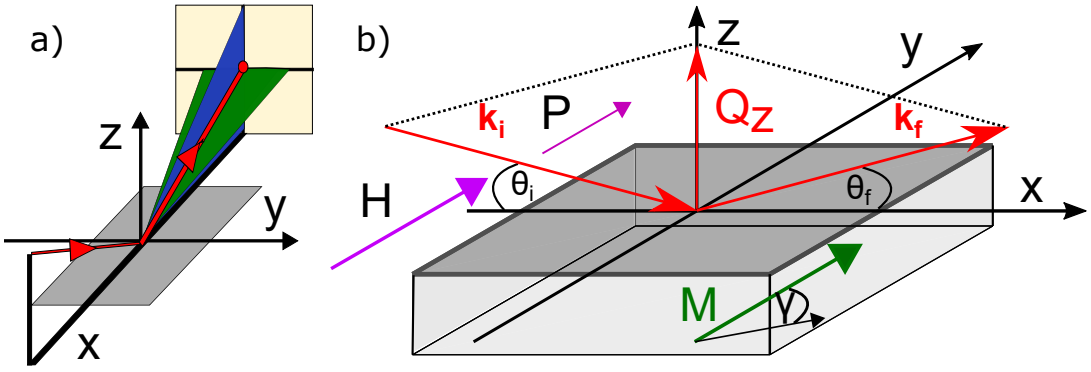

Figure 2.2: a) Different grazing incidence scattering geometries, where the red line is specular reflectivity, the blue plane is off-specular scattering and the green plane is grazing incidence small angle scattering. Figure a) is taken from [132]. b) Q scattering geometry of polarized neutrons reflecting from a film. Incident and scattered neutrons with wave vectors $\mathbf{k}_i$ and $\mathbf{k}_f$, respectively, and scattering vector $\mathbf{Q}_z$ are shown in red, applied field and polarisation direction are shown in purple, and in-plane magnetisation vector **M**, which can have some in-plane angle γ, is shown in green.

There are three grazing scattering geometries shown in figure 2.2 a): specular reflection (SR); scattering in the incident plane or off-specular; and scattering in the XY plane, known as grazing incidence small angle neutron scattering (GISANS). These different scattering geometries probe different length scales and incidence planes. Only specular and off-specular scattering will be discussed in this thesis as the instruments we used were optimised for these scattering geometries. Off-specular scattering (blue plane) is caused by in-plane surface features and has a typical length scale of 600 nm to 60 μm. SR (red line) probes in-depth into the sample, on a length scale of approximately 1 nm to 500 nm.

Figure 2.2 b) shows a collimated neutron beam impinging at a glancing angle θ_i onto a flat and extended surface separating vacuum and film. The reflected beam leaves the surface under a glancing angle θ_f. For SR the incident and final angles are identical, $\theta_i = \theta_f$, meaning only the scattering angle, θ, will be discussed. Assuming elastic scattering such that $|\mathbf{k}_i| = |\mathbf{k}_f| = 2\pi/\lambda$, where λ is the neutron wavelength, the scattering vector $\mathbf{Q}_z$ is given by,

$$\mathbf{Q}_z = \mathbf{k}_f - \mathbf{k}_i = \frac{4\pi}{\lambda}\sin(\theta), \tag{2.2}$$

which points along the z-direction parallel to the surface normal. $\mathbf{Q}_z$ represents the momentum transfer vector for the neutron in the z-direction parallel to the surface normal.

2.2.2 Theory of non-magnetic specular reflectivity

This section is following reference [132]. In a vacuum the part of the neutron energy corresponding to its propagation in the z-direction is,

$$E_z = \frac{\hbar^2 Q_z^2}{8m_n}, \tag{2.3}$$

where m_n is the neutron mass. Due to the "optical approximation" [138] we can model the film as a continuous Fermi pseudo potential,

$$V_n = \frac{2\pi\hbar^2}{m_n}\rho_N, \tag{2.4}$$

where $\rho_N = \sum N_i b_{li}$ is called the nuclear "scattering length density" (SLD) and is the sum of the atomic density of the nuclei in the material N_i multiplied by their individual nuclear scattering lengths b_{li}.

To examine the neutron scattering behaviour from a nuclear potential, we consider the time-independent Schrödinger equation,

$$\frac{-\hbar^2}{2m}\nabla\mathbf{\Psi} + V_n\mathbf{\Psi} = E\mathbf{\Psi}, \tag{2.5}$$

where $\mathbf{\Psi}$ is the neutron wave-function. This equation can be expressed as a Helmholtz propagation equation,

$$\nabla U + \mathbf{k}^2 U = 0, \tag{2.6}$$

where the propagation wave vector in the potential V_n is given by

$$\mathbf{k}^2 = \frac{2m_n}{\hbar^2}(E - V_n). \tag{2.7}$$

Since the neutron follows a classical propagation equation, it is possible to define an optical index n in the medium,

$$n^2 = \frac{\mathbf{k}^2}{\mathbf{k}_0^2}, \tag{2.8}$$

where $\mathbf{k}_0$ is the wave-vector in a vacuum. This optical index is given by,

$$n^2 = 1 - \frac{V_n}{E} = 1 - \frac{\lambda^2}{\pi}\rho_N. \tag{2.9}$$

The square root of equation 2.9 with the binomial expansion yields [139],

$$n \approx 1 - \frac{\lambda^2}{2\pi}\rho_N. \tag{2.10}$$

The value of n is typically less than one. Complete reflection occurs from materials with

$n < 1$ for glancing angles below a critical value of [139],

$$\theta_c = \sin^{-1}(\sqrt{1-n^2}), \tag{2.11}$$

which in combination with equation 2.9 and 2.2, gives a critical wave vector,

$$Q_c = 4\sqrt{\pi\rho_N}. \tag{2.12}$$

Materials are typically quoted in SLD as the refractive index changes as a function of λ.

Here we consider a neutron beam reflecting from a simple substrate. The neutron wave function can be represented using an incident plane wave,

$$\boldsymbol{\Psi}(\mathbf{r}) = e^{i\mathbf{k}\cdot\mathbf{r}} = e^{i\mathbf{k}\parallel\cdot\mathbf{x}}e^{i\mathbf{k}\perp\cdot\mathbf{z}} = e^{i\mathbf{k}\parallel\cdot\mathbf{x}}\boldsymbol{\psi}(z). \tag{2.13}$$

The scattering in specular conditions is continuous and so the neutron wave function can be expressed as a function of z only. When the neutron wave is incident on a surface at an angle greater than θ_c, a portion of the wave will be reflected, giving an opposite phase, and a portion of the wave will be transmitted into the substrate. This gives wave functions in the vacuum and in the substrate of,

$$\boldsymbol{\psi}_0(z) = 1.e^{i\mathbf{k}_{\perp 0z}} + r.e^{-i\mathbf{k}_{\perp 0z}}, \tag{2.14}$$

$$\boldsymbol{\psi}_s(z) = t.e^{i\mathbf{k}_{\perp sz}} + 0.e^{-i\mathbf{k}_{\perp sz}}, \tag{2.15}$$

where 1, r and t are the amplitudes of the incident, reflected and transmitted beam, respectively. Using the continuity equations of the neutron wave function at the interface where z=0, equations 2.14 and 2.15 can be expressed as Fresnel amplitudes of reflection and transmission,

$$r = \frac{\mathbf{k}_{\perp 0} - \mathbf{k}_{\perp s}}{\mathbf{k}_{\perp 0} + \mathbf{k}_{\perp s}}, t = \frac{2\mathbf{k}_{\perp 0}}{\mathbf{k}_{\perp 0} + \mathbf{k}_{\perp s}}. \tag{2.16}$$

The measured reflectivity signal is then $\mathbf{R} = |rr^*|$. In an experiment, this is equivalent to the ratio of measured flux, I, vs incident flux I_0 onto the sample, $\mathbf{R} = \frac{I}{I_0}$. Below Q_c the neutron beam is totally reflected and above approximately $3Q_c$ the signal decays by $1/Q^4$ [132].

2.2.3 Theory of magnetic specular reflectivity

In this section, we follow references [129, 130]. Neutrons carry a magnetic moment μ_n, whose operator,

$$\hat{\boldsymbol{\mu}}_n = \gamma_n\mu_N\hat{\sigma}, \tag{2.17}$$

is proportional to the Pauli spin operator $\hat{\sigma}$ acting in a two-dimensional spin space and being represented by a set of 2 x 2 matrices: $\hat{\sigma} = \{\hat{\sigma}_x, \hat{\sigma}_y, \hat{\sigma}_z\}$ [129]. Here $\gamma_n = -1.913$ is the gyromagnetic ratio of the neutron and $\mu_N = e\hbar/2m_pc$ is the nuclear magneton.

The interaction of a neutron with a sample of magnetic induction vector $\mathbf{B}_l$ is described by a magnetic (Zeeman) potential with the corresponding operation,

$$\hat{V}_m(\mathbf{r}) = -\hat{\boldsymbol{\mu}}_n \cdot \sum_l \mathbf{B}_l(\mathbf{r} - \mathbf{r}_l), \tag{2.18}$$

where r_l refers to the interaction of a neutron with nuclei located at positions r_l, enumerated in the sample by l.

If $\mathbf{B}_l$ is associated with only the unpaired spins of electronic shells from atoms, then it can be expressed via a Fourier transform as [130],

$$\mathbf{B}_l(\mathbf{q}) = 4\pi\mu_l \mathbf{m}_l^{\perp} f_l(Q), \tag{2.19}$$

where $f_l()$ is the magnetic form factor, which in the small angle range of specular reflectivity is assumed to be equal to 1 [140], $\mu_l = |\mu_l|$ is the absolute value of the atomic magnetic moment, μ_l, directed along the unit vector $\mathbf{m}_l = \boldsymbol{\mu}_l/\mu_l$. According to classical electrodynamics [141],

$$\mathbf{m}_l^{\perp} = \mathbf{m}_l - \mathbf{q}(\mathbf{q} \cdot \mathbf{m}_l)/q^2, \tag{2.20}$$

meaning it is orthogonal to the scattering vector q. This result is important for thin films as the scattering vector in specular reflectivity will always be normal to the sample surface, meaning only the in-plane magnetisation component will be observed. As such, any moment rotation that takes place out of the sample plane will be seen as a reduction in the projection of the magnetisation along the applied field direction.

The magnetic field is concentrated within the range of the atomic electron spin density function, which is extended over the atomic size of the order of 10^{-10} m but decays with r^{-3} and can be described as a magnetic scattering length,

$$b_l^m = \frac{m_n}{2\pi\hbar^2}\mu_n \bar{B}_l v_l, \tag{2.21}$$

where $\bar{B}_l = 4\pi\mu_l$ and v_l is the volume per lth magnetic atom [130]. In crystalline systems, v_l is one formula unit.

For a homogeneously magnetized film along the applied field direction y, the potential energies of the neutron-sample interaction for alternative polarization directions are the eigenvalues of the interaction operator from equation 2.18 and are determined by the equation,

$$V_{\pm} = V_n \pm V_m = \frac{2\pi\hbar^2}{m} N(b_l^n \pm b_l^m), \tag{2.22}$$

where +(-) stands for neutrons polarized parallel (anti-parallel) to the applied field direction. Again the neutron wave function is treated a plane wave $\Psi(\mathbf{k},\mathbf{r}) = e^{i\mathbf{k}\cdot\mathbf{r}}$ but now with two dimensional spin states $|\Psi(z)\rangle$ represented by a column [129],

$$|\Psi(z)\rangle = \begin{pmatrix} \Psi_+(z) \\ \Psi_-(z) \end{pmatrix}, \tag{2.23}$$

which denote probability amplitudes to find a neutron with positive/negative spin projections on the y-axis.

If the internal field vector $\mathbf{M}$ makes some in-plane angle γ with respect to the applied filed, then our $V_\pm$ interaction matrix,

$$\begin{pmatrix} V_{++} & V_{+-} \\ V_{-+} & V_{--} \end{pmatrix} = \frac{2\pi\hbar^2}{m} N \left[\begin{pmatrix} b_l^n & 0 \\ 0 & b_l^n \end{pmatrix} + \begin{pmatrix} b_{ly}^m & b_{lx}^m \\ b_{lx}^m & -b_{ly}^m \end{pmatrix} \right], \tag{2.24}$$

has none zero diagonal elements, where b_{ly}^m and b_{ly}^m are the x and y projections of $\mathbf{M}$, such that $\mathbf{M}_x \propto b_l^m sin(\gamma)$ and $\mathbf{M}_y \propto b_l^m cos(\gamma)$. Spin-flip (SF) scattering is the change in a neutron's polarisation from + to - or vice versa, due to the torque applied to its magnetisation from the perpendicular magnetic inductance in the sample, $\mathbf{M}_x$. The diagonal elements $V_{\pm\mp} \propto (b_n \pm b_{ly}^m)$ depend on the parallel inductance, $\mathbf{M}_y$.

Using equations 2.24 and 2.23 the Schrödinger equation can be written as a system of two coupled equations [129],

$$\left[\frac{\delta^2}{\delta z^2} + p_o^2 - \frac{2m}{\hbar^2} V_{++}(z) \right] \Psi_+(z) - \frac{2m}{\hbar^2} V_{+-}(z) \Psi_-(z) = 0, \tag{2.25}$$

$$\left[\frac{\delta^2}{\delta z^2} + p_o^2 - \frac{2m}{\hbar^2} V_{--}(z) \right] \Psi_-(z) - \frac{2m}{\hbar^2} V_{-+}(z) \Psi_+(z) = 0, \tag{2.26}$$

where $p_o = Q_z/2 = \frac{2\pi}{\lambda} \sin\theta$, is the component of the neutron wave vector normal to the field boundary.

Already it can be seen that if V_{+-} and V_{-+} are zero, then equations 2.25 and 2.26 are decoupled and only non-spin-flip (NSF) scattering occurs. In this case, the magnetisation vector $\mathbf{M}$ is aligned only along the y-axis. Solutions for equation 2.25 and 2.26 can be found elsewhere [129, 142–144]. They lead to the following reflectivity signals,

$$\mathbf{R}^{++} = \frac{1}{4} |R_+(1 + cos\gamma) + R_-(1 - cos\gamma)|^2, \tag{2.27}$$

$$\mathbf{R}^{--} = \frac{1}{4} |R_+(1 - cos\gamma) + R_-(1 + cos\gamma)|^2, \tag{2.28}$$

$$\mathbf{R}^{+-} = \mathbf{R}^{-+} = \frac{1}{4} |R_+ - R_-|^2 sin^2\gamma, \tag{2.29}$$

If no spin analysis of the initially polarised reflected neutrons is performed then only the two reflectivities $\mathbf{R}^{+} = \mathbf{R}^{++} + \mathbf{R}^{+-}$ and $\mathbf{R}^{-} = \mathbf{R}^{--} + \mathbf{R}^{-+}$ can be measured, giving,

$$\mathbf{R}^{\pm} = \frac{1}{2}(|r_{+}|^2(1 \pm cos\gamma) + |r_{-}|^2(1 \mp cos\gamma)). \tag{2.30}$$

2.2.4 Specular reflectivity on non-magnetic thin films

With thin film samples, it is necessary to characterise the film in terms of SLD, interface quality and thickness. SLD is particularly important, as it is the sum of the atomic density of the nuclei, which we take as the number of atoms in the unit cell divided by its volume, multiplied by the individual nuclear scattering lengths, given by the chemical composition of the bilayer, as discussed in section 2.2.2. For example, CFO has a unit cell volume of 578 Å^3 [14], with 8 atoms in its unit cell, giving an atomic density of 0.0138 atom/Å^3. CFO has one Co atom of $b_l^n = 2.49$ fm, two Fe atoms of $b_l^n = 9.54$ fm and four O atoms of $b_l^n = 5.803$ fm [145], which summed gives a total $b_l^n = 44.602fm$. The product of atomic density with the scattering length for CFO then gives an SLD of 6.17 10^{-6}/Å^2. The unit of 10^{-6}/Å^2 comes from the calculation of fm/Å^3. Therefore any changes in SLD when compared to the bulk value can indicate either a change in the chemical composition or a change in the density, but crucially, the nature of this change cannot be determined as the two factors are covariant.

If a thin film is grown on a flat substrate, within the length scale of specular reflectivity, Kiessig fringes will be observed in the reflectivity profile. These fringes occur due to scattering from the top and bottom surfaces of the film and are spaced according to,

$$d = 2\pi/\Delta Q_z. \tag{2.31}$$

When a multilayer is deposited, the periodicity generates Bragg reflections of mth order at defined positions in reciprocal space [130]. To simulate the reflective profile of multilayers, numerical modelling is required [132].

When growing real samples it is expected that the interfaces between layers will not be perfectly flat. The average SLD fluctuations in the z-direction at an interface are characterised by the root mean squared (RMS) value,

$$\sigma = \sqrt{\langle z^2 \rangle}, \tag{2.32}$$

commonly referred to as RMS roughness or the Nevot-Croce formalism [146]. For thin film systems, variations in SLD can come from several sources such as structural roughness and chemical diffusion. These effects will both alter the observed SLD and therefore RMS roughness, meaning reflectivity is not sensitive to the nature of σ. This means σ is approximated as a smooth profile.

To demonstrate the effects of roughness and Kiessig fringes, reflectivity on a bare substrate and single films havehad been simulated using the GenX software [147] in figure 2.3. By modelling reflectivity, the layer thickness, interface roughness and layer SLDs can be extracted.

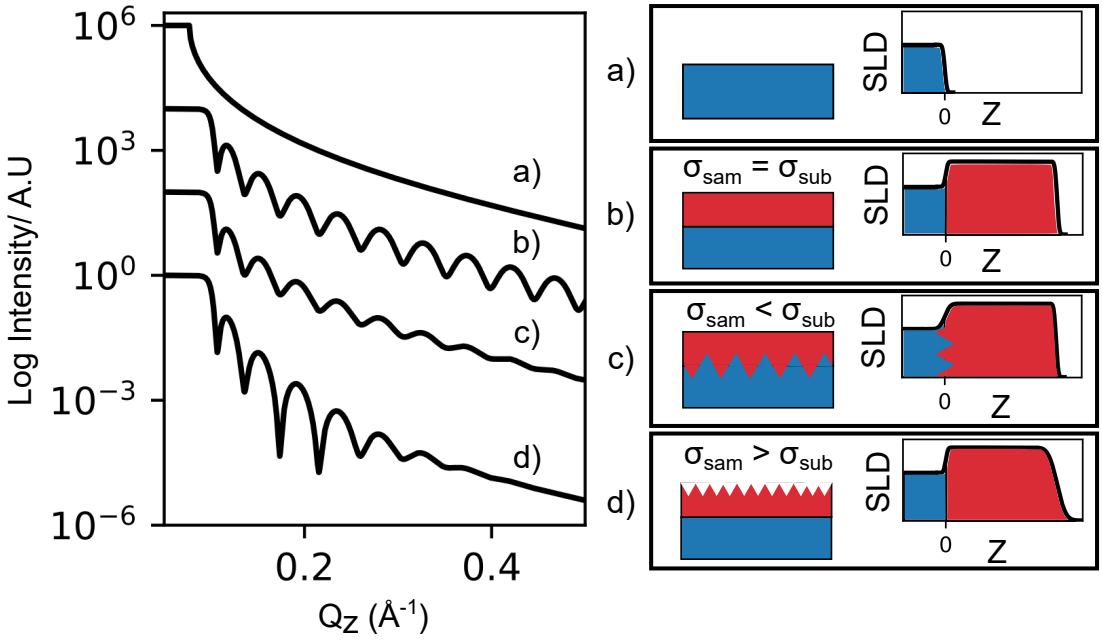

Figure 2.3: Simulated reflectivity profiles of a sample system consisting of a) a bare substrate, b) a substrate and thin film, where the substrate RMS roughness, σ_{sub}, is equal to the sample RMS roughness, σ_{sam}, c) where σ_{sub} is greater than σ_{sam} and d) where the σ_{sub} is less than σ_{sam}.

2.2.5 Specular reflectivity on magnetic thin films

For studying magnetic thin films and multi-layers, PNR allows us to measure the magnetisation as a profile of depth, which we have used to extract information on samples' magnetisation and switching behaviour.

We measure samples with PNR at a saturating field to observe a layer's saturation magnetisation, and for the case of studying magnetisation reversal, for comparison to saturation so that the relative amount of switching can be understood. For a magnetically saturated thin film, where $\mathbf{M}$ is aligned to the applied field direction, PNR will show reflectivity for $\mathbf{R}^{++}$ and $\mathbf{R}^{--}$. In this case, only NSF reflectivity is expected and so the reflectivities can be simplified to $\mathbf{R}^{+}$ and $\mathbf{R}^{-}$. It can be seen in figure 2.4 that the two channels have different Q_c values, Q_{c+} and Q_{c-}, which have shifted the Kiessig fringes but maintained the periodicity at high Q. This difference in Q_c comes from the different SLD profiles for each channel, where $SLD = N(b_l^n \pm b_l^m)$ and $+$ and $-$ represent the difference SLD for the up and down polarised neutrons. The in-plane magnetization profile projected along the external field direction of the films is encoded

in the dependence of the spin-asymmetry ratio $(\mathbf{R}^+ - \mathbf{R}^-)/(\mathbf{R}^+ + \mathbf{R}^+)$ on Q_z. Fitting it against a model gives the depth profile of the magnetic SLD (M-SLD) contribution to the nuclear SLD. When compared to VSM, which averages over the whole sample volume, PNR offers a much higher degree of sensitivity to where the magnetisation is located in depth into the sample.

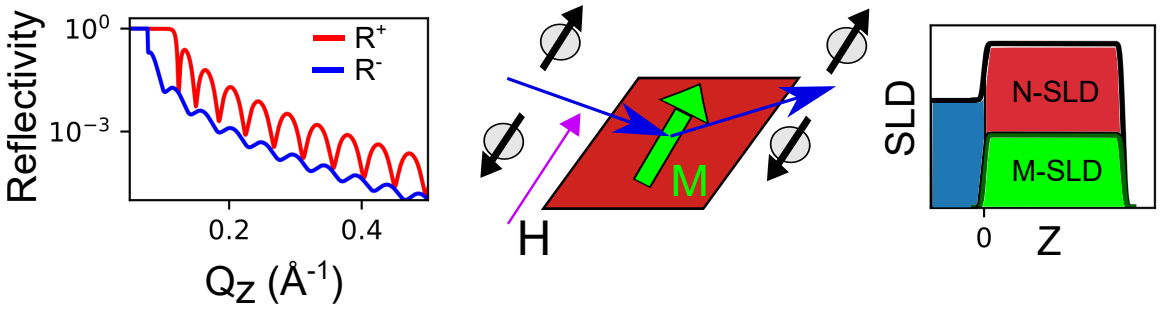

Figure 2.4: Simulated reflectivity profiles R^+ and R^- for a thin film sample with $\mathbf{M}$ aligned with the polarisation axis. In the sample diagram blue arrows represent the neutron propagation direction, black arrows represent the incoming and outgoing neutron polarization and the green arrow is the magnetisation vector $\mathbf{M}$. SLD vs depth into the sample, z, shows both the contributions from the film's nuclear SLD (N-SLD) and magnetic SLD (M-SLD).

When characterising magnetic bilayers, information such as layer coercivity and potential exchange spring interactions can be extracted from the magnetic hysteresis, as such we measured PNR during magnetisation reversal.

Magnetisation reversal has a hysteresis, during which the magnetisation can break down into domains. A magnetic domain is a region in which the magnetic spins of atoms or molecules are aligned. During rotation, a sample can remain as a single domain or become several smaller magnetic domains, each of uniform magnetisation separated by narrow zones called domain walls, in which the spins change orientation from one domain to the next. Depending on the mechanism of rotation and domain propagation, the magnetisation in the domains can make some angle γ with respect to the applied field direction, meaning it is important to consider the magnetisation inside the domains.

The simplest case is shown in figure 2.5, where the sample remains as a single domain during magnetisation reversal. The reflectivity signals R^{++}, R^{--} and R^{+-} are present, where $R^{+-} = R^{-+}$ according to equation 2.29. It can be seen that at $\gamma = 30°$, R^{++} and R^{--} channels are still present, but when $\gamma = 90°$, $R^{++} = R^{--}$ and SF reflectivities increase, as described by equations 2.27, 2.28 and 2.29. This shows that when measuring a single domain state during magnetisation rotation, by using full spin analysis it is possible to determine the modulus of the angle γ,

$$|\gamma| = \arcsin\left(\frac{2\sqrt{R^{+-}}}{|r^+ - r^-|}\right), \tag{2.33}$$

and therefore the magnitude of $\mathbf{M}_x$. The sign of γ cannot be determined as the SF

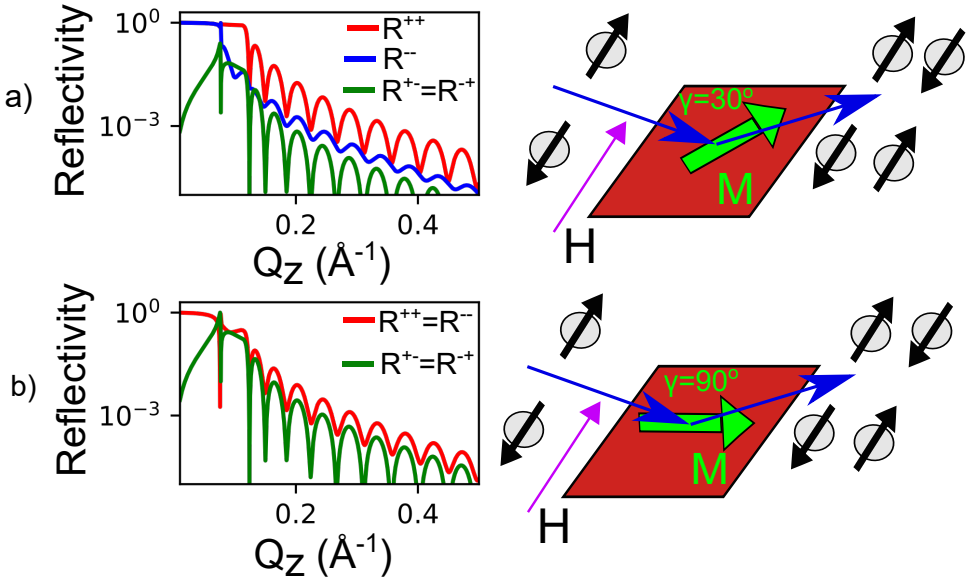

Figure 2.5: Simulated reflectivity profiles R^{++}, R^{--}, R^{+-} and R^{-+} for a thin film sample where $\mathbf{M}$ makes an angle a) $\gamma = 30°$ and b) $\gamma = 90°$ with the polarisation axis. The neutron polarisation and propagation direction are represented by the back and blue arrows, respectively, with the scattered neutrons showing the possible polarisations due to SF.

reflectivity is proportional to $\sin^2(\gamma)$ from equation 2.29. Without analysis, we would measure the reduced reflectivity $\mathbf{R}^{\pm}$ from section 2.2.3. The SF scattering is still present but in combined channels of SF+NSF. The same magnetisation is seen in the sample, but without analysis, it is difficult to separate out the different contributions. The effect of the SF scattering will reduce the spin-asymmetry, which can lead to an apparent reduction in measured magnetisation projection.

If the sample's magnetisation breaks down into domains during its rotation, the scattering becomes more complicated. If during reversal the domains are larger than the neutron longitudinal coherence length l_y^{coh}, each domain will contribute to the respective reflectivity, leading to signals for R^{++}, R^{--} and $R^{+-} = R^{-+}$. In this case the reflectivity $\mathbf{R}$ is equal to the weighted sum of $\mathbf{R}_i$ from ith domain,

$$\mathbf{R} = \sum_i w_i \mathbf{R}(\gamma_i), \tag{2.34}$$

where $w_i = w(\gamma_i)$ is the surface fraction of domains with magnetisation axis tilted at the angle γ_i [130]. It's important to note that this is an incoherent sum, and so no information on the structure of the domains is recorded. Large domains with no analysis will therefore present SF+NSF, meaning a potential reduction in spin asymmetry which can lower the observed magnetisation projection.

If the domain size is sufficiently small such that it can be illuminated by the neutron coherently, both specular and off-specular scattering needs to be considered.

Scattering from objects that lie in the X direction within l_y^{coh} add up coherently i.e the

scattered intensity of all domains in the ith l_y^{coh} is a square of the sum of the amplitudes,

$$\left(\frac{d\sigma}{d\Omega}\right)_i^{coh} = \left(\sum_j f_j\right)^2, \tag{2.35}$$

where $\frac{d\sigma}{d\Omega}$ is the differential cross-section discussed in section 2.3.1 and f_j is the scattering amplitude for the jth domain [130]. Scattering from objects which are separated by a distance larger than the coherence volume add up incoherently i.e. the total intensity is the sum of all scattering cross-sections indexed by the subscript i,

$$\frac{d\sigma}{d\Omega} = \sum_i \left(\frac{d\sigma}{d\Omega}\right)_i^{coh}, \tag{2.36}$$

similar to equation 2.34 [130].

SR follows equation 2.36, meaning the reflection from each l_y^{coh} is always incoherently summed, where the observed γ is the average, $\langle\gamma\rangle$, for all domains within l_y^{coh}. If during magnetisation reversal there is no preferential direction for the rotation, i.e. rotation is symmetric about the x-axis, then $\langle\gamma\rangle$ over the l_y^{coh} is zero, meaning no specular SF is observed, even though some domains are at an angle with the polarisation axis. As the domains are summed over the coherence length, this can result in a reduced average projection of the magnetisation when compared to the magnetisation in each domain. This means small domains can lead to a reduction in spin-asymmetry and therefore observed magnetisation projection. As such without analysis, small and large domains can have a similar effect on the spin asymmetry, resulting in a reduced observed magnetisation projection.

Off-specular scattering follows equation 2.35, meaning if more than one domain is within l_y^{coh}, the γ and size of each domain l_y^{coh} needs to be considered. Multiple domains with a clear structure within l_y^{coh}, which are not much smaller than l_y^{coh}, lead to potential steps which can cause off-specular scattering peaks in both SF and NSF channels. If the domain length is much smaller than l_y^{coh}, then the coherent sum begins to dephase, which increases the broadening of the off-specular peaks and leads to reduced intensity [130].

As such, if a magnetic thin film breaks down into multiple domains during magnetic reversal, the effects of large domains and small domains can be similar for the SR due to the combination of NSF and SF channels and the averaging over the coherence length. For off-specular, the size of the domains relative to l_y^{coh}, typically between 600 nm to 60 μm [132], and the angle γ in each domain are crucial as they can affect both SF and NSF channels.

2.2.6 Modeling of reflectivity data

In order to acquire quantitative data from neutron reflectometry curves it is necessary to model the sample and then simulate the data using reflectometry modelling software. A number of fitting software are publicly available and we currently use GenX [147].

Figure of merit

The figure of merit (FOM) is a function which is used to compare how well a simulation matches a dataset. The most commonly used FOM is chi-squared (χ^2), however for neutron reflectivity where the data scales with a function of $\sin^{-4}(2\theta)$, this can mean data points closer to the critical edge are weighted far more heavily than points at higher Q_z values. One solution is to use a normalised FOM. In GenX there are multiple normalised FOMs and we typically use sintth4, where the data and simulation are multiplied by a factor of $\sin^4(2\theta)$, given by,

$$FOM_{sintth4} = \frac{\sum_i |Y_i - S_i| \times \sin^4(2\theta)}{N - p} \tag{2.37}$$

where the data set is Y, the simulation is S, a single element is denoted by i, N is the number of points and p is the number of free parameters. In the case where there are many large errors, FOMs can be weighed such that data points with larger errors are worth less than those with smaller ones. In these cases, we have used a logarithmic normalised FOM named logbars, given by,

$$FOM_{logbars} = \frac{1}{N - p} \times \sum_i \frac{|\log_{10}(Y_i) - \log_{10}(S_i)|}{E_i \cdot \ln(10) \cdot Y_i}, \tag{2.38}$$

where E is the error array [147]. With PNR, high Q values have typically larger error bars as they have low count rates, meaning fitting with a weighted FOM can ignore these regions. Typically we used the weighted logbars FOM to get an initial fit but have then switched to the unweighted sintth4 FOM for a better overall compared to the data. From the FOM, after a fit is finished errors bars are calculated by varying the fit parameters until they change 5 % of the FOM [147].

Making a model

As discussed in sections 2.2.4 and 2.2.5, PNR is sensitive to layer thickness, interface RMS roughness, nuclear SLD (N-SLD), magnetic SLD (M-SLD) and in the case of SF, γ. In order to extract this information from measured reflectivity profiles, a model is used to simulate the reflectivity. Models consist of an infinitely long substrate with a slab or multiple slabs which represent layers. The N-SLD of the substrate and slabs are calculated from known tables of scattering lengths for neutrons (and X-rays in the case

of X-ray reflectivity) and crystal volumes, discussed in section 2.2.4. For the magnetic layers, the M-SLD is initially estimated using known bulk magnetisation. Layer thickness and interface RMS roughness are estimated from the sample growth and that thin films typically have smooth interfaces of RMS roughness lower than 100 Å. From this model, we simulate the reflectivity and compare it to our measured reflectivity. Based on the FOM, the model is then refined. Typically the procedure is to first fit the layer thickness, and RMS roughness, however, if a good fit is not achieved then we then expand the parameters to the N and M-SLD of the layers. The N-SLD of the substrate is not fitted as it is assumed to present a bulk value. Additional layers can be added to the model to improve the fit, but introduce a large number of extra parameters and so are only used if necessary. Fitting is stopped once the simulated reflectivity matches best as possible to the measured reflectivity and a suitable FOM is achieved with a model that is still physical i.e. physically possible/reasonable—. From the refined model, we extract values and error bars for layer thickness, RMS roughness, N-SLD, M-SLD and in the case of SF (where there is a considerable contribution), the in-plane magnetisation angle with respect to the applied field direction, γ.

Complementary techniques for making a PNR model

When attempting to fit PNR data there are a number of complementary techniques available. X-ray reflectometry can be used to determine layer thickness, roughnesses and X-ray SLD, with the advantage of different chemical contrast to neutrons, discussed in section 2.2. XRR can be fitted in parallel with PNR. This is because they see the same layer thicknesses and roughnesses, and the X and N-SLD need to agree on the material, meaning parallel fitting increases the reliability of the model.

VSM can be used to estimate the magnetisation of each layer but this is not as straightforward to implement as XRR. VSM measures the sample moment, whereas PNR measures the in-plane magnetisation projection. Therefore the effects such as out-of-sample plane rotation can lead to differences in an observed moment. The calculation of magnetisation from the moment measured with VSM carries considerable errors, discussed in section 2.4.2, which can lead to disagreement with the observed magnetisation projection with PNR.

We sometimes compare the magnetisation from VSM measurements to PNR by converting μ_B/F.U. to M-SLD. These calculations have been performed using the equation for the magnetic scattering length, $b_l^m = \frac{m_n}{2\pi\hbar^2}\mu_n \overline{B}_l V_l$ from section 2.2.3, where μ_n is the neutron magnetic moment, B_l is the magnetic field present in the volume, V_l, which is the atomic density of the material and $\frac{m_n}{2\pi\hbar^2}\mu_n = 2.645 \times 10^5$. For example, CFO with an atomic density of 0.0136 atoms/Å^3 and a magnetisation of 3.7 μ_B/F.U.gives an M-SLD of 1.351 10^{-6}/Å^2.

2.2.7 Neutron reflectivity experimental setup

The majority of PNR experiments in this thesis have been performed at the D17 instrument [148, 149] (ILL, Grenoble, France), schematically shown in figure 2.6, with a minority of data being collected at the Super-ADAM instrument [150] (ILL, Grenoble, France). As such, unless specifically stated, PNR measurements have been performed on D17. D17 is a time of flight (TOF) instrument, but can also be operated in a monochromatic configuration. TOF measures with a white neutron beam, allowing for continuously variable resolution and a range of Q values to be measured simultaneously. Monochromatic measurements, on the other hand, offer a constant wavelength resolution and polarisation, where the entirety of the flux is focused on a single Q value, which can be useful where specific features of reflectivity need to be resolved. Here we describe the D17 Instrument, a more complete description of the current instrument can be found elsewhere [148, 149].

D17 is supplied by the cold neutron guide H18 at ILL. An entrance slit which transmits a beam height of 160 mm is used to capture the vertical divergence of the 150 mm H18 guide, but in typical operation, the entrance slit is open by 10 mm to limit the flux [148]. A low-efficiency uranium neutron monitor is used to correct reactor power fluctuation. In monochromatic mode, the double disk choppers are stopped in an open position and a Ni/Ti non-polarising monochromator is used. To select the desired 5.5 Å wavelength the focusing guide is rotated 4° to match the corresponding Bragg reflection. In TOF mode, the rotating-disk chopper pair is activated in order to pulse the beam. A pair of collimator slits are used to define the beam size and horizontal divergence. The top and bottom of the focusing guide are coated with a supermirror with the focal point at the sample. The data is collected by a time-resolved two-dimensional detector with a spatial resolution of 2.2 × 5.2 mm^2 (horizontal × vertical full-width half maximum) [148].

In our experiments, we used polarised neutrons. For monochromatic measurements, polarisation is provided by a Si/Fe polarising monochromator in a permanent magnet assembly. In TOF operation, a supermirror S-bender [151] is moved into the beam path to polarize a large section of the wavelength band from 4 to 20 Å, with a typical polarisation of $p_0 > 99\,\%$. Two adiabatic radio frequency (RF) spin-flipper coils are positioned before the focusing guide and in the detector chamber. If only the $\mathbf{R}^+$ and $\mathbf{R}^-$ reflectivities are required, only the first spin-flipper at the exit of the focusing guide is used to flip the neutron polarization. For measurements where $\mathbf{R}^{++}$, $\mathbf{R}^{--}$, $\mathbf{R}^{+-}$ and $\mathbf{R}^{-+}$ are recorded, both spin-flippers are used in conjunction with an analyser. Polarisation analysis is performed either by a supermirror for TOF or a ^{3}He cell for monochromatic measurements and off-specular measurements which are expected to cover the full detector [148].

All of our experiments at the D17 instrument [148] (ILL, Grenoble, France) were performed in polarized time-of-flight (TOF) mode. Measurement times are a crucial

factor to consider as PNR experiments are given limited beamtime on each instrument. As such, TOF mode was selected as measuring over a range of Q values resulted in shorter measurement times when compared to the monochromatic mode. The PNR experiments at the Super ADAM instrument [150] (ILL, Grenoble, France) were monochromatic. For all room temperature measurements, magnetic fields were controlled by a 1.48 T vertical field electromagnet. For measurements taken at 5 K on D17, sample temperature and magnetic fields were controlled by an Oxford Instruments 7 T vertical field cryomagnet.

When using D17, neutrons with wavelengths 4-20 Å were used to ensure the constant polarization of $p_0 > 99\%$. Field measurements at 1.48T and RT were taken to a Q range of 0.003 to 0.22 Q_z. When using Super ADAM we used a neutron wavelength of 5.2 Å, with a polarization of $p_0 > 99\%$. The field measurements at 1.48 T were taken with a Q range of 0.001 to 0.10 Q_z. D17 TOF data reduction was performed using the COSMOS software [152]. Super ADAM data reduction was performed using the PySAred package [153]. The data reduction includes corrections for over-illumination (Super ADAM only), direct beam normalization, polarization inefficiency, angle misalignments, monitor calibrations, background subtraction, and curved samples.

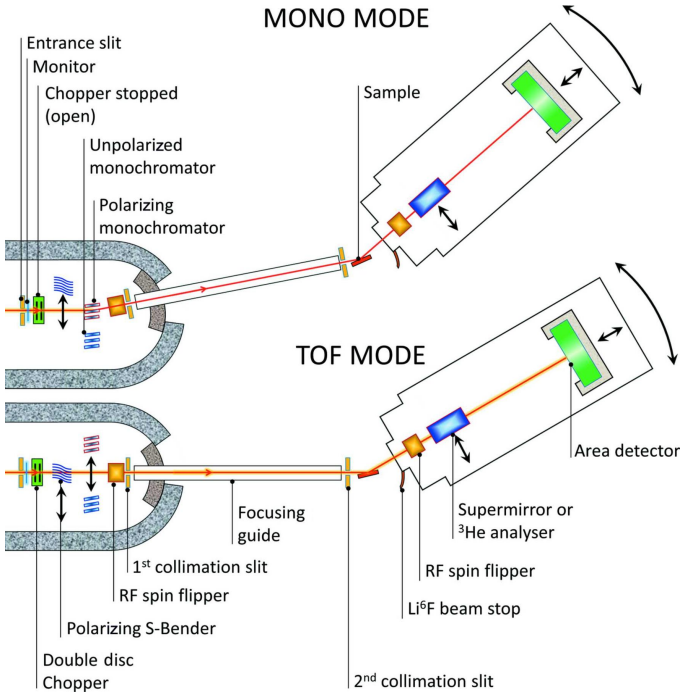

Figure 2.6: Institue Laue Langevin (ILL) instrument D17 [148].

2.3 X-ray diffraction

X-ray diffraction (XRD) is a powerful characterisation technique for thin films and heterostructures. Its ability to probe inter-atomic distances means a sample's crystal struc-

ture can be observed. The super-exchange interactions in ferrites mean that crystal structure and magnetic properties are strongly interlinked, and so characterisation with XRD is necessary to understand the magnetisation of these thin films and heterostructures. Many excellent resources exist which describe diffraction [134, 140, 154–158]. Here we highlight some key results and how they are used to extract structural information from thin film heterostructures.

2.3.1 Scattering and differential cross-sections

If some flux, Φ, is incident on a medium, then the cross-section, σ, of that medium is the ratio of scattered particles vs the incident flux,

$$\sigma_{tot} = \frac{(total\ number\ of\ particles\ scattered\ per\ second)}{\Phi}, \tag{2.39}$$

where Φ has the units area^{-1} time^{-1}, giving σ units of area, hence cross-section [140]. It is necessary to count the number of X-rays (or neutrons) which have been scattered from some medium and arrived at a detector placed at some spherical angle. It is assumed that the distance to the detector is large compared to the dimensions of the detector and the medium, such that the small solid angle $d\Omega$ subtended by the detector and the medium are well defined. Using polar coordinates to describe the scattering, shown in figure 2.7, where the direction of the scattered neutrons is θ and ϕ, the differential cross section is defined by,

$$\frac{d\sigma}{d\Omega} = \frac{(total\ number\ of\ particles\ scattered\ per\ second\ into\ d\Omega\ in\ the\ direction\ \theta\phi)}{\Phi\ d\Omega}. \tag{2.40}$$

Meaning in a real experiment, the differential cross-section is what will be measured (excluding any neutron spin states) [140].

2.3.2 Bragg diffraction from a rigid crystal

Crystals are periodic arrays of atoms. An example 2D single crystal is shown in figure 2.8. For a three-dimensional crystal, the lattice points are displaced from the origin by lattice vectors,

$$\mathbf{l} = n_1\mathbf{a} + n_2\mathbf{b} + n_3\mathbf{c}, \tag{2.41}$$

where n_1, n_2 and n_3 are integers.

If an incident beam, treated as a planar wave with wave vector $\mathbf{k}_i$, is elastically scattering from a crystal, then the differential cross-section in the far-field limit is proportional to

$$\left(\frac{d\sigma}{d\Omega}\right) \propto \left|\sum_{j=1}^{N} b_{lj} e^{i\mathbf{Q}\cdot\mathbf{R}_j}\right|^2, \tag{2.42}$$

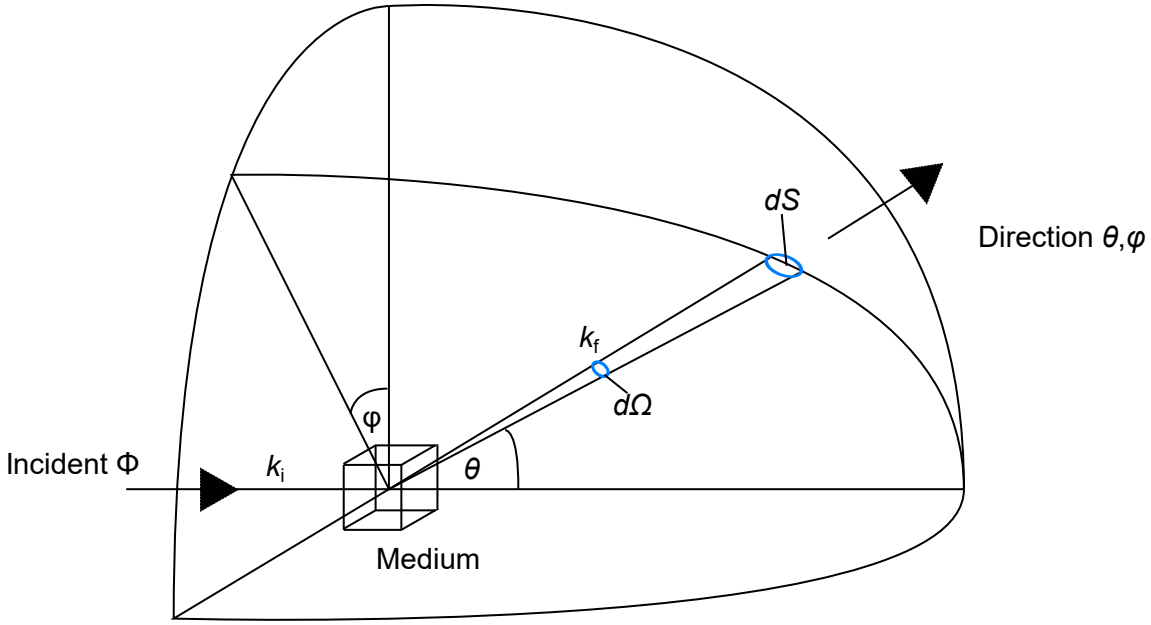

Figure 2.7: Vector diagram for proton or neutron of incident wave vector k_i and final wave vector k_f scattering elastically through an angle of θ, into a small detector area of dS.

where b_{lj} is the scattering length of the jth atom located at $\mathbf{R}_J$ and $\mathbf{Q} = \mathbf{k}_i - \mathbf{k}_f$ is the scattering vector [140]. If a nucleus has a position $\mathbf{R}_{jn}$ away from an atom at a lattice vector $\mathbf{l}$ by lattice a spacing $\mathbf{d}_n$ where,

$$\mathbf{R}_{jn} = \mathbf{l} + \mathbf{d_n}, \tag{2.43}$$

such that,

$$\left(\frac{d\sigma}{d\Omega}\right) = \left|\sum_l e^{i\mathbf{Q}\cdot\mathbf{l}} \sum_l b_d e^{i\mathbf{Q}\cdot\mathbf{d_n}}\right|^2, \tag{2.44}$$

then coherent (Bragg) scattering will occur when all terms in this sum equal 1. This means $\mathbf{Q}$ must be,

$$\mathbf{Q} = h\mathbf{a^*} + k\mathbf{b^*} + l\mathbf{c^*}, \tag{2.45}$$

where h, k and l are integers and,

$$\mathbf{a^*} = \frac{2\pi\mathbf{b}\times\mathbf{c}}{\mathbf{a}\cdot(\mathbf{b}\times\mathbf{c})}, \mathbf{b^*} = \frac{2\pi\mathbf{c}\times\mathbf{a}}{\mathbf{a}\cdot(\mathbf{b}\times\mathbf{c})}, \mathbf{c^*} = \frac{2\pi\mathbf{a}\times\mathbf{b}}{\mathbf{a}\cdot(\mathbf{b}\times\mathbf{c})}, \tag{2.46}$$

are the reciprocal lattice vectors [140], such that for example $\mathbf{a}\cdot\mathbf{a^*} = 2\pi$ and $\mathbf{a}\cdot\mathbf{b^*} = 0$. This means that strong elastic scattering occurs when Q is equal to a lattice spacing in reciprocal space,

$$\mathbf{Q} = \mathbf{G}_{hkl} \tag{2.47}$$

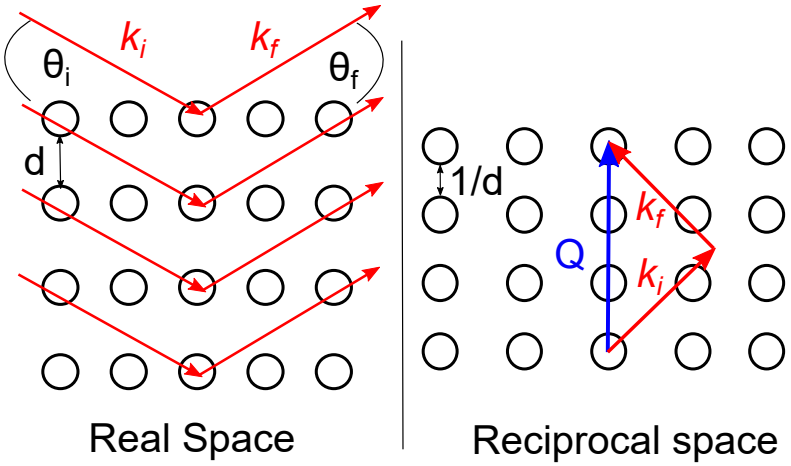

Figure 2.8: Diagram of a 2-dimensional crystal of in-plane lattice spacing d in real and reciprocal space, showing scattering of an X-ray with initial and final wavevectors $\mathbf{k}_i$ and $\mathbf{k}_f$, and incident and scattered angles θ_i and θ_f, leading to a momentum transfer vector $\mathbf{Q}$.

known as the **Laue condition** where,

$$\mathbf{G}_{hkl} = h\mathbf{a}^* + k\mathbf{b}^* + l\mathbf{c}^*. \tag{2.48}$$

This is shown in figure 2.8, where in reciprocal space the $\mathbf{Q}$ vector is matching the spacing of the crystal, fulfilling the Laue condition. Using the set of all reciprocal vectors $\mathbf{G}_{hkl}$, with the properties that $\mathbf{G}_{hkl}$ is normal to the plane (hkl) and that $|\mathbf{G}_{hkl}| = \frac{2\pi}{d_{hkl}}$, the Laue condition can be written as,

$$\frac{4\pi}{\lambda}\sin(\theta) = \frac{2\pi}{d_{hkl}}, \tag{2.49}$$

where the definition of $\mathbf{Q}$ has been taken from section 2.2.1. Equation 2.49 rearranged gives,

$$\lambda = 2d_{hkl}\sin(\theta), \tag{2.50}$$

known as Braggs law. This equation is typically presented as,

$$n\lambda = 2d_{hkl}\sin(\theta), \tag{2.51}$$

where n is an integer which refers to the diffraction order.

2.3.3 X-ray diffractometer

The standard experimental set-up for our X-ray diffraction (XRD) (and X-ray reflectivity) measurements was as follows. The measurements were performed on the Panalytical Empyrean X-ray diffractometer. Measurements were performed at room temperature and no field with a Cu anode source. The components of an X-ray diffractometer are

shown in figure 2.9. For the incident side, a fixed divergence slit 1/16 to 1/32 inches was placed before the focusing optic. We have used two optics, a monochromatic linear beam divergence optic producing a K_α wavelength of 1.5406 Å and a Bragg-Brentano para-focusing optic. For the receiving side, after the sample stage, we use an anti-scatter slit between 1 and 1/16 inches, then a beam collimator with Soller slits of acceptance angles of 0.04 RADs, then an automatic attenuator and before the detector, a receiving slit of between 1/16 to 1/32 inches. The detector was a one-dimensional scintillator detector.

For XRD, due to the lower intensity of the scattering, it was preferred to use wider 1/16 slit widths. All XRD measurements were taken after alignment to a sample Bragg reflection, with $\theta_i = \theta_f$ and $\mathbf{Q}$ normal to the sample surface. For measurements with reflectivity, it was preferred to use the smaller 1/32 fixed divergent and receiving slits to lower the angular divergence, as the error in the measured Q_z in these experiemnts is a combination of the fractional errors from λ and θ, given by [130],

$$\frac{\Delta Q_z}{Q_z} = \sqrt{(\frac{\Delta\lambda}{\lambda})^2 + (\frac{\Delta\theta}{\theta})^2}. \tag{2.52}$$

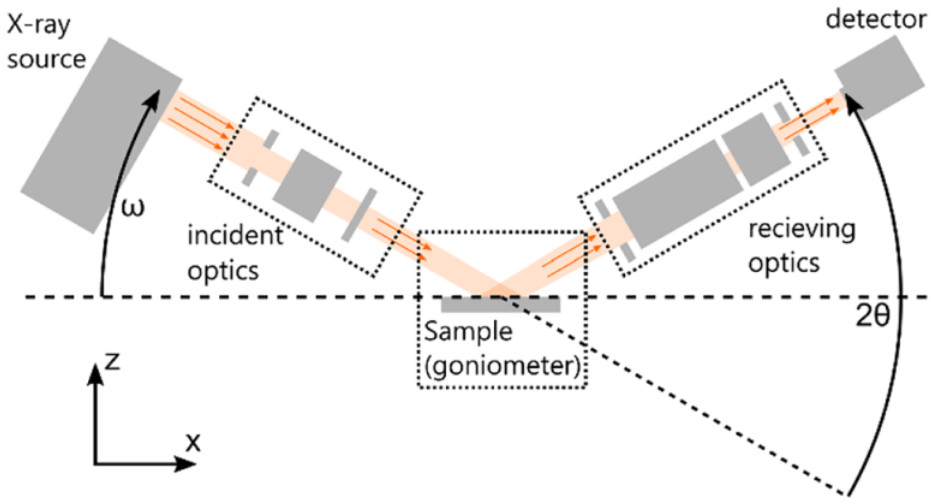

Figure 2.9: Components of a diffractometer [159]

2.3.4 X-ray diffraction on thin films

Diffraction from thin films gives us crucial information about the samples' crystallinity. There are several important structural types that we consider for our samples when performing XRD normal to the sample surfaces. For an amorphous sample, there is no regular array of atoms and so no sample diffraction peaks will be observed. For a polycrystalline sample, multiple crystalline orientations will be present normal to the sample surface, leading to multiple diffraction peaks from each orientation. An in-plane textured sample presents a single crystalline orientation normal to the sample surface

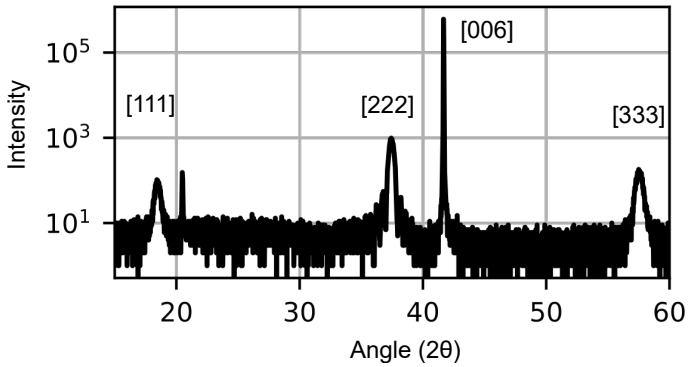

Figure 2.10: XRD measured on a crystalline CFO thin film, where the film CFO [111] and substrate Al_2O_3[006] Bragg peaks can be seen.

but may have different crystallographic orientations in the sample plane. An epitaxial sample is considered a single crystal. When measuring XRD normal to the sample surface, epitaxial and textured samples will both only present one orientation and so they cannot be distinguished. To distinguish an epitaxial structure from a textured structure, a full reciprocal space map is needed [160].

An example of XRD using the setup described in section 2.3.3 with the monochromatic optic has been taken on a thin film sample, shown in figure 2.10. As **Q** is normal to the sample surface, the out-of-plane (OOP) crystallographic orientation has been probed. The Bragg reflections have been fitted using a Gaussian profile in the Python programming language with the scipy.optimize.curve_fit function. From the fitted Gaussians, we extract peak values and error bars. Using equation 2.51 we then calculate the sample, d_{sample}, spacing. The d spacing between lattice planes for cubic systems is given by,

$$d_{hkl} = \frac{a}{\sqrt{h^2 + k^2 + l^2}}. \tag{2.53}$$

where a is the lattice constant. Using equation 2.53 with the known bulk lattice constants for a sample, we calculate the expected d_{bulk} for a given orientation and can then distinguish which orientation is present. Once the orientation is known, if there is a difference between d_{bulk} and sample d_{sample}, the sample is strained, where the percentage strain is given by,

$$\epsilon = \frac{d_{sample} - d_{bulk}}{d_{bulk}} \times 100. \tag{2.54}$$

As such, we measure XRD normal to the sample surface to discern a sample's crystalline structure, orientation, lattice constant and out-of-plane strain.

2.3.5 Laue oscillations

If a film is sufficiently crystalline and planar, weak subsidiary maxima can be observed on the sides of Bragg reflections, known as Laue oscillations. Specifically, Laue oscillations

are diffraction from the longest region of coherent unit cells, d_{coh}. The positions and intensities of these satellite reflections are predicted by the Laue interference function [161–163],

$$I(\mathbf{Q}) \propto \frac{sin(\frac{N}{2}\mathbf{Q}_c)^2}{sin(\frac{1}{2}\mathbf{Q}_c)^2} \tag{2.55}$$

where c is the lattice constant, $\mathbf{Q}$ is the scattering vector and N is the integer number of coherent diffracting unit cells. Figure 2.11 shows an example of a measured [222] peak from a [111] orientated $CoFe_2O_4$ thin film. The Laue oscillations have been simulated using the python programming language with the scipy.optimize.curve_fit function. The lattice parameter is calculated before fitting, discussed in section 2.3.4. From the fit we extract a value and error for the N unit cells, which multiplied by the lattice parameter gives d_{coh}.

As discussed in section 2.2.4, reflectivity observes Kiessig fringes, which come from changes in N and M-SLD profiles from the top and bottoms of layers. Laue oscillations observe the crystalline structure and are sensitive to disorder. This makes the two techniques complementary, as Kiessig fringes will observe the total layer thickness, while Laue oscillations will observe the longest coherent crystalline length.

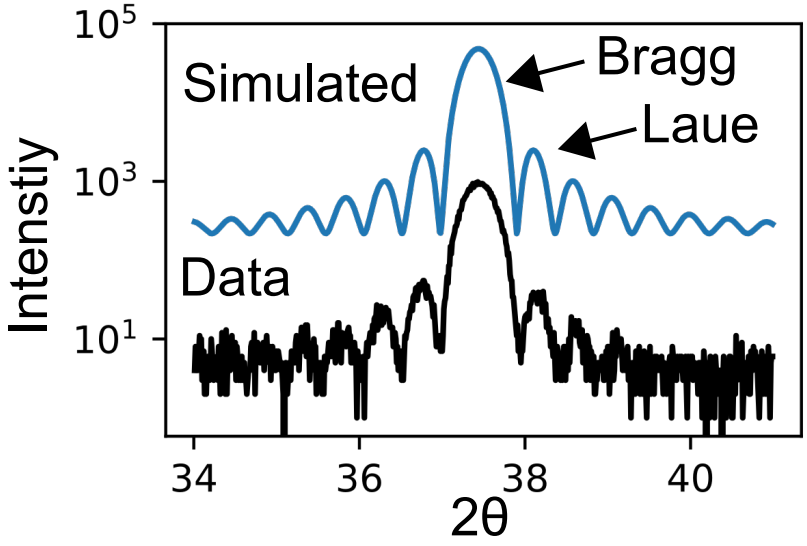

Figure 2.11: Measured and simulated XRD showing both Bragg peaks and Laue oscillations.

2.3.6 Scherrer equation

Paul Scherrer published an equation in 1981 known as the Scherrer equation [164], which describes the average crystallite size in a system from the breadth of its Bragg peaks, given by,

$$L = \frac{K\lambda}{\beta cos\theta}, \tag{2.56}$$

where λ is the X-ray wavelength, β is the integral breadth of the sample Bragg peak in radians, K is a dimensionless shape factor typically taken as 0.9, and θ is the angle of the Bragg peak. Generally, this value can be taken as a lower bound of the crystal size. When applied in thin films, assuming an out-of-plane (OOP) peak is measured, the peak broadening is caused by the average coherent crystalline length OOP, such that $L = d_{coh}$ from section 2.3.5.

A conventional approach is that the integral breadth of the pure sample profile β is separated from the observed profile B by subtracting the instrument profile b. If all profiles are assumed to be Lorentzian then $B = b+\beta$, and for Gaussian this is $B^2 = b^2+\beta^2$ [165]. We found for our samples a Gaussian profile best approximated the Bragg peaks. The sample and instrument peaks were fitted using the python programming language with the scipy.optimize.curve_fit function. The integral breath was taken as the full-width half maximum (FWHM) of the Gaussian. From the fit, we extract values and errors for the FWHM and Bragg angle for sample and instrument peaks. When using a monochromatic optic, λ was taken from the K_α 1.5406 Å. For the case of a non-monochromatic optic, there will be two Gaussians superimposed from the K_α and K_β wavelengths. In this case, we fit a double Gaussian where the FWHM of the Gaussians are coupled parameters. Once all the required parameters are known, d_{coh} for the sample can be calculated from the Scherrer equation.

If the sample is strained then the sample peak will be broadened by $\beta = \beta_m + \beta_n$, where β_m is the integral breadth from the crystallite size and β_n is the integral breadth broadening due to the lattice strain, given by [165],

$$\epsilon = \frac{\beta_n}{4tan\theta} \times 100. \tag{2.57}$$

This is the same ϵ discussed in section 2.3.4. As both the d_{coh} and ϵ broaden the sample peaks, but by differing amounts depending on θ, multiple Bragg reflections need to be measured in order to separate the two. Once multiple values for β have been calculated, the strain can then be calculated via the x-intercept and gradient from a plot of $\beta cos\theta$ vs $4\sin\theta$, an example can be found in reference [166].

Values of crystallite size calculated using the Scherrer equation are generally used as estimates as they carry significant errors. This error comes from multiple origins. The value of the shape factor K can vary depending on the definition of the 'breadth' of the crystal, crystalline shape and crystal direction [167]. Error is introduced by assuming the peaks are either Gaussian or Cauchy [168]. By subtracting b from B the fractional error becomes larger. Due to these errors, the measurement of d_{coh} from the Laue oscillations is considered to be more reliable.

The error associated with using the Scherrer formula makes the calculation of strain difficult with our sample systems. The NFO and CFO [111] direction will produce four

peaks in a 100° 2θ range, giving only four data points. An x-intercept and gradient calculated from just four points, all with considerable errors, would not be reliable and so we do not attempt to calculate strain with this method.

2.4 Vibrating sample magnetometry

Vibrating sample magnetometry (VSM) is a powerful tool for characterising the magnetic properties of thin films and heterostructures. Superconducting quantum interface device (SQUID) VSMs such as the Quantum Design MPMS VSM which we have used, have the ability to measure to high fields of up to 7 T, alongside short averaging times and fast ramping speeds. This means we were able to measure high-resolution hysteresis loops to high fields, with reasonable data acquisition times.

2.4.1 Working principles

The creation of the VSM is accredited to S. Foner [169]. The operation is based on the flux change in a coil when a magnetized sample is vibrated in close proximity. The sample is attached to the end of a non-magnetic rod, made with for example carbon fibre, which is attached to a mechanical vibrator. The oscillating magnetic field of the sample induces an alternating electromagnetic force (EMF) in the pickup coils, according to Faraday's law [170]. As sample sizes are small [12], typically less than 1 g, the EMF needs to be amplified by lock-in amplifiers. An advantage of VSMs is that they can be adapted to high and low-temperature measurements as only the sample and vibrating rod needs to be heated or cooled. A diagram of a typical VSM can be seen in figure 2.12. The main advantage of measuring using this technique is the ability to probe directly the magnetic moment of the sample and therefore the magnetisation M, while effectively ignoring the applied field H.

Measurements have been made using either a Quantum Design MPMS3 SQUID VSM or a custom-built VSM at the University of York, School of Physics, Engineering and Technology. A SQUID is based on the tunnelling of superconducting electrons across a very narrow insulating gap, called a Josephson junction, between two superconductors. When a changing magnetic field is applied, the design of a SQUID is such that it can detect a single flux quantum, giving an extremely high sensitivity to the magnetisation [12], of down to 10^{-8} emu. As such, for measurements which are used to calculate the magnetisation of a sample, we use a SQUID VSM. Measurements can be made in either DC mode or VSM mode. In DC mode, the sample is moved back and forth one time through a 2^{nd} order gradiometer, producing a voltage waveform which is then fitted to calculate the sample magnetisation. This comes with several disadvantages, mainly long measuring times of around 30 seconds per point and would only be considered for use

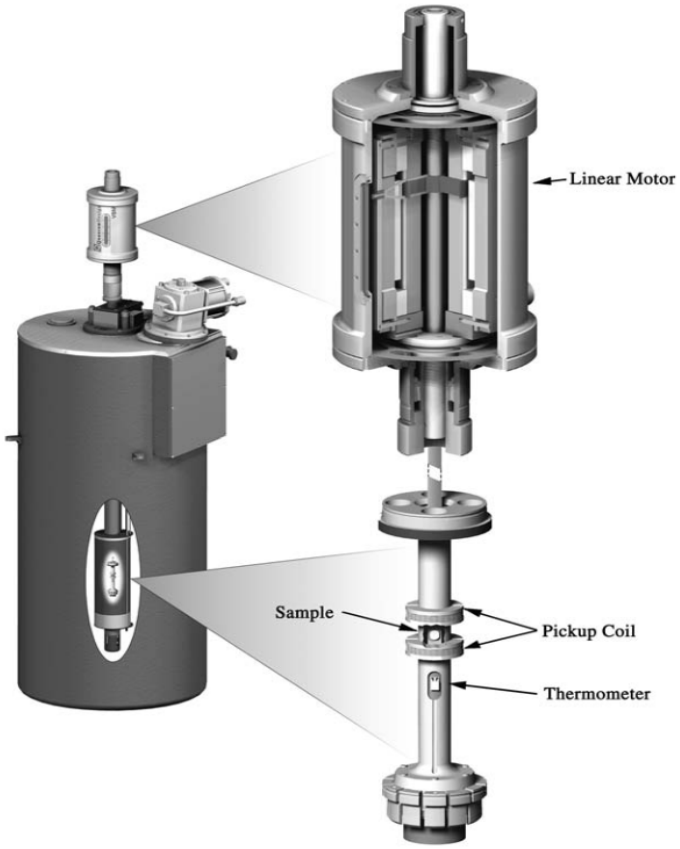

Figure 2.12: VSM working in a superconducting solenoid. The oscillating sample motion is provided by a linear motor [12].

with samples that are too large or unsuitable to be vibrated [171]. Our measurements have been performed in VSM mode. In VSM mode, the sample is oscillated near the centre of the gradiometer, producing a voltage waveform of a parabola, such that the measured signal becomes a quadratic [171],

$$V(t) \approx Cz^2, \tag{2.58}$$

where C is the amplitude of the response, which is then converted into a magnetic moment via a system-dependent calibration factor and z is the time dependant sample position given by,

$$z = A\sin(\omega t), \tag{2.59}$$

where the angular frequency is $\omega = 2\pi f$ and A is the amplitude. This leads to a voltage waveform of,

$$V(t) \approx CA^2 \sin^2 \omega t \approx \frac{CA^2}{2}[1 - \cos 2\omega t]. \tag{2.60}$$

. The physical origin of 2ω is that the sample will pass by minimum and maximum twice during each oscillation period. Measuring in VSM mode allows for several advantages. Mechanical noise is mostly linked to ω and so by measuring 2ω this is largely ignored [171]. The signal is proportional to A^2, meaning for a sample where there is a weak magnetisation, the oscillation amplitude can be increased to increase the strength of the voltage signal. Measurements can be taken very rapidly, where we typically use a one-second averaging time per point. All our measurements were taken with a 4 mm amplitude and 14 Hz frequency. The custom VSM at the University of York has been used for angular-dependent measurements. These measurements were performed by Dr. Stuart A. Cavill, University of York, School of Physics, Engineering and Technology. For these measurements, the sample rod rotates such that the field is orientated between the sample plane at 0° and along the surface normal at 90°.

When determining magnetisation it is normally important to consider the demagnetisation field, as this can dramatically affect the true field felt by the sample. For all VSM measurements where we present values for the magnetisations, the field H applied was in-plane, where the demagnetisation field in thin films is small or negligible [12], and so is not considered in this section.

2.4.2 Data reduction

With real samples, multiple layers lead to multiple magnetisation dynamics. For example, a ferromagnetic layer may be placed on a paramagnetic or diamagnetic substrate, these effects are shown in figure 2.13. Any VSM measurements would be sensitive to all magnetisation dynamics and so need to be separated through data reduction. Figure 2.13 d) and e) shows for combined paramagnetism/diamagnetism and ferromagnetic,

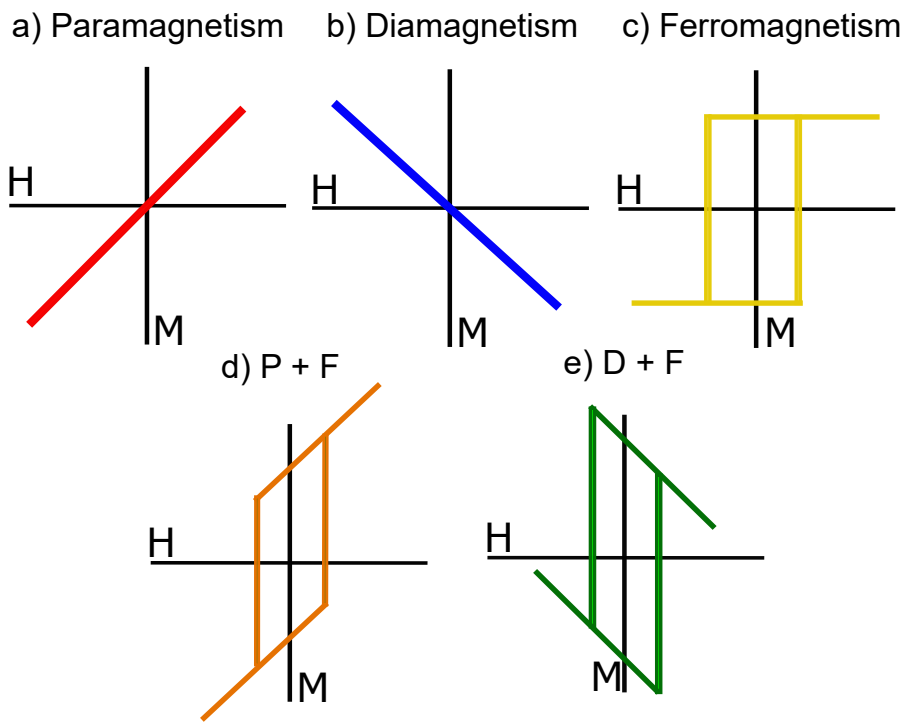

Figure 2.13: M vs H diagrams for various magnetisation dynamics. P/D + F represents the combined paramagnetic/diamagnetic and ferromagnetic responses.

once the sample is ferromagnetically saturated, the remaining slope is caused only by the paramagnetic or diamagnetic signal. To correct for these effects we calculate the gradient or susceptibility from data points at high fields above where the sample has ferromagnetically saturated. The susceptibility is then subtracted from the data. Diamagnetism is temperature independent [12] meaning it is best to take this magnetic susceptibility at room temperature. Paramagnetism is temperature dependent [12] and a magnetic susceptibility needs to be calculated at each given temperature. Once all present diamagnetic or paramagnetic susceptibilities have been removed, only the ferromagnetic response will remain.

Magnetisation values are typically presented in either emu/cc or μ_B/Formula Unit (F.U). To convert the magnetic moment measured from VSM into magnetisation, the sample volume needs to be calculated. For thin films, this volume is assumed to be a cuboid. To measure the surface area, a photograph of the sample is taken and then using the image processing software ImageJ [172], the number of pixels is counted and converted into an area. A systematic issue with this method is that the resolution of the camera, relative focus on the sample and shadowing effects from sample growth will all blur the edges of the sample, increasing the error on the measured area. The sample thickness can be taken from models of XRR, PNR or both fitted in parallel. As XRR is not sensitive to magnetisation, this technique is less ideal, especially for magnetic heterostructures as there can be regions of zero magnetisation which will be counted

towards the total magnetisation volume. PNR is clearly preferred as the exact volume of any regions of magnetisation can be taken. Using layer thicknesses taken from either XRR or PNR will introduce additional errors as the layers have uncertainty from the RMS roughness. Once the sample volume is known, the measured magnetic moment can be converted into emu/cm^3 or if the crystal formula unit cell is known, into μ_B/F.U.. For example, here we calculate the magnetisation for a CFO thin film with a surface area of 25 mm^2, a thickness of 300 Å and a measured moment of 1.5×10^{-4} emu. The sample volume is $7.5{\times}10^{-7}$ cm^3, giving a magnetisation of 200 emu/cm^3. To convert this magnetisation into μ_B/F.U., we used a conversion factor of C = $1.0783 \times 10^{20}\,\mu_B$/emu and one formula unit for CFO. CFO is FCC and has a lattice constant of 8.383 Å [14], giving a unit cell of 589 Å^3, which has 8 F.U. per unit cell, giving 74 Å^3/F.U. or 74 $\times 10^{-30}$ m^3/F.U.. The magnetisation emu/cm^3 is converted to meters by multiplying by $1/10^{-6} m^3/cm^3$ such that the units are $\frac{emu}{m^3} \times \frac{\mu_B}{emu} \times \frac{m^3}{F.U.} = \frac{\mu_B}{F.U.}$. This gives 1.58 μ_B/F.U. for this CFO thin film.

Before taking a measurement the sample must be aligned to the VSM pickup coils, such that the centre of the sample is aligned with the centre of coils at the middle point of oscillation. Any misalignment will lead to a reduced value in the measured moment. Misalignment is a larger concern during measurements involving large temperature variations, as this can lead to thermal expansion or contraction of the sample rod. To avoid this, the sample rod is typically made of a material with a low thermal expansion coefficient. A further correction can be made via a 'touch down' operation by the VSM. Here the sample rod makes contact with the base of the VSM, allowing for a measurement of its length. The normal sample rod length is known and so the expansion or contraction can be corrected without re-aligning the sample.

As such, even with the excellent sensitivity to magnetisation from SQUID VSM, the errors introduced from both misalignment and volume normalisation can lead to considerable uncertainties in the final values of magnetisation.

2.4.3 Calculation of coercive field, H_c

We measured VSM in field steps, often meaning we did not exactly measure the H_c, but slightly before and slightly after. The H_c was calculated from the x-intercept of a line plot between the last two points before and after H_c. To estimate the error on this value, we model a branch of the sample hysteresis loop with a sigmoid function combined with a linear polynomial, using the python programming language with the scipy.optimize.curve_fit function, we fit the model. With this model of the hysteresis loop, we then increase the point density to simulate a VSM measurement with a smaller field step size. The value of H_c from this simulation shows how much the measured H_c might have changed with a smaller field step size. We then took the difference between

the simulated VSM H_c with a high point density and the measured H_c as the error of H_c.

Chapter 3

$NiFe_2O_4$ and $CoFe_2O_4$ single film experiments

In this chapter, we investigate thin films of $CoFe_2O_4$ (CFO) and $NiFe_2O_4$(NFO) grown on Al_2O_3 (ALO). C17, C49, N20 and N45 are single film CFO/ALO (174 Å ± 7 Å), CFO/ALO (491 Å ± 3 Å), NFO/ALO (199 Å ± 3 Å) and NFO/ALO (449 Å ± 8 Å), respectively. Film thicknesses are not nominal, but taken from PNR measurements in section 3.2. We have investigated these films both to observe how growth on ALO will affect their structural and magnetic properties and to characterise these films for later growths in magnetic heterostructures.

3.1 X-ray diffraction measurements

The measured XRD of N20, N45, C17 and C49 are shown in figure 3.1. Only NFO and CFO [111] sample Bragg peaks were present in the measured 2θ range of 6° to 100°, showing all samples are [111] out-of-plane (OOP) and not amorphous or polycrystalline.

CFO and NFO have bulk lattice parameters of a_{CFO}= 8.383 Å [14] and a_{NFO}=8.346 Å [15], with expected [222] Bragg peaks of $2\theta_{CFO}$ = 37.123° and $2\theta_{NFO}$ = 37.292°. Using the Bragg scattering equation and method detailed in section 2.3.2, with Miller indices of [h k l] = [2 2 2] for a cubic system and a copper x-ray source of λ=1.5406 Å, we have calculated the lattice constants and strain of the films from the fitted peak values in table 3.1. These calculations show that N20, C49 and C17 are compressively strained between -0.376 % to -0.416 %, but N45 shows no strain within the detection limits of our experiment.

The -0.376 % to -0.416 % strain of N20, C17 and C49 is surprising as the ALO[001] surface has 8% mismatch on the O-O sublattice with the [111] plane in NFO and CFO, which was expected to lead to tensile strain [7, 25]. It's possible that the films are still

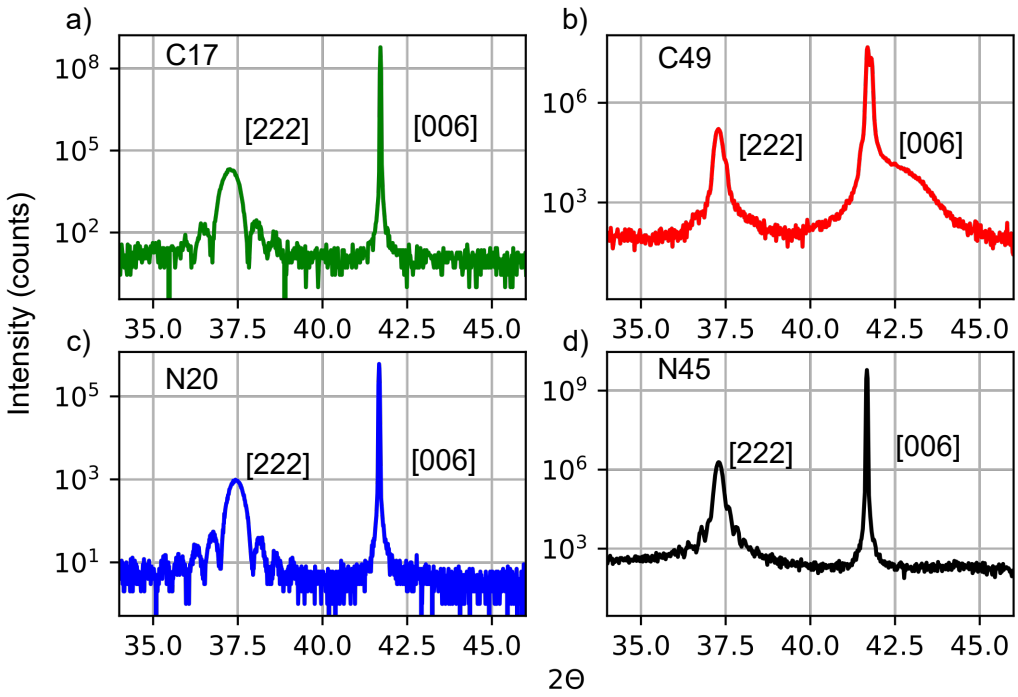

Figure 3.1: Intensity vs 2θ of N20, N45, C17 and C49 showing [222] NFO or CFO and [006] ALO peaks.

under tensile strain in-plane. If the volume of the unit cell has increased to accommodate this in-plane strain, then the z-axis would remain unchanged. As these samples present compressive strain in the z-axis, it is more likely that this axis has compressed to accommodate the in-plane tensile stain, meaning the volume of the unit cell is more likely to be unchanged. As the z-compression is much less than 8%, it's possible that these films reformed on the ALO surface via misfit dislocations, retaining a single-crystal order and weakening the effects of strain. N45 does not present a compression in its z-axis. It's possible that the strain has relaxed in the bulk of the N45 film, however, C49 is thicker and is still strained. Given the matching crystal structures and almost matching lattice constants of NFO and CFO, a difference in strain relaxation length between the CFO and NFO would be surprising. The volume of the crystal cell in N45 could be larger, but this is unlikely as a change in crystal volume is a strain effect, and so if no change in volume is present in the thinner N20, then it would be surprising to see this effect in a thicker sample.

Sample	[222] Bragg peak (2θ)	Lattice constant (Å)	Strain (%)
N45	37.298±0.001	8.346±0.001	-0.001
N20	37.443±0.001	8.315±0.001	-0.376
C49	37.287±0.001	8.348±0.001	-0.416
C17	37.283±0.001	8.349±0.001	-0.406

Table 3.1: Fitted peak values, lattice constants and strain values of thin film samples taken from XRD measurements.

By measuring the full-width half maximum of the [222] sample Bragg peaks and using the Scherrer equation from section 2.3.6, we have calculated the OOP coherent scattering length of the films, d_{coh}. For N45, N20 and C17 this gives a d_{coh} of 408Å ± 40 Å, 223 Å ± 22 Å and 228 Å ± 23 Å, respectively. By using the Laue interference function discussed in section 2.3.5, the Laue oscillations around the [222] Braggs peak have been simulated, giving an additional measurement of d_{coh}. Using this method we calculate a d_{coh} for N45, N20 and C17 of 434 Å ± 1Å, 201 Å ± 1 Å and 173 Å ± 1Å, respectively. For C49, the d_{coh} could not be calculated as this sample was not measured with a monochromatic optic, meaning its Bragg peaks are a combination of the $K_{\alpha 1}$ and $K_{\alpha 2}$ peaks from the copper X-ray source. This combination broadens the Bragg peak and Laue oscillations, meaning it is not possible to accurately estimate the FWHM or measure the Laue oscillations' periodicity. Additionally, there is a broad shoulder observed on the substrate peak which cannot be an effect of the combination of $K_{\alpha 1}$ and $K_{\alpha 2}$ peaks. This could be due to the angular range and detector acceptance, leading to an asymmetric omega integration.

3.2 Polarised neutron reflectivity measurements

PNR has been measured on C17, C49 and on N20 on D17 and N45 was measured using Super ADAM, descriptions can be found in section 2.2.7. Measurements were taken at room temperature (RT) with an applied field of B=1.48 T, shown in figure 3.2. The simplest and best models for C17 and C49 were single layers. The simplest and best models for N20 and N45 were two layers of different nuclear (N) and magnetic (M) SLDs.

The values of d_{coh} from N20 of 223 Å ± 22 Å and 201 Å ± 1 Å are in reasonable agreement with the thickness measured from PNR of 199 Å ± 3 Å, showing this sample has only one coherent crystalline growth region OOP. N20 shows a gradually increasing N-SLD profile from the substrate, up to a maximum value of 7.21 $10^{-6}/Å^2$, close to NFO's expected bulk N-SLD of 7.23 $10^{-6}/Å^2$ [145]. This gradient could be due to the effects of strain where the volume of the crystal cell has been reduced, reducing the N-SLD. However, it has already been discussed that a change in crystal cell volume for N20 is

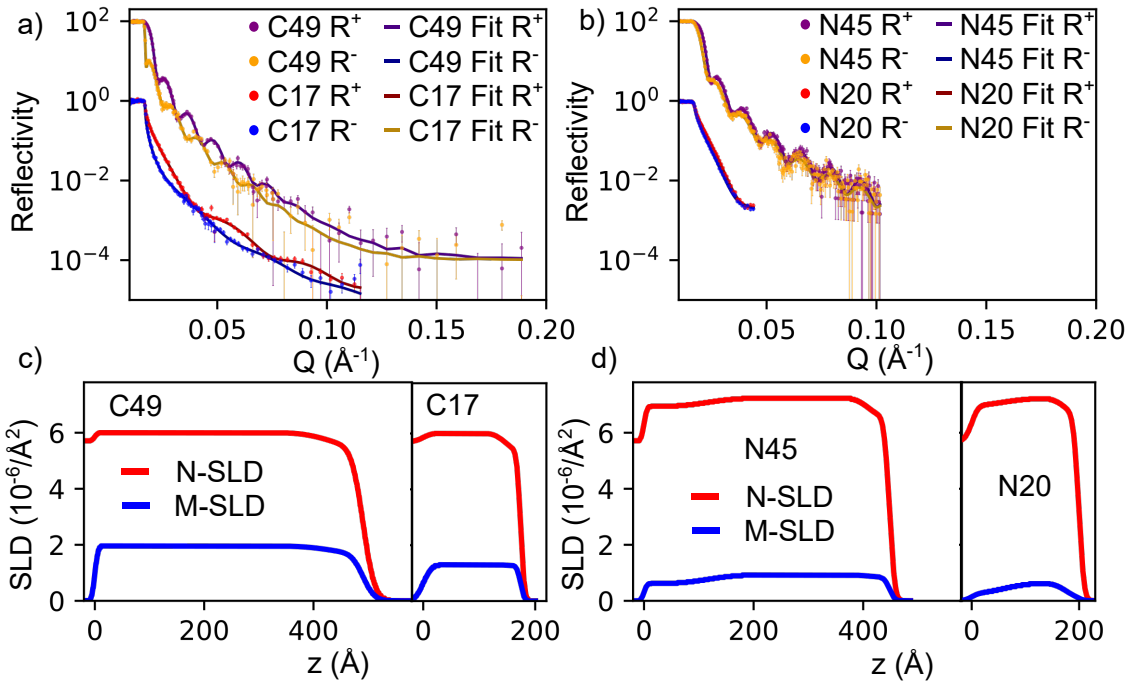

Figure 3.2: RT PNR with B = 1.48 T taken on a) C48 and C17 and b) N44 and N20, and modelled neutron-SLD (N-SLD) and magnetic (M-SLD) in c) and d). The reflectivity profiles of N45 and C49 have been scaled by a factor of 100 for clarity. All M-SLD profiles have been scaled by a factor of 2.

unlikely. It's possible the gradient is caused by chemical diffusion. Ni or Fe atoms could be missing from the initial growth. Oxygen is unlikely to diffuse away as all samples are oxides. It's possible that aluminium (Al) from the substrate has diffused into the NFO. Al has a smaller neutron scattering length of $b_n = 3.4$ fm, when compared to Ni with a scattering length of $b_n = 10.3$ fm [145]. The smaller b_n of Al would therefore lower the N-SLD. This gradient could also be caused by structural defects such as dislocations and anti-phase boundaries.

The values of d_{coh} from N45 of 408 Å ± 40 Å and 434 Å ± 1 Å are consistently shorter than the thickness measured by PNR of 449 Å ± 3 Å, with a maximum difference of 41 Å. PNR profiles are made up of Kiessig fringes, which are sensitive to changes in M and N-SLD, whereas the d_{coh} is the largest coherently scattering crystal domain. This suggests that there is an initial smaller growth phase of unknown quality, followed by a larger crystalline growth phase. PNR on N45 shows an 80 Å region of gradually increasing N-SLD profile from the substrate, up to a maximum value of 7.23 10^{-6}/Å^2, matching NFO's expected bulk N-SLD of 7.23 10^{-6}/Å^2 [145], which is then a ≈ 370 Å region of bulk NFO N-SLD. This is more evidence that N45 presents two crystalline growth phases.

As discussed, N45 does not appear to be strained along the z-axis. As N-SLD is the product of a material's nuclear scattering length and atomic density, the matching N-SLD of N45 to bulk NFO is further evidence that N45 does not present a change in the crystal

cell volume. Like N20, the differences in N-SLD in N45's initial growth region could be caused by several factors such as chemical diffusion and crystal defects. It's possible this initial region allows for the relaxation of N45's strain, leading to the difference in strain between N45 and the other films.

C17's value of d_{coh} from the Scherrer equation is 228 Å ± 23Å, from the measuring the Laue oscillations is 173 Å ± 1Å, and from PNR the sample thickness is 174Å ± 8Å . It is not possible that d_{coh} is larger than the thickness measured by PNR. The values of d_{coh} from the Scherrer formula can have large errors, discussed in section 2.3.6. The largest possible value of d_{coh} is 182 Å, meaning the error here using the Scherrer formula is at least 25 %. The d_{coh} from measuring the Laue oscillations is within the error of length measured with PNR, suggesting the sample is one coherent crystal OOP. C49 has an N-SLD of 6.01 10^{-6}/Å^2, 3 % below CFOs bulk expected value of 6.17 10^{-6}/Å^2. The film shows a uniform N and M-SLD, unlike the NFO films. This is surprising as both NFO films show a region of N-SLD gradient. If the gradient in NFO is caused by Al diffusion, we would expect there to be Al diffusing into the CFO. A difference in the number of crystal defects between C17 and the NFO films is possible but would be surprising given NFO and CFO have similar lattice constants and crystal structures.

From PNR C49 has a layer thickness of 491 Å ± 8 Å and an N-SLD of 6.01 10^{-6}/Å^2, the same as C17 and again 3 % below the bulk CFO value. Like C17, this film shows a uniform N-SLD, more evidence that the CFO films are behaving differently from the NFO films.

3.3 Magnetometry

Measured in-plane (IP) M vs H loops for C17, C49, N20 and N45 at various temperatures are shown in figures 3.4 and 3.3. Due to the high saturating fields of the samples, M_s values have been taken 0.2 T after the hysteresis loop closes, where the majority of the sample is assumed to have saturated.

Total layer thicknesses, magnetisation values and coercive fields extracted from PNR and VSM measurements are presented in table 3.2.

Sample	d (Å)	M_{sPNR} ($\mu_B/F.U.$)	M_{sVSM} RT ($\mu_B/F.U.$)	M_{sVSM}5 K ($\mu_B/F.U.$)	Hc RT (T)	Hc 5 K (T)
N45	449±3	1.11±0.10	1.01±0.1	-	0.0368 ± 0.0017	-
N20	199±3	0.57±0.20	0.60±0.02	1.30±0.02	0.0265 ± 0.0004	0.0980±0.0002
C49	491±8	2.50±0.08	2.65±0.01	-	0.0430±-0.0041	-
C17	174±7	1.78±0.08	2.05±0.01	2.80 ± 0.05	0.2384±0.0027	1.3417±0.0083

Table 3.2: Layer thickness, magnetisation values and coercive field of N45, N20, C48 and C17 taken from PNR and VSM measurements.

From table 3.2, both N45 and C49 show an increased M_s from both VSM and PNR when compared to their respective thinner samples, N19 and C17. This indicates a

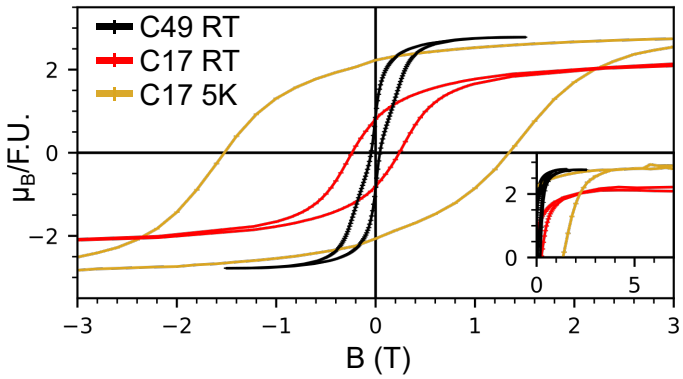

Figure 3.3: IP B vs μ_B/F.U. of C17 and C49 at various temperatures. The inset shows the top right branch of the hysteresis loop up to 7 T.

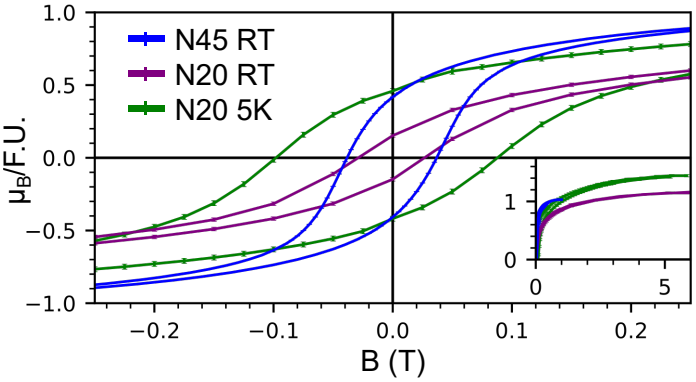

Figure 3.4: IP B vs μ_B/F.U. of N20 and N45 at various temperatures. The inset shows the top right branch of the hysteresis loop up to 6 T.

thickness dependence on the magnetisation of both NFO and CFO in our systems.

From table 3.2, both NFO films present a lower than bulk magnetisation compared to $2.3\mu_B$/F.U. [12]. The RT and 5 K hysteresis loops of N20 show an increasing magnetisation up to 6 T. Both sample measurements have been corrected for linear diamagnetism and paramagnetism, discussed in section 2.4.2, meaning this increasing magnetisation is ferromagnetic in nature. Bulk NFO is a soft magnet [173] which is expected to saturate below 1 T. This suggests that APBs are present [27], leading to very large saturating fields, discussed in section 1.3.2. APBs could then account for the lower magnetisation of both N20 and N45, as the values of M_s taken 0.2 T after the loop closed, where the samples are not saturated. The larger magnetisation of N45 compared to N20 could then be related to the defect density of APBs.

Crystal defects such as APBs were discussed as a reason why both N20 and N45 present regions of gradient N-SLD profiles. Figure 3.2 d) shows in the same region as the N-SLD gradients, a gradient in the M-SLD profiles in both NFO films. If APBs are causing this reduction in M-SLD and N-SLD, then a lower N and M-SLD implies a larger APB density. This would suggest that N20 has a higher APB density than N45,

as N45 has a large region of uniform N-SLD. VSM on N45 shows a larger magnetisation than N20, suggesting it was more easily saturated, supporting this argument. As the decreased N and M-SLD profiles are both at the interface with the ALO, this is evidence that APBs are being caused by the ALO surface. As discussed ins section 3.1, these films may have grown via misfit dislocations, which are likely to produce APBs, discussed in section 1.3.2,

Both CFO films present a lower magnetisation when compared to a bulk magnetisation of 3.70 μ_B/F.U. [12]. The high field measurements on C17 from figure 3.3 show this film's magnetisation does appear to ferromagnetically saturate, suggesting C17 does not have a large number APBs. This means the lower M_s could be due to other mechanisms. One possible explanation is the amount of cation inversion, which has been seen to lower the magnetisation of ferrites [121]. The larger magnetisation of C49 compared to C17 could then be explained by a difference in the inversion parameter or APBs, but it is not clear if this is a thickness-related effect or an interface effect.

If C17 is not presenting a large amount of APBs, this implies a difference in defect density between CFO and NFO. Both CFO films present uniform N and M-SLD profiles in figure 3.2 c), supporting this argument. This would be surprising, given both CFO and NFO has the same orientation, similar thicknesses, the same inverse spinel structure and very similar lattice constants (Δa/a =0.4 %). This could imply that there is a difference in the effect of the ALO interface between CFO and NFO.

From table 3.2, the increasing values of H_c with decreasing temperature of C17 and N20, with percentage increases of 116 % and 400 % respectively, are in line with experiments on similar ferrite systems [10, 174–178]. Experiments on thin film NFO systems have measured RT H_c values between 0.01 to 0.05 T [11], in agreement with the RT H_c of both N20 and N45.

CFO has bulk H_c values of H_c (5 K) = 2.5 T and H_c (300 K) = 0.53 T [179], as such both C17 and C49 show significantly lower H_c values than bulk CFO. The strain is weak in these films (< 0.5 %), and so the stress anisotropy term is weak and unlikely to have a large effect on the H_c. It's possible these films have a weaker magnetocrystalline anisotropy constant when compared to bulk.

Angular-dependent (AD) VSM has been measured on C17 and C49, shown in figure 3.5, with 0° representing an IP field and 90° OOP. From table 3.3, C49 shows an increasing H_c and decreasing M_r/M_s with increasing angle. C49 at 0° presents a saturating field, H_{Ms}, of 0.72 T vs 1.52 T for 90°. The comparatively lower M_r/M_s and saturating field when comparing IP vs OOP indicates an easier IP axis. This easier IP axis could be due to the effect of stress and shape anisotropy. CFO's single crystal magnetostricion constants are λ_s^{100}=(-223 to -590) and $\lambda_s^{111} \approx -1/5\lambda_s^{100}$ [99]. The film is compressively strained by -0.416 %, giving a negative sign to σ. The stress anisotropy for the [111] direction will therefore have a negative sign from multiplying the negative σ with the

Angle (degrees)	C49 Hc (T)	C17 Hc (T)	C49 Mr/Ms	C17 Mr/Ms
0	0.0430±0.004	0.2384±0.0027	0.312	0.380
15	0.0411±0.0041		0.305	
30	0.0434±0.0022		0.292	
45	0.0498±0.0014	0.2007±0.0068	0.269	0.330
60	0.0605±0.0012		0.229	
75	0.0740±0.0088		0.173	
90	0.1080±0.0061	0.1752±0.0054	0.153	0.256

Table 3.3: RT H_c and remanence $(M_r)/M_s$ values for C49 and C17 taken from AD VSM.

positive λ_s^{111}. As discussed in section 1.2.3, a negative sign of stress anisotropy will promote an easy IP axis. Shape anisotropy in a thin film will also promote an IP easy axis. CFO has a bulk magnetic easy axis in the [100] direction [98]. In our coordinates system, normal to the [111] plane is 90° meaning the [100] direction makes a 54.73° with the [111] direction, such that the [100] direction is at 35.27° away from the sample plane, meaning the [100] easy direction is closer to IP then OOP. This means stress, shape and magnetocrystalline anisotropy promote an easier IP axis.

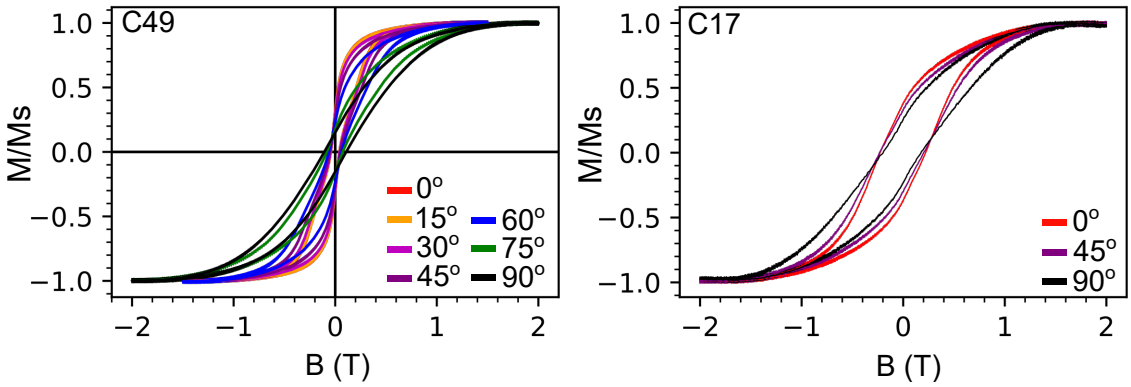

Figure 3.5: Angular dependant VSM measured on C49 and C17 at RT. 0° is IP and 90° is OOP. Measured by Dr Stuart A. Cavill at the University of York.

C49 shows an IP narrowing of its hysteresis loop, lowering its H_c value when compared to both bulk CFO with a H_c of 0.53 T [179] and C17, where C17 has an IP H_c that is 820 % larger. The H_c values of C49 in table 3.3 show this narrowing remains relatively unchanged between 0° to 45°, but weakens significantly up to 90°. It's possible this effect is caused by CFO's bulk magnetic easy axis, or by stress anisotropy. The CFO bulk easy axis lies at ⟨100⟩ direction at 35.27° from the sample plane. It is possible that this narrowing loop is CFO's magnetisation rotating into its easy direction as the field approaches zero. Once the angle is above 60°, the magnetisation is rotating too far from the easy axis, causing the increase in H_c and high OOP saturating fields seen in figure 3.5. However, experiments on thin film epitaxial [001] oriented CFO grown on $SrTiO_3$ have also shown a narrowing of CFO's hysteresis loop [180], meaning this narrowing cannot be

CFO rotating into its easy direction. This narrowing was attributed to stress anisotropy [180], as our sample is also strained, our measurements support this argument but is surprising given the small amount of stress ($< -0.5\,\%$). In these experiments, CFO's loop narrowing was found to have a thickness dependence. Interestingly in the thinner C17, the OOP direction shows a narrowing towards the centre, unlike C49 which has an IP narrowing. As C17 and C49 are strained by the same amount, this is evidence that this effect is also thickness related.

From table 3.3, C17 presents a decreasing H_c and M_r/M_s with increasing angle, with a H_{Ms} of 1.35 T at 0° vs 1.65 T at 90°. This suggests an easier IP direction in C17, however, figure 3.5 shows that IP and OOP directions have similar hysteresis loops, suggesting IP vs OOP anisotropy is weak in C17, and weaker compared to C49 in figure 3.5.

RT angular dependent VSM (AD VSM) has been measured on N20 and N45, shown in figure 3.6, with 0° representing an IP field and 90° OOP. The H_c values of N45 in table 3.4 shows increasing H_c values from 0° to 45°, which then decreases such that the H_c of 0° is close to 90°, showing no strong anisotropy between IP and OOP. The M_r/M_s values from table 3.4 decrease with increasing angle and the H_{Ms} at 0° is 0.39 T vs 0.54 T, for 90°, suggesting an easier IP direction for N45. Bulk NFO has an easy [111] direction [114]. As such this easier IP direction is likely the effect of shape anisotropy, discussed in section 1.2.3.

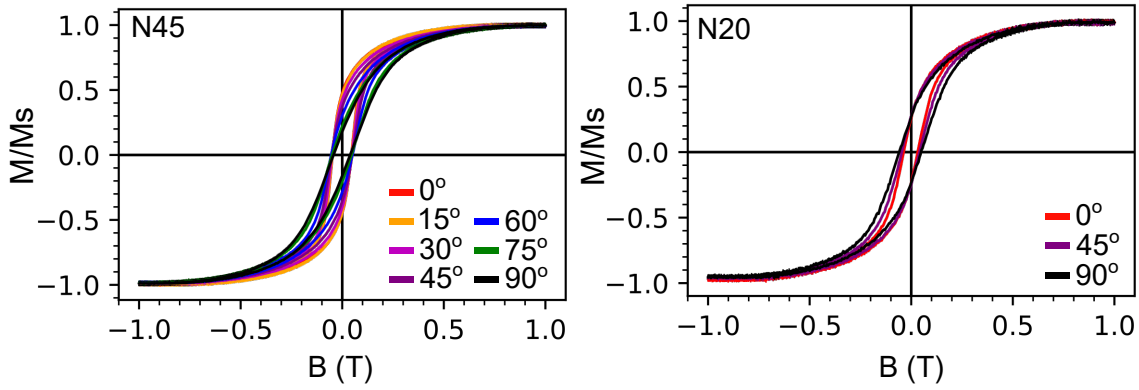

Figure 3.6: Angular dependant VSM measured on N45 and N20 at RT. 0° is IP and 90° is OOP. Measured by Dr Stuart A. Cavill at the University of York.

For N20, table 3.4 shows minor differences between M_r/M_s with increasing angle. figure 3.6 shows similar hysteresis loops for 0° compared to 90°. This shows that the anisotropy between IP and OOP in N20 is weak. As Bulk NFO has an easy [111] direction [114], for a [111] oriented film it can be expected that IP and OOP are both easy directions, however, it is surprising as it means shape anisotropy is weak and weaker than in N45. NFO does not have large magnetostriction constants, discussed in section 1.3.3, meaning the stress anisotropy term will be weak and so unlikely to have a large effect.

Angle (degrees)	N45 Hc (T)	N20 Hc (T)	N45 Mr/Ms	N20 Mr/Ms
0	0.0368±0.0070	0.0265±0.0004	0.479	0.254
15	0.0456±0.0009		0.465	
30	0.0476±0.0010		0.425	
45	0.0500±0.0017	0.0317±0.0060	0.373	0.279
60	0.0509±0.0012		0.304	
75	0.0457±0.0018		0.222	
90	0.0389±0.0001	0.0482±0.0013	0.178	0.268

Table 3.4: RT H_c and M_r/M_s values for C49 and C17 taken from AD VSM.

In figures 3.5 and 3.6, the thinner samples C17 and N20 do not show a strong IP or OOP easy axis, whereas for the thicker samples C49 and N45, a clear IP easier axis develops. As discussed, in the CFO films the stress anisotropy is expected to promote an IP easy axis and similarly from section 1.3.3, NFO has a negative magnetostriction in the [111] direction and so stress anisotropy would also promote an IP easier axis in the NFO films. Stress anisotropy is an interface effect, meaning it should be stronger in the thinner films, however, the thicker films present an easier IP axis, meaning this effect is unlikely to be stress anisotropy. This could suggest that as both NFO and CFO films are increasing in thickness, their magneto-crystalline or shape anisotropy is becoming stronger.

3.4 Summary

This chapter aimed to investigate how growth on ALO would affect the structural and magnetic properties of thin film CFO and NFO.

XRD showed all films present [111] OOP orientation. N20, C17 and C49 experienced between -0.376 % to -0.416 % compressive strain along the z-axis. This was much lower than the 8 % mismatch from the ALO[001] surface for the NFO and CFO [111] directions, which was expected to lead to tensile strain. The compressive strain in the z-axis is evidence that the volume of the crystal cell has remained unchanged, where the lower than 8 % strain could be explained by misfit dislocations during the film's growth. N20, C17 and C49 show a d_{coh} which agrees with the layer thicknesses measured by PNR, showing that they are a single coherent crystal OOP. N20 showed a gradient of M and NSLD profile, which could be due to effects such as chemical diffusion and crystal defects.

N45 did not present any strain and showed a d_{coh} up to 41 Å shorter than the sample length measured by PNR. These effects were attributed to two growth regions in N45. The initial region presented a lower N-SLD, similar to N20, where potential effects such as chemical diffusion, crystal defects and strain relaxation are present. In the second growth region, the strain has relaxed, and NFO presents its bulk [111] unstrained Bragg peak and N-SLD value.

Both CFO films presented uniform N-SLD profiles, unlike the NFO films, suggesting a difference in growth between the materials. This difference could be, for example, the defect density close to the substrate.

Both N20 and N45 showed a lower than bulk magnetisation for both samples and a large saturating field, which was attributed to the presence of APBs, which was more evidence that crystal defects are present and linked to the gradient M and N-SLD profiles in both films. Both C17 and C49 showed a lower than bulk magnetisation for both samples, which could be attributed to APBs or cation distribution. VSM on C17 showed that this sample did not experience a large number of APBs, more evidence that the CFO films present fewer crystal defects than the NFO films.

C49 shows a narrowing of its hysteresis loop between 0° to 60°, which is attributed to the effects of strain anisotropy, with C17 showing a narrowing hysteresis loop OOP, indicating a potential thickness dependence on this effect.

The thinner samples C17 and N20 do not show a strong IP or OOP easy axis, whereas the thicker samples C49 and N45 present an easier IP axis. This suggests that as both NFO and CFO films are increasing in thickness, their anisotropy is becoming stronger.

Chapter 4

$NiFe_2O_4$ and $CoFe_2O_4$ bilayer effects investigation

This chapter investigates thin film CFO/NFO bilayers. N27C26 and C19N21 are ALO [001] grown bilayers of NFO (272 Å ± 3 Å)/ CFO (255 Å ± 3 Å)/ ALO and CFO (194 Å ± 2 Å)/ NFO (212 Å ± 2 Å)/ALO, respectively. Sample thicknesses are taken from PNR and XRR measurements in section 4.3. The motivation for changing the layer order, such that we grew ALO/CFO/NFO and ALO/NFO/CFO, was to investigate both the influence of the top layer vs ALO/CFO and ALO/NFO films and how the layer order reversal affects these materials.

4.1 X-ray diffraction measurements

Figure 4.1 shows measured XRD on N27C26 in a 2θ range of 78° to 81°. Two peaks can be seen which represent the [444] Bragg reflections for CFO and NFO, with 2θ values of 79.281° ± 0.002° and 79.674° ± 0.002°, respectively. This gives lattice constants for CFO and NFO of 8.365 Å ± 0.002 Å, and 8.331 Å ± 0.002 Å, which compared to the bulk values of a_{CFO}= 8.383 Å [14] and a_{NFO}=8.346 Å [15], shows strains of -0.210 % and -0.181 %, respectively. These strain values are both lower then single films N20, C17 and C49 (all > 0.3 %), and above N45 (0.001 %). Given CFO is grown on ALO in this bilayer and has a thickness between C17 and C49, it's surprising that the strain is less. This could suggest the NFO growth is affecting the CFO layer.

Figure 4.2 shows measured XRD on C19N21 from a 2θ of 36° to 39°. A single peak can be seen at 37.243° ± 0.001°, which is the combination of the [222] Bragg reflections of the CFO and NFO [222] peaks, with bulk values of $2\theta_{CFO}$ = 37.123° and $2\theta_{NFO}$ = 37.292° [14, 15]. This peak gives a lattice spacing of 8.357 Å ± 0.001 Å. To estimate the strain from the two superimposed peaks, we have averaged the bulk lattice constants of NFO and CFO, giving 8.365 Å, meaning an average lattice strain between the two films

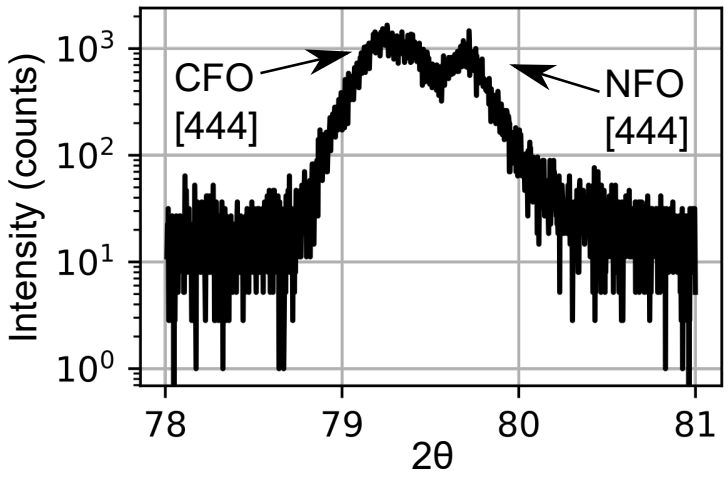

Figure 4.1: Measured XRD on N27C26 showing the [444] NFO and CFO Bragg reflections.

of -0.094 %. This is lower then the average strain from N27C26 (-0.196 %), and lower than the strain of N20 (-0.376 %). Interestingly this could indicate a similar effect as seen in N45, where an initial region of NFO might have allowed for strain relaxation. The low strain in both bilayers indicates a similar growth to the single films from Chapter 3, potentially indicating the layer grown on ALO in both bilayers has grown via miss-fit dislocations. Laue oscillation can be seen on the shoulders of the Bragg reflections. These oscillations have been simulated, giving a d_{coh} of $407\,\text{Å} \pm 1\,\text{Å}$.

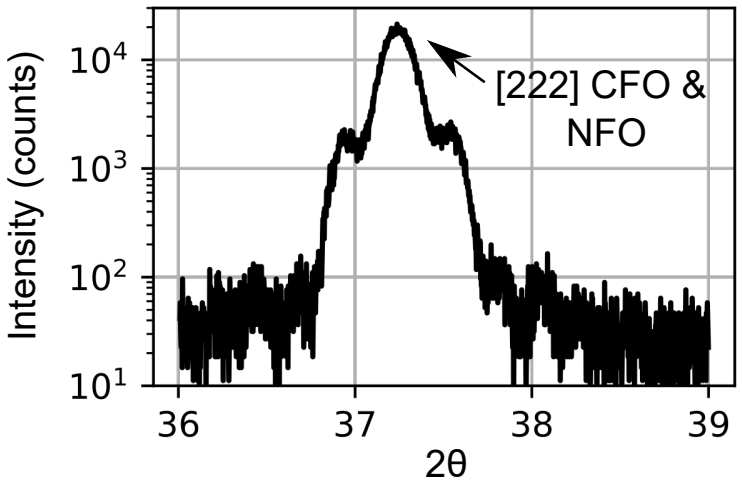

Figure 4.2: Measured XRD on C19N21 showing a combined [222] CFO and NFO Bragg reflection.

4.2 Magnetometry measurements

Measured M vs H loops for C19N21 and N27C26 taken at room temperature (RT) and 5 K can be seen in figures 4.3 and 4.4. Due to the high saturating fields of the samples,

M_s values have been taken 0.2 T after the hysteresis loop closes, where the majority of the sample is assumed to have saturated. Values of M_s and H_c can be seen in table 4.1, values for C17 and N20 have been added for comparison as their layer thickness are similar to individual layers in the bilayers.

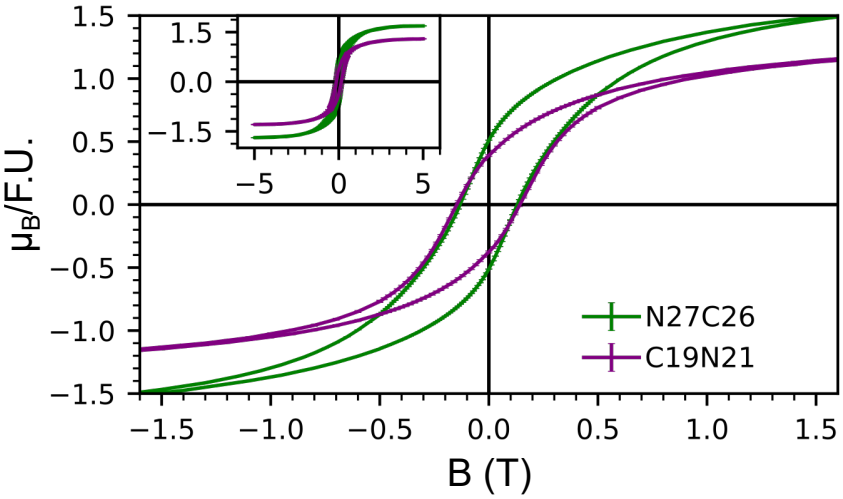

Figure 4.3: In-plane magnetic moment (μ_B/F.U.) vs applied field (T) hysteresis loops of N27C26 and C19N21 at room temperature, with an inset showing the fully measured field range.

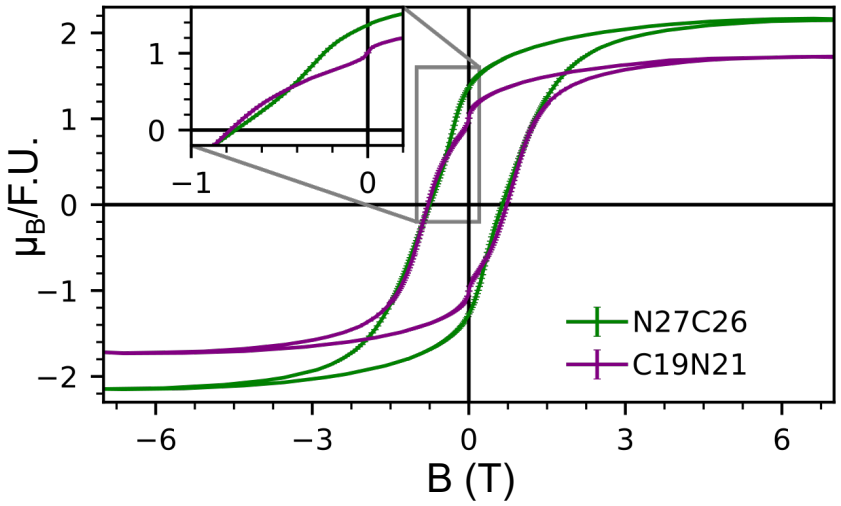

Figure 4.4: In-plane magnetic moment (μ_B/F.U.) vs applied field (T) hysteresis loops of N27C26 and C19N21 at 5 K, with an inset showing where the loops present a step.

Both bilayers at RT present single-step s-shaped hysteresis loops, suggesting rigid exchange coupling, discussed in section 1.2.4. Interestingly both bilayers at 5 K present a two-step hysteresis loop. For C19N21 the step is at zero-field and for N27C26 the step is at 0.4 T. This suggests part of the soft layer is able to nucleate away from the hard

layer. This implies that the bilayers are rigidly coupled at RT and not rigidly coupled at 5 K. It's also possible that a step is present at RT, but is too small to see, then once the samples are cooled down to 5 K, the larger difference in H_c values of CFO and NFO makes this step visible.

From section 1.2.4, rigidly coupled systems should present magnetic properties which are the average of the two layers. To approximate this average we calculated the H_c of a 1:1 ratio bilayer based on C17 and N20 at RT and 5 K. At RT the H_c of the 1:1 bilayer is 0.133 T, above N27C26's and C19N21's RT H_c by 0.005 T and 0.007 T, respectively, showing reasonable agreement. This is more evidence that the layers are rigidly coupled at RT. At 5 K, we calculate for the 1:1 bilayer a H_c of 0.720 T. This is above N27C26's H_c by 0.08 T. This indicates N27C26 is presenting a lower H_c when compared to our estimate of a rigidly coupled system. It's possible that NFO is above the critical thickness for rigid coupling, δ_{cs}, as soft layers above δ_{cs} lower the coercivity of the hard layer when compared to a rigidly coupled system, and as such the overall bilayer, discussed in section 1.2.4. The H_c of the 1:1 estimate at 5 K is below C19N21s 5 K H_c by 0.008 T, showing reasonable agreement. Interestingly this indicates rigid coupling. It's also possible that the anisotropy, and therefore H_c, of CFO in this bilayer has been modified due to the growth on the NFO [111] surface when compared to the strained ALO [001] growth surface for CFO in C17. This would mean the 1:1 bilayer estimate is wrong.

Table 4.1 shows that N27C26 has a higher M_s than C19N21 at both temperatures. This indicates that when grown on the ALO [001] surface compared to either the CFO or NFO [111] surface, at least one of the films is showing a change in magnetisation.

Sample	Ms (μ_b/F.U.) RT	Ms (μ_b/F.U.) 5 K	Hc (T) RT	Hc (T) 5 K	% Hc diff RT vs 5 K
C17	2.05 ± 0.06	2.80 ± 0.06	0.238 ± 0.003	1.342 ± 0.008	464%
N20	0.60 ± 0.02	1.30 ± 0.02	0.027 ± 0.001	0.098 ± 0.001	263%
C19N21	1.54 ± 0.05	1.64 ± 0.05	0.140 ± 0.002	0.728 ± 0.001	420%
N27C26	2.00 ± 0.06	2.16 ± 0.06	0.128 ± 0.001	0.640 ± 0.002	400%

Table 4.1: Measured saturation and coercive field values from thin film and bilayer samples at RT and 5 K.

4.3 Reflectivity measurements

To observe the structure of the bilayers and the saturation magnetisation's of CFO and NFO in the bilayers, both samples were measured with PNR at a saturating field (B = 1.5 T at RT and B = 2.2 T at 5 K) and XRR at RT and no field. A structural model was then co-fitted from both PNR at M_s and XRR. To discern how NFO and CFO were behaving during magnetic switching in the bilayers, field reversal was applied to both samples (B = 1.5 T to -1.5 T for RT and B = 3 T to -3 T at 5 K), and then measurements

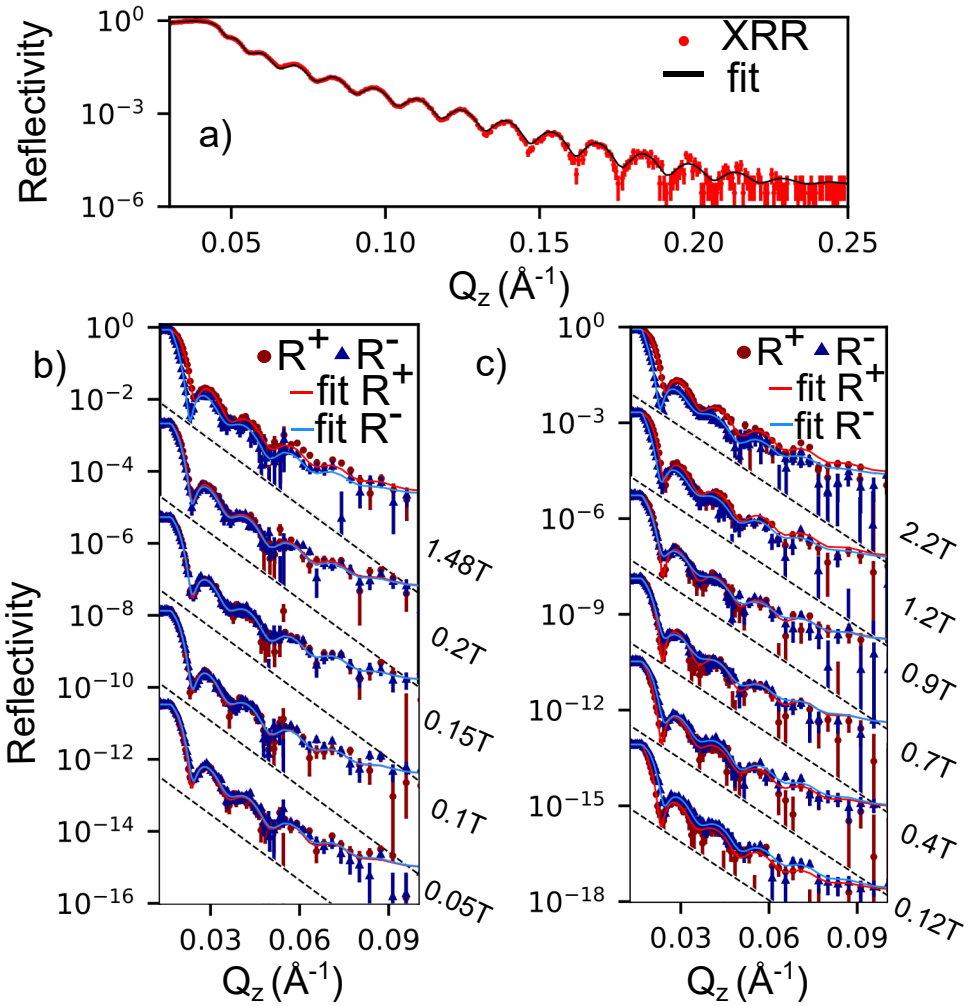

Figure 4.5: C19N21 measured (symbols) and fitted (solid lines) a) XRR and b) and c) PNR curves as a function of momentum transfer (Q_z) on a logarithmic scale. PNR was measured at b) RT and c) 5 K. Neutron reflectivity profiles have been shifted along the vertical axis and separated by dashed lines for clarity.

were taken in a region starting close to zero field and ending after the coercive field (B=0.05 to B=0.2 T at RT and B=0.12 up to B=1.2 T for 5 K). This data was then fitted with the structure obtained from fitting at M_s. Figures 4.5 and 4.6 show fitted XRR and PNR profiles from C19N21 and N27C26 at RT and 5 K (neutrons only) as a function of momentum transfer Q_z.

For C19N21 the best and most simple model was, starting from the substrate, a layer of NFO and then a layer of CFO. This structural model showed a $FOM_{sintth4} = 1.8991^{-17}$ for a parallel fit of RT and 5 K PNR measured at M_s and XRR and was not significantly decreased by the addition of more layers. For N27C26 the best and most simple model was, starting from the substrate, a layer of CFO, then an intermediate layer and then a layer of NFO. This structural model showed a $FOM_{sintth4} = 4.2419 \times 10^{-17}$, whereas a two-layer model without an intermediate layer shows $FOM_{sintth4} = 4.9137 \times 10^{-17}$, showing the intermediate layer improves the fit. Both models were fitted with five

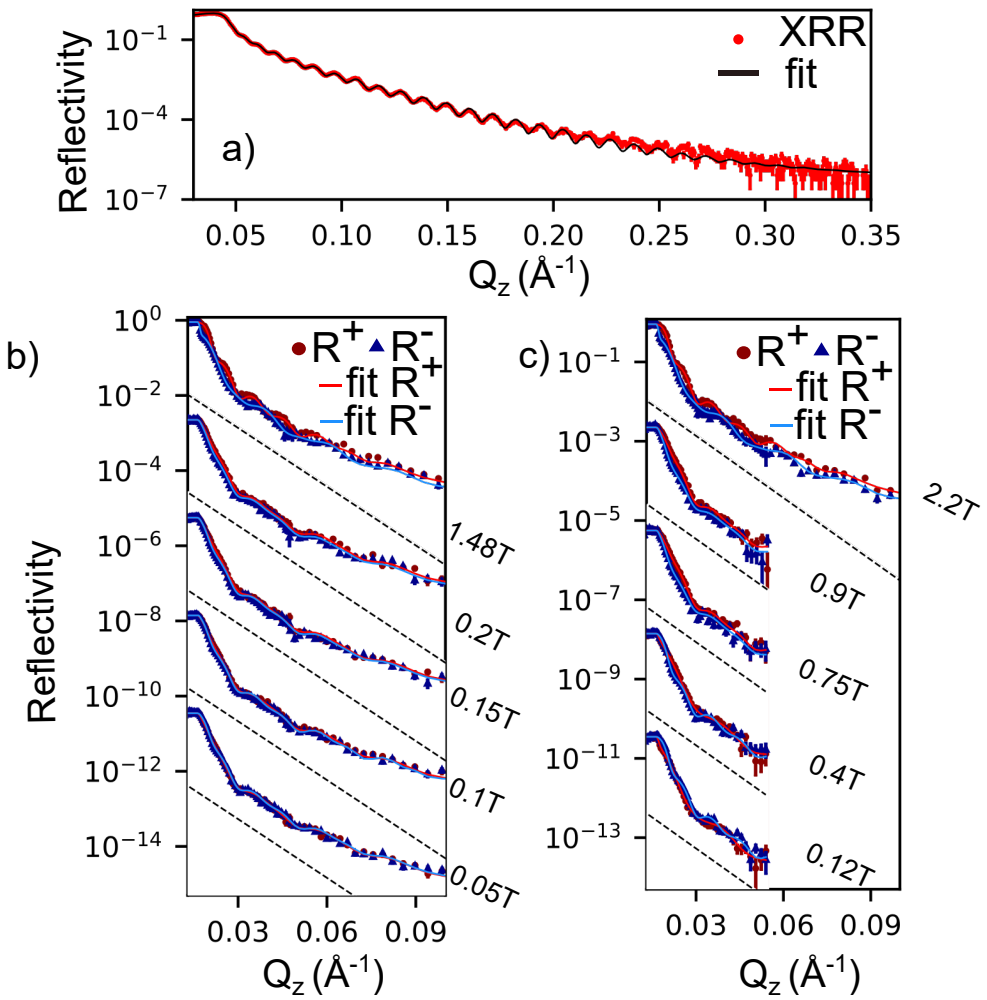

Figure 4.6: N27C26 measured (symbols) and fitted (solid lines) a) XRR and b) and c) PNR curves as a function of momentum transfer (Q_z) on a logarithmic scale. PNR was measured at b) RT and c) 5 K. Neutron reflectivity profiles have been shifted along the vertical axis and separated by dashed lines for clarity.

independent regions of magnetisation. In both samples, more regions of magnetic freedom were given to the bottom layer when compared to the top (3 vs 2). This is to allow for the modelling of magnetic effects from the substrate interface and the CFO/NFO interface in the bottom layer. The widths of the five magnetic regions were fitted parameters in the model. The widths of the magnetic regions in N27C26 are, starting from the substrate, 88 Å, 116 Å, 51 Å, 96 Å and 177 Å. In C19N21 the widths of the five magnetic regions are, starting from the substrate, 63 Å, 80 Å, 71 Å, 59 Å and 136 Å. The limit of only 5 magnetic layers, each connected by roughness profiles restricted to less than half their widths, leads to nonphysical steps in the magnetisation in the model.

The models SLD and M-SLD have been sliced into layers during fitting. The layers have a minimum width of 0.5 Å, however, if the deviation in SLD between slices is smaller than $0.002^{-6}/Å^2$ then the layers are combined.

The root mean squared (RMS) roughness of C19N21 at the CFO/NFO interface is

modelled by a single step profile of 34.9 Å ± 0.2 Å. N27C26 roughness was modelled with a two-step profile of 11 Å ± 1 Å for the first step and then a roughness of 24.98 Å ± 0.06 Å for the second step, making total roughness for the two steps of 35 Å ± 1 Å. This shows that the heterostructures have very similar overall roughness at the CFO/NFO interface, but with different roughness profiles.

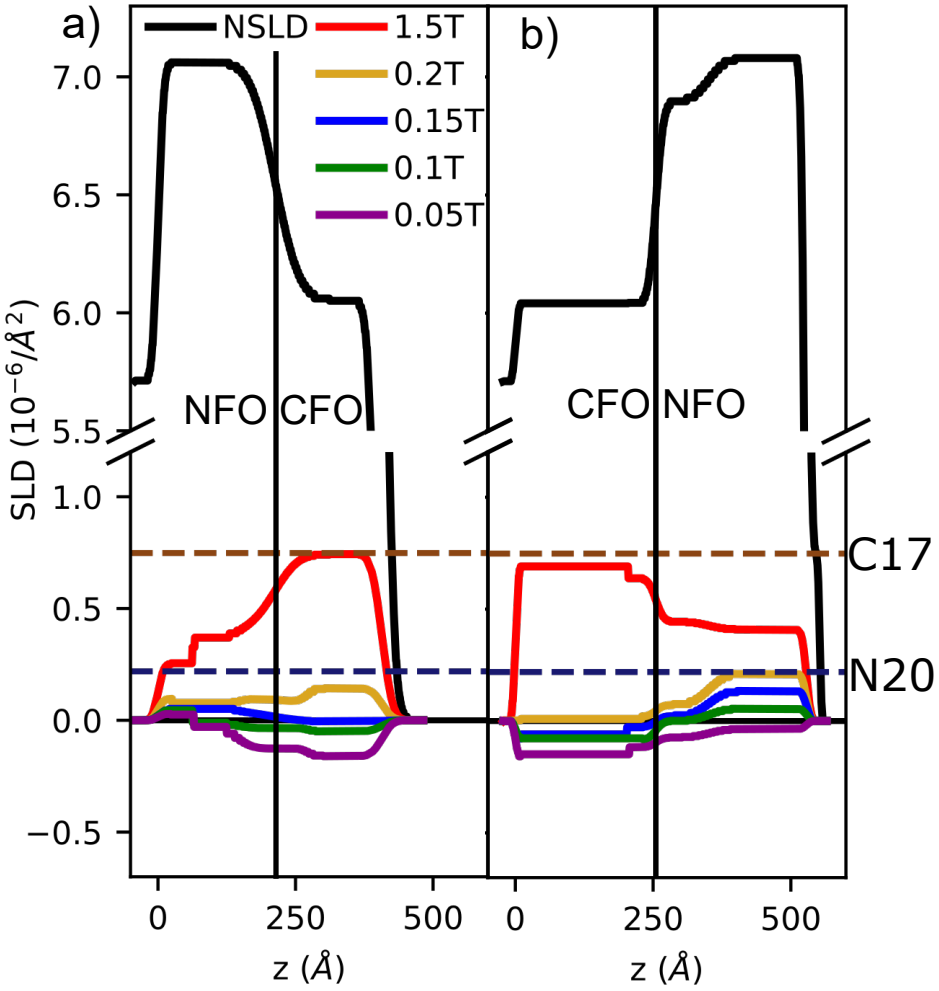

Figure 4.7: Modelled SLD profiles (black) and M-SLD profiles (coloured lines) after field reversal at 1.5 T for C19N21 (a) and N27C26 (b), measured at RT. Dashed lines show converted μ_B/F.U to M-SLD values for VSM of C17 and N20 at 1.5 T. and RT.

4.4 Room temperature magnetisation effects

Here we discuss the saturation measurements of the bilayers at RT to see what effect the strain imposed by the substrate has on the different ferrites. Indications for this were presented in Chapter 3, but here we are interested in the impact on the upper layer.

The M-SLD of C19N21 at RT and B = 1.5 T is shown in figure 4.7 (a). Starting at the substrate, NFO's initial 63 Å magnetic region presents an M-SLD of 0.254 10^{-6}/Å^2.

This is very similar to N20s RT M-SLD of $0.219\,10^{-6}/Å^2$. In Chapter 3, N20 presented a gradient in N and M-SLD profiles, indicating potential chemical diffusion or a large number of crystal defects such as APBs. NFO in C19N21 presents a uniform N-SLD of $7.060\ 10^{-6}/Å^2$, a 2 % difference to NFO's bulk value of $7.23\ 10^{-6}/Å^2$ [145], meaning large amounts of chemical diffusion are unlikely. A large am of APBs could be present in this region close to the ALO interface, similar to the effects discussed in Capter 3, causing this initial region to not saturate, lowering the magnetisation projection seen by PNR. Interestingly, the following 78 Å region in NFO is flat with an M-SLD of $0.369\ ^{-6}/Å^2$ and the next 70 Å region leads into the roughness profile towards the NFO/CFO interface, with a maximum M-SLD of $0.411\,10^{-6}/Å^2$. This shows a magnetisation gradient which extends beyond the chemical roughness into NFO. This indicates the CFO layer is affecting NFO's magnetisation. The VSM measurements have shown that CFO and NFO are magnetically coupled in C19N21. The coupling at the NFO/CFO interface could then align the magnetisation of NFO to the applied field. This effect decreases with increasing distance from the interface, leading to a magnetic gradient in the NFO.

In contrast in N27C26 at B = 1.5 T (b) where the NFO layer is weakly strained (-0.196 %) there is a more uniform M-SLD profile, where after the chemical roughness, it presents an M-SLD of $0.409\ \ 10^{-6}/Å^2$. If we compare this value to the three NFO magnetic regions in C19N21, their percentage differences are -38 % for the initial region, -10 % for the middle region and 0.5 % for the final region. This shows that at 1.5 T, NFO in C19N21 has a lower magnetisation than in N27C26.

In both bilayers at RT and 1.5 T, NFO presents a lower M_s than the experimental bulk value of $0.840\ 10^{-6}/Å^2$ (2.4 μ_B/F.U.) [12], indicating all films are potentially presenting APBs. The difference in magnetisation for NFO between the bilayers could then be explained by a difference in APB density between the films. It was indicated in Chapter 3 that NFO presents a higher APB density closer to the ALO interface. NFO in C19N21 grew on the ALO [001] surface, whereas NFO in N27C26 grew on the almost perfectly lattice-matched CFO surface ($\Delta a < 0.4\,\%$). This difference in growth surface could explain a difference in APB density between the films, which is more evidence that the ALO interface is having a large effect on the APB density in NFO.

The M-SLD profiles of CFO at 1.5 T in C19N21 (a) and N27C26 (b) are flat after the structural roughens, with M-SLD values of $0.743\ ^{-6}/Å^2$ and $0.691\,10^{-6}/Å^2$ respectively. These values are below CFO's bulk magnetisation of $1.351\ \ 10^{-6}/Å^2$ ($3.70\mu_B$/F.U.)[12]. CFO in both bilayers presents a similar value of M-SLD compared to C17's M_s at RT of $0.748\,10^{-6}/Å^2$, suggesting a similar growth quality. In chapter 3 it was suggested that CFO is presenting APBs, but with a lower density than compared to NFO, meaning another mechanism was also responsible for the lower than bulk magnetisation of CFO. CFO shows an increase in magnetisation of 8 % going from C19N21 to N27C26, much lower than the percentage difference seen in NFO. The lower impact of changing growth

surface for CFO magnetisation compared to NFO is more evidence that NFO is more affected by the ALO growth surface than CFO, discussed in Chapter 3.

The VSM results showed that N27C26 has a higher M_s than C19N21, indicating at least one of the layers was presenting a different magnetisation depending on the layer order. By integrating the M-SLD values from PNR at RT and 1.5 T in figure 4.7, we calculate magnetisations for N27C26 and C19N21 of 1.47 μ_B/F.U. and 1.38 μ_B/F.U, respectively. This confirms that at RT, N27C26 presents the largest magnetisation of the two bilayers from both VSM and PNR. As CFO's magnetisation is weakly affected by layer order reversal, the difference in magnetisation between the bilayers can be explained by a change in NFO APBs density driven by different growth surfaces. In N27C26 NFO is grown on the CFO [111] surface, meaning lower APBs density and easier saturation, whereas in C19N21 NFO is grown on ALO, leading to high APBs density and larger saturating fields.

4.5 Room temperature coupling effects

Next, we discuss the magnetization profiles during field reversal at RT. The M-SLDs after field reversal between 0.05 T and 0.2 T in figure 4.7 allows for observation of CFO's and NFO's individual switching behaviour, which can be compared to the single films.

In figure 4.7 in C19N21 (a), NFO's H_c is between 0.1 T and 0.15 T, a percentage increase between 270 % and 450 % when compared to N20's RT H_c. CFO's H_c in C19N21 is between 0.15 T and 0.2 T, a percentage decrease of between 37 % to 16 % when compared to C17's H_c at RT. In N27C26, NFO's H_c is between 0.05 T and 0.1 T, a percentage increase of between 85 % to 270 % when compared to N19's RT H_c, and CFO's H_c is between 0.15 T and 0.2 T, a percentage decrease of between 37 % to 16 % when compared to C17's RT H_c. For rigidly coupled layers, both layers should nucleate at the same field during magnetic hysteresis, discussed in section 1.2.4. As CFO and NFO present different coercive fields in both bilayers, they cannot be rigidly coupled. Some examples where the magnetisations of CFO and NFO are not colinear can be seen in the M-SLDs of C19N21 (a) at B=0.1 T and N27C26 (b) at B=0.15 T.

Figure 4.7 shows in C19N21 (a) a maximum 212 Å ± 3 Å region of magnetic gradient throughout the NFO layer during the bilayers magnetic switching, the same length of increasing magnetisation toward the CFO layer observed at 1.5 T. Interestingly, N27C26 (b) in the range B=0.05 T to B=0.2 T now also presents a 145 Å ± 3 Å region of a magnetic gradient starting at the CFO/NFO interface and leading into NFO. This magnetic gradient, along with a none co-linear magnetisation between CFO and NFO, is an indication of an exchange spring interaction, discussed in section 1.2.4.

The presence of a magnetic gradient in both samples means there is potential in-plane moment canting away from the applied field at the CFO/NFO interface, which can have

several important effects on the measured reflectivity. The in-plane moment canting caused by an exchange spring interaction is linked to magnetisation reversal. During magnetisation reversal, a sample's magnetisation can break down from a single-domain state to a multi-domain state. Here the exchange spring interaction would take place at each coupled domain in NFO and CFO.

If during magnetisation reversal, the sample remained as a single domain or presented large enough domains such that they can be illuminated by the neutron coherently in the sample plane, and moment rotation was in-plane making some angle γ with the applied field direction, this would lead to a mixture of NSF and SF reflectivity profiles. as discussed in section 2.2.5. Without an analyser, the combined SF and NSF channels are measured. The addition of the SF scattering leads to a reduction in spin-asymmetry between the NSF channels. The full magnetisation is present in the combined NSF and SF reflectivity, but without knowing contributions from the SF, the determination of the magnetisation is more difficult. The reduced spin-asymmetry can therefore appear as a reduced magnetisation, though this is not the case physically.

During magnetisation reversal the domains could be small such they were within the neutron coherence length in the sample plane, typically between $600\,\text{nm} < \xi < 60\,\mu\text{m}$, as discussed in section 2.2.5. Specular reflectivity averages over the coherence length incoherently. This means multiple small domains orientated around the applied field direction are averaged, which can lead to a reduction in the observed magnetisation and spin-asymmetry.

This means in specular conditions without spin analysis, if during magnetisation reversal the sample breaks down into large domains or small domains where there is canting away from the applied field, both will have similar effects on the spin-asymmetry and so are difficult to distinguish.

To investigate if an exchange spring interaction was present, R^{++}, R^{+-}, R^{-+} and R^{--} neutron reflectivity profiles were recorded on N27C26 at RT with an applied field of $B = 1.5\,T$ and $B = 0.1\,T$ after field reversal. $B = 0.1\,T$ was assumed to be above the exchange field, allowing the exchange spring coupling to present in NFO, discussed in section 1.2.4. After accounting for spin-flipper efficiency, no indication of neutron SF was detected. We also performed full SF analysis on a similar NFO ($178\,\text{Å} \pm 4\,\text{Å}$)/ CFO ($282\,\text{Å} \pm 8\,\text{Å}$) heterostructure grown on ALO[001] at both RT and 5 K and again saw no SF signal. The amount of SF scattering is dependent on both γ and $\mathbf{Q}_z$. No SF scattering could mean either large domains with a small γ, small domains where the average γ is small, or the SF intensity was too weak to detect.

If the domains are small such that they present a potential step within the neutron coherence length, this can cause off-specular SF scattering, discussed in section 2.2.5. No off-specular or SF off-scattering was observed. As off-specular scattering is weak [130], it's possible it was present but was below the sensitivity limit of the experiment. It's

also possible that the domains are much smaller than the coherence length, leading to off-specular scatting that is too broad and weak to detect.

It is also possible that the magnetisation reversal depends on mechanisms in which moments rotate out-of-plane (OOP). As PNR is only sensitive to in-plane magnetisation, discussed in section 2.2.3, OOP moment rotation would show a decrease in the M-SLD profile. OOP M vs H measurements on C17 and N20 in Chapter 3 showed in-plane and OOP anisotropies without a clear easy direction. This demonstrates that there is some competition with shape anisotropy, meaning an out-of-plane rotation is possible.

4.6 5 K coupling effects

VSM on the bilayers at 5 K, showed an increase in coercive field, the same as the single films in Capter 3. At RT the bilayers presented almost matching H_c values, but at 5 K there is a difference in H_c of 0.088 T. Additionally, at 5 K, both bilayers present two-step hysteresis, loops indicating they are not rigidly coupled. Here we discuss the magnetization profiles during field reversal at 5 K measured with PNR to observe the individual layer switching and potentially explain some of the differences observed with VSM.

The 5 K M-SLD profiles in figure 4.8 show for C19N21 at B=0.75 T and (b) N27C26 at B=0.4 T non-colinear regions between CFO and NFO, connected by an inhomogeneous magnetic gradient in NFO, which is characteristic of an exchange spring interaction, discussed in section 1.2.4. This confirms that the layers are not rigidly coupled, as indicated by the VSM.

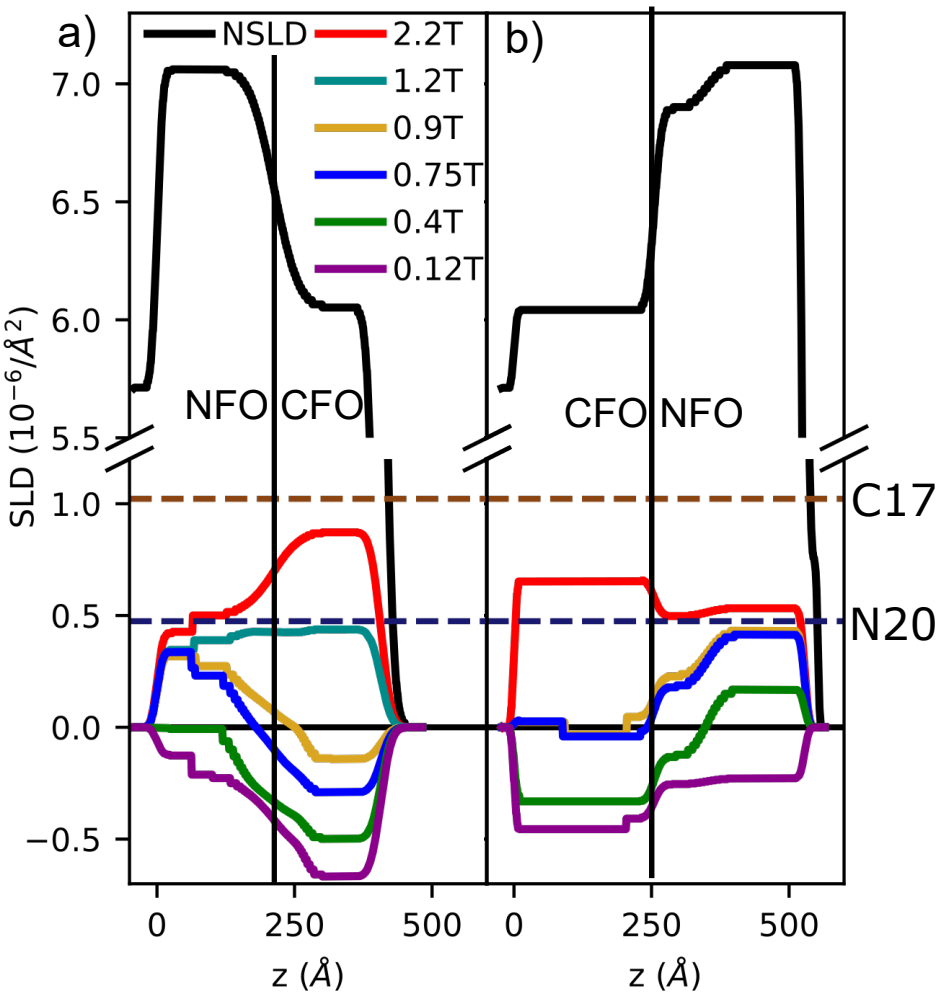

Figure 4.8: Modelled SLD profiles (black) and M-SLD profiles (coloured lines) after field reversal at 3 T for C19N21 (a) and N27C26 (b), measured at 5K. Dashed lines show converted μ_B/F.U. to M-SLD values for VSM of C17 and N20 at 2.2 T and 5 K.

The switching field of NFO in each bilayer can be seen in the M-SLDs shown in figure 4.8. In C19N21 (a) NFO's H_c is between 0.4 T and 0.75 T. When compared to the uncoupled N20 film, which presents a H_c at 5 K of 0.098 T ± 0.001 T, NFO in this bilayer shows a percentage increase in H_c of between 308 % and 665 %. In N27C26 (b), NFOs H_c is between 0.12 T and 0.4 T, a percentage increase between 22 % and 308 % compared to N20 at 5 K. This shows NFO in C19N21 shows a larger increase in H_c when compared to N27C26, the same effect observed at RT. From the PNR at RT, NFO's H_c in C19N21 increased between 270 % to 450 % and in N27C26, increased between 85 % to 270 % when compared to N20's RT H_c.

The differences in NFO H_c between the single film N20 and between the bilayers, can be explained by the behaviour of the soft layer in an exchange spring system. In these systems, the soft layer is pinned to the hard layer below a critical applied field known as the exchange field, H_{ex}, discussed in section 1.2.4. This field is the H_c of NFO which we

observe in the bilayers, given by,

$$H_{ex} = \frac{\pi^2 A_s}{2 M_s t_s^2}, \tag{4.1}$$

where s denotes the soft layer, and A, M and t are the exchange constant, magnetisation and thickness. This $1/t^2$ dependence is likely why N27C26, with a thicker NFO layer, shows a lower NFO switching field when compared to C19N21.

The switching field of CFO in each bilayer can be seen in the M-SLDs shown in figure 4.8. For C19N21 (a), CFO's H_c is between 0.9 T and 1.2 T. When compared to the uncoupled C17, which presents a H_c at 5 K of 1.342 ± 0.008, this shows a 33 % to 11 % decrease. For N27C26 (b), CFO's H_c is between 0.75 T and 0.9 T, a percentage decrease between 44 % to 33 % when compared to C17 at 5 K. A decrease in CFO's H_c is expected in an exchange spring system, discussed in section 1.2.4. The difference in CFO's H_c between the bilayers could be due to multiple effects that are difficult to separate. A difference in strain anisotropy is unlikely to be altering CFO's behaviour between the films as CFO in N27C26 shows a lattice strain of -0.210 % and C19N21 shows an average lattice strain of -0.094 %, meaning both films are weakly strained. The difference in soft layer thickness between the films could drive a change in CFO switching behaviour. As discussed in section 1.2.4, the switching behaviour of the hard layer is dependent on the thickness of the soft layer, t_s, on the order of magnitude of two hard layer domain walls, $2\delta_h$. Ferrite hard/soft heterostructures using CFO as the hard layer have reported exchange spring behaviour, with a critical soft layer thickness of 80 Å [21]. In an exchange spring system, the critical soft layer thickness, δ_{cs}, for rigid coupling is twice the width of the hard layer domain wall, discussed in section 1.2.4, meaning $\delta_{cs} = 2\delta_h \approx 80$ Å. This gives an estimated δ_h of thin film CFO of 40 Å. The difference in NFO thickness between C19N21 and N27C26 is 60 Å, meaning this difference in t_s is of the order of magnitude of the hard layer domain wall length. This can explain the lower switching field for CFO in N27C26 compared to C19N21. As CFO in N27C26 is growing on ALO [001], the same as C17 and C49, it's possible that the film is presenting the same loop-narrowing effects seen in Chapter 3, lowering its H_c when compared to CFO in C19N21. This interestingly would support the argument that the loop narrowing is an interface effect from the ALO substrate.

In figure 4.8 during magnetisation reversal, both bilayers present an M-SLD gradient into the NFO layer. The region of magnetic gradient in the NFO layer in C19N21 is $212 \text{ Å} \pm 3$Å compared to $145 \text{ Å} \pm 3$Å in N27C26, showing a clear difference between the bilayers. It's possible that this gradient is an effect of the structural roughness, however in C19N21 the gradient extends beyond the structural roughness. This effect could be related to the exchange spring coupling. In this coupling, NFO is expected to behave like a Bloch wall after exceeding the exchange field [51]. The length of this region was

discussed in section 1.2.4, described as the critical soft layer domain wall length, given by,

$$\delta_{cs} = \pi\sqrt{\frac{A_s}{2K_h}} \tag{4.2}$$

where K_h is the anisotropy constant of the hard layer. The shorter magnetic gradient region or wall length in N27C26 when compared to C19N21, assuming a constant A_s, implies that CFO has a higher anisotropy constant in N27C26. This is unexpected as CFO in N27C26 has a lower H_c than in C19N21, which would imply a generally weaker anisotropy for CFO. As discussed, this lower CFO H_c in N27C26 could be due to a thicker NFO layer when compared to C19N21. In Chapter 3 it was observed that from C17 to C49, CFO appeared to develop its magnetocrystalline anisotropy, leading to an easier in-plane direction and crucially lower H_c due to a loop narrowing effect. These results could indicate the same relationship, as CFO in N27C26 is 61 Å thicker than CFO in C19N21. The more developed anisotropy in CFO in N27C26 would then contribute to both a lower H_c and decreased δ_{cs}.

4.7 5 K magnetisation effects

Magnetometry on single film C17 and N20 in chapter 3 showed an increase in M_s from RT to 5 K. VSM on both bilayers at 5 K showed an increased M_s when compared to RT measurements. To observe this effect in each layer in the bilayers, allowing for comparison to the single films, we performed PNR at 5 K and 2.2 T, with modelled N and M-SLD profiles presented in figure 4.8.

The VSM measured at 5 K from figure 4.4 shows that 2.2 T was not a saturating field for these samples. To estimate how far away the samples are from saturation, we have calculated the virgin hysteresis loops for the bilayers. To do this we took the magnetisation values at 2.2 T from the top and bottom branches of the hysteresis loop and averaged them. The error is taken as the difference between the calculated virgin loop and the magnetisation values from the top and bottom branches. With the virgin loop, we can estimate how far away the bilayer's magnetisation is from M_s at 2.2 T. For N27C26, this gives 85 % ± 6 % of saturation and for C19N21 88 % ± 2 %.

In C19N21 (a) at 2.2 T, starting at the substrate, the first 63 Å magnetic region in NFO has an M-SLD of $0.427\,10^{-6}/Å^2$. The following 78 Å region in NFO is flat with an M-SLD of $0.500\,^{-6}/Å^2$ and the next 70 Å region leads into the roughness profile towards the NFO/CFO interface, with a maximum M-SLD of $0.538\,10^{-6}/Å^2$. This shows that NFO is presenting an increasing magnetisation beyond the chemical roughness, towards the NFO/CFO interface, the same effect seen at RT.

In N27C26 at 2.2 T, after structural roughness, NFO presents a uniform region of M-SLD of $0.533\,10^{-6}/Å^2$. The M-SLD values of NFO in N27C26 when compared to the

three magnetic regions in C19N21 show percentage differences of, -11 % for the initial region, -6 % for the flat region and 1 % for the final region. This shows that, like at RT, NFO in C19N21 presents the lowest magnetisation, though the difference between the two bilayers is now smaller. Interestingly, it can be seen in figure 4.8, that NFO in both films now presents a similar M-SLD value to N20's magnetisation at 5 K of $0.475\,10^{-6}/\text{Å}^2$, which was not the case at RT. This could be caused by measuring at 2.2 T at 5 K compared to 1.5 T at RT, which is saturating more of the NFO film.

In both C19N21 (a) and N27C26 (b) at 2.2 T, CFO presents a flat M-SLD profile after the structural roughness, with average values of $0.872\,10^{-6}/\text{Å}^2$ and $0.653\,10^{-6}/\text{Å}^2$, respectively. This is surprising, as at RT CFO's magnetisation between the two films showed an 8 % difference, but now this difference is 34 %. One explanation is that the CFO is not saturated, due to measuring below a saturating field. C17 at 5 K presents a magnetic saturation value of $1.022\,10^{-6}/\text{Å}^2$, which is higher than both values of CFO M-SLD from the bilayers at 5 K, supporting the argument that CFO is not saturated in the bilayers. C19N21 was estimated to be 88 % ± 2 % saturated, which can explain the 15 % difference in M-SLD compared to C17. N27C28 was estimated to be 85 % ± 6 % saturated, as such the 36 % decrease in CFO magnetisation compared to C17 is surprising from CFO. One possibility could be that CFO's magnetisation reversal takes place OOP in N27C26. An OOP rotation, combined with large or small domains during magnetisation reversal, would further reduce the magnetisation projection measured by PNR when compared to a reduction from the effects of just domains. From Chapter 3, it was observed that CFO grown on ALO presents a narrowing of its hysteresis loop. One possibility for this loop narrowing was CFO's moments rotating into an OOP easier direction during magnetisation reversal. This same effect could be happening in CFO in N27C26 as it is also grown on an ALO [001] surface. The larger C17 magnetisation could then be explained as this was measured with VSM, which measures the total sample moment, whereas PNR measures the projection of the magnetisation along the applied field direction. Interestingly, this suggests that CFO in C19N21 is rotating more IP, as it has a higher magnetisation compared to CFO in N27C26, more evidence that CFO between the bilayers presents a difference in anisotropy.

Integration of M-SLDs at 5 K and 2.2 T of C19N21 and N27C26 gives values of 1.73 μ_B/F.U. and 1.57 μ_B/F.U. respectively. This appears to show at 5 K that N27C26 has a lower magnetisation than C19N21, disagreeing with the VSM measurement. This could be more evidence that there is an OOP rotation of moments in N27C26, lowering the magnetisation projection observed by PNR.

.

4.8 Summary

By combining thin films of CFO and NFO into heterostructures we have modified the magnetic properties of the individual films. Bilayer samples C19N21 and N27C26 have been grown on ALO [001] via PLD. XRD showed that all bilayer samples are [111] orientated and are weakly compressively strained in the z-axis.

PNR and VSM have been used to characterise the samples' magnetic properties. CFO and NFO showed altered coercive fields in the bilayers when compared to single film samples, showing the layers are magnetically coupled. In both bilayers at RT and 5 K, a magnetic gradient has been observed in the NFO layer during magnetic switching and non-colinear alignment between CFO and NFO was observed. This showed that the bilayers are exchange coupled and present an exchange spring interaction during magnetisation reversal.

Measurements taken during magnetisation reversal revealed no SF scattering and no off-specular SF scattering. As the effects of large domains with combined NSF and SF scattering, small domains averaged over the neutron coherence length, and OOP rotation all reduced the spin-asymmetry, it was not possible to observe any in-plane canting from a potential exchange spring interaction.

Different NFO coercivities were observed between N27C26 and C19N21 which can be explained by the $1/t_s^2$ dependence on H_{ex} in exchange spring systems. Differences in CFO switching behaviour were observed between the bilayers which are due to several potential effects. It's possible that the change in length of the soft layer (NFO) has altered the switching behaviour due to the exchange coupling. It's also possible that CFO in N27C26 presents the same loop narrowing discussed for CFO in Chapter 3, lowering its H_c when compared to CFO in C19N21.

The length of increasing magnetisation in C19N21 in NFO was was $212\,\text{Å} \pm 3\text{Å}$ compared to $145\,\text{Å} \pm 3\text{Å}$ in N27C26. This region was compared to the length of δ_{cs} in an exchange spring system, which is proportional to $1/\sqrt{2K_h}$, evidence that CFO has a larger anisotropy energy constant in N27C26 compared to C19N21.

NFO in both bilayers at RT and 5 K shows a lower M_s than bulk NFO. This can be explained by the presence of APBs in NFO in both films, leading to very large saturating fields. The larger NFO M_s in N27C27, when compared to C19N21, indicates that when grown on ALO, NFO is presenting more APBs compared to being grown on CFO. This difference in APBs density leads to a larger bilayer M_s in N27C26 when compared to C19N21. CFO showed a smaller change in magnetisation between the bilayers at RT, and showed a similar M_s to C17, indicating that the lower magnetisation is not due only to the effects of APBs, but some other mechanism such as cation inversion. This showed that APBs play a larger role in NFO's magnetisation than CFO, which is surprising given the similar crystal structure and lattice constants of the materials. A lower M-SLD in

CFO at 5 K in N27C26 when compared to C17 and C19N21 was evidence that CFO's magnetisation rotates OOP during magnetisation reversal.

This chapter clearly demonstrates that by growing NFO and CFO bilayers on ALO[001], the film's individual magnetic properties are modified due to the effects of layer anisotropies, layer thicknesses, growth surfaces and exchange spring coupling.

Chapter 5

Conclusions and future outlook

5.1 Conclusions

The goal of this thesis was to investigate the structural and magnetic properties of thin film CFO and NFO grown as single layers and in magnetic heterostructures on ALO. We chose to investigate ferrites as they are a versatile group of materials which have attracted large attention in recent years due to a broad range of magnetic and electronic properties. CFO was selected due to its low conductivity, large magnetostriction and high magneto-crystalline anisotropy constant when compared to other ferrites. NFO was selected due to its large exchange splitting, ability to be grown insulating or conducting and its soft ferrimagnetic behaviour.

Ferrite thin films have been shown to have modified structural and magnetic properties due to interactions with the substrate, for example, via strain. As such we selected ALO [001] as a substrate due to an 8% mismatch on the O-O sublattice with the [111] plane in NFO and CFO, leading to tensile strain.

The similar crystal structures of CFO and NFO meant the materials were highly suitable for combination into a heterostructure. The relative hard/soft magnetisations of CFO and NFO made them interesting candidates for studying the physics of exchange coupling and exchange spring interactions.

PNR was employed, in combination with XRR, to probe the nuclear and magnetic profiles of samples as a function of depth. This was particularly useful in the investigation of the magnetic bilayers as it was possible to observe in individual magnetisation of each film. VSM and AD-VSM were employed to observe the films' magnetic moments and hysteresis over a range of temperatures and applied field directions. XRD has been used to characterise the films' crystal structure, with the use of both the Scherrer equation and Laue oscillation function allowing for observation of the number of coherent unit cells in each film. The combination of these techniques has allowed for a broad characterisation of samples' magnetic and structural properties.

Experiments on single film CFO and NFO samples C17, C49, N20 and N45 have revealed the modified magnetic and structural properties which are related to the layer thickness and ALO [001] growth surface. All films show a [111] orientation grown on the ALO [001] surface. All films showed a lower strain than the expected 8 % from ALO. C17, C49 and N20 showed a compressive strain in the z-axis, and interestingly N45 showed no strain in the z-axis. In combination with bulk N-SLD values, this indicated that the unit cell volume has remained the same in all samples and that misfit dislocations may have occurred during growth. Simulation of Laue oscillations when compared to layer thicknesses from PNR show C17, C49, and N20 are one coherent crystalline phase OOP, showing high-quality growth. The lack of compressive strain observed in N45 could be due to an initial growth phase which allowed for strain relaxation over a shorter length when compared to the CFO films.

APBs near the ALO interface could be playing a large role in the behaviour of the NFO films. PNR revealed regions of reduced N and M-SLD in both N20 and N45 at the interface with ALO, which can be explained by large amounts of crystal defects. VSM measurements on N20 showed large saturating fields for the ferromagnetic response at RT and 5 K, well above the bulk saturating field, which was more evidence of APBs. Both CFO films presented lower than bulk magnetisation, also indicating the effects of APBs. However, the uniform N and M-SLDs profiles and VSM measurements which saturated, indicated a weaker effect of APBs when compared to NFO. This indicated that the ALO interface causes more APB defects in NFO than in CFO. Interestingly, C49 showed a narrowing of its hysteresis loop in-plane. This narrowing was present out of the sample plane in C17. This effect could be related to both stress anisotropy and film thickness. C17 and N20 films showed weak anisotropy between the in-plane directions and out-of-plane directions. The thicker C49 and N45 films then showed clear IP easier directions, indicating the films were increasing their magneto-crystalline or shape anisotropy with increasing thickness.

Experiments of bilayers of CFO and NFO on samples C19N21 and N27C26 have shown modified magnetic properties when compared to the single films linked to layer order reversal, layer thickness and exchange coupling. XRD revealed all samples are [111] orientated. The values of strain in strain in both samples were lower than the single films, suggesting the growth of the second layer has modified the observed strain of the bottom layer. A combination of VSM and PNR results showed that the bilayers are exchange-coupled. None co-linear M-SLD profiles of both bilayers at RT and 5 K during magnetisation reversal demonstrated that this exchange coupling is not rigid. Regions of increasing magnetisation into the NFO layers M-SLD during magnetisation reversal was evidence that the layers were presenting an exchange spring interaction. The physics of exchange coupled systems are then used to explain differences in the switching behaviour of NFO and CFO between the systems, highlighting these systems'

sensitivity to soft layer thickness. Interestingly, a difference in the length of the exchange spring between the bilayers indicated a difference in the anisotropy energy of the CFO between the bilayers, potentially showing a strong effect from the ALO surface or from a small relative change in thickness. Measurements of PNR at 2.2 T at 5 K on N27C26 showed a reduced CFO magnetisation when compared to C19N21. This was evidence that CFO moments were making an OOP rotation during magnetisation reversal, another indication that the anisotropy of CFO in N27C26 was different than C19N21. Differences in NFO magnetisation driven by layer order reversal were evidence that the APBs density is linked to the growth surface. The opposite was true for CFO, where a small change in magnetisation density driven by layer order reversal was more evidence that CFO was presenting a lower APB density.

5.2 Outlook and future work

Going forward with these results, some measurements could be used to answer key questions. We plan to perform transmission-electron-microscopy (TEM) in combination with electron energy loss spectroscopy (EELS). The images from TEM will allow for observation of local defect density and give more insight into the film thickness. EELS will allow for observation of local Fe, Co, Ni, O and Al content in the films. The combination of TEM and EELS will help answer questions about chemical diffusion in the film, questions about APBs defects and APB defect density.

Additional XRD will be performed. The XRD measurement on C49 in Chapter 3 will be retaken with a monochromatic optic, potentially allowing for observation of Laue oscillations. Full reciprocal space maps will be performed on all films. This will give insight into both the in-plane strain and will allow for the determination of whether the films are epitaxial or present in plane texture effects. Due to the thickness dependant properties of both the thin film and bilayers, we have begun a new investigation into the effects of lowering the bottom layer thickness of NFO/CFO bilayers, shown in Appendix A.

Bibliography

[1] A. V. Ramos, M.-J. Guittet, J.-B. Moussy, R. Mattana, C. Deranlot, F. Petroff, and C. Gatel. Room temperature spin filtering in epitaxial cobalt-ferrite tunnel barriers. *Applied Physics Letters*, 91(12):122107, 2007. doi: 10.1063/1.2787880. URL https://doi.org/10.1063/1.2787880.

[2] S. Matzen, J.-B. Moussy, P. Wei, C. Gatel, J. C. Cezar, M. A. Arrio, Ph. Sainctavit, and J. S. Moodera. Structure, magnetic ordering, and spin filtering efficiency of $NiFe_2O_4$(111) ultrathin films. *Applied Physics Letters*, 104(18):182404, 2014. doi: 10.1063/1.4871733. URL https://doi.org/10.1063/1.4871733.

[3] Er-Jia Guo, Andreas Herklotz, Andreas Kehlberger, Joel Cramer, Gerhard Jakob, and Mathias Kläui. Thermal generation of spin current in epitaxial $CoFe_2O_4$ thin films. *Applied Physics Letters*, 108(2):022403, 2016. doi: 10.1063/1.4939625. URL https://doi.org/10.1063/1.4939625.

[4] Zhong Li, Jan Krieft, Amit Vikram Singh, Sudhir Regmi, Ankur Rastogi, Abhishek Srivastava, Zbigniew Galazka, Tim Mewes, Arunava Gupta, and Timo Kuschel. Vectorial observation of the spin seebeck effect in epitaxial $NiFe_2O_4$ thin films with various magnetic anisotropy contributions. *Applied Physics Letters*, 114 (23):232404, 2019. doi: 10.1063/1.5092774. URL https://doi.org/10.1063/1.5092774.

[5] D. Meier, T. Kuschel, L. Shen, A. Gupta, T. Kikkawa, K. Uchida, E. Saitoh, J.-M. Schmalhorst, and G. Reiss. Thermally driven spin and charge currents in thin $NiFe_2O_4$/Pt films. *Phys. Rev. B*, 87:054421, Feb 2013. doi: 10.1103/PhysRevB.87.054421. URL https://link.aps.org/doi/10.1103/PhysRevB.87.054421.

[6] Ana V. Ramos, Sylvia Matzen, Jean-Baptiste Moussy, Frédéric Ott, and Michel Viret. Artificial antiphase boundary at the interface of ferrimagnetic spinel bilayers. *Phys. Rev. B*, 79:014401, Jan 2009. doi: 10.1103/PhysRevB.79.014401. URL https://link.aps.org/doi/10.1103/PhysRevB.79.014401.

[7] A. V. Ramos, J.-B. Moussy, M.-J. Guittet, M. Gautier-Soyer, C. Gatel, P. Bayle-Guillemaud, B. Warot-Fonrose, and E. Snoeck. Influence of a metallic or oxide

top layer in epitaxial magnetic bilayers containing $CoFe_2O_4$(111) tunnel barriers. *Phys. Rev. B*, 75:224421, Jun 2007. doi: 10.1103/PhysRevB.75.224421. URL https://link.aps.org/doi/10.1103/PhysRevB.75.224421.

[8] B. B. Nelson-Cheeseman, R. V. Chopdekar, J. S. Bettinger, E. Arenholz, and Y. Suzuki. Magnetism of $NiMn_2O_4$–Fe_3O_4 spinel interfaces. *Journal of Applied Physics*, 103(7):07B524, 2008. doi: 10.1063/1.2838320. URL https://doi.org/10.1063/1.2838320.

[9] U. Lüders, A. Barthélémy, M. Bibes, K. Bouzehouane, S. Fusil, E. Jacquet, J.-P. Contour, J.-F. Bobo, J. Fontcuberta, and A. Fert. $NiFe_2O_4$: A versatile spinel material brings new opportunities for spintronics. *Advanced Materials*, 18(13): 1733–1736, 2006. doi: https://doi.org/10.1002/adma.200500972. URL https://onlinelibrary.wiley.com/doi/abs/10.1002/adma.200500972.

[10] K. Maaz, A. Mumtaz, S.K. Hasanain, and M.F. Bertino. Temperature dependent coercivity and magnetization of nickel ferrite nanoparticles. *Journal of Magnetism and Magnetic Materials*, 322(15):2199–2202, 2010. ISSN 0304-8853. doi: https://doi.org/10.1016/j.jmmm.2010.02.010. URL https://www.sciencedirect.com/science/article/pii/S0304885310000764.

[11] S. Venzke, R.B. Van Dover, J.M. Phillips, E.M. Gyorgy, T. Siegrist, C.-H. Chen, D. Werder, R.M. Fleming, R.J. Felder, E. Coleman, and R. Opila. Epitaxial growth and magnetic behavior of $NiFe_2O_4$ thin films. *Journal of Materials Research*, 11 (5):1187–1198, 1996. ISSN 0884-2914. doi: 10.1557/JMR.1996.0153.

[12] Bernard D. Cullity, Bernard Dennis Cullity, and Chad D. Graham. *Introduction to magnetic materials*. IEEE Press, Piscataway, NJ, 2. ed edition, 2009. ISBN 978-0-471-47741-9.

[13] M. Khodaei, S.A. Seyyed Ebrahimi, Yong Jun Park, Jong Mok Ok, Jun Sung Kim, Junwoo Son, and Sunggi Baik. Strong in-plane magnetic anisotropy in (111)-oriented $CoFe_2O_4$ thin film. *Journal of Magnetism and Magnetic Materials*, 340:16–22, 2013. ISSN 0304-8853. doi: https://doi.org/10.1016/j.jmmm.2013.03.019. URL https://www.sciencedirect.com/science/article/pii/S030488531300187X.

[14] M. Ounacer, A. Essoumhi, M. Sajieddine, A. Razouk, A. Fnidiki, F. Richomme, J. Juraszek, S.M. Dubiel, and M. Sahlaoui. Substitutional effect of Mg^{2+} on structural and magnetic properties of cobalt nanoferrite. *Journal of Physics and Chemistry of Solids*, 148:109687, 2021. ISSN 0022-3697. doi: https://doi.org/10.1016/j.jpcs.2020.109687. URL https://www.sciencedirect.com/science/article/pii/S0022369719325946.

[15] P. Priyadharsini, A. Pradeep, P. Sambasiva Rao, and G. Chandrasekaran. Structural, spectroscopic and magnetic study of nanocrystalline Ni–Zn ferrites. *Materials Chemistry and Physics*, 116(1):207–213, 2009. ISSN 0254-0584. doi: https://doi.org/10.1016/j.matchemphys.2009.03.011. URL https://www.sciencedirect.com/science/article/pii/S0254058409001606.

[16] E.F. Kneller and R. Hawig. The exchange-spring magnet: a new material principle for permanent magnets. *IEEE Transactions on Magnetics*, 27(4):3588–3560, 1991. doi: 10.1109/20.102931.

[17] Ralph Skomski and J. M. D. Coey. Giant energy product in nanostructured two-phase magnets. *Phys. Rev. B*, 48:15812–15816, Dec 1993. doi: 10.1103/PhysRevB.48.15812. URL https://link.aps.org/doi/10.1103/PhysRevB.48.15812.

[18] T. Leineweber and H. Kronmüller. Micromagnetic examination of exchange coupled ferromagnetic nanolayers. *Journal of Magnetism and Magnetic Materials*, 176(2):145–154, 1997. ISSN 0304-8853. doi: https://doi.org/10.1016/S0304-8853(97)00601-X. URL https://www.sciencedirect.com/science/article/pii/S030488539700601X.

[19] Eric E Fullerton, J.S Jiang, and S.D Bader. Hard/soft magnetic heterostructures: model exchange-spring magnets. *Journal of Magnetism and Magnetic Materials*, 200(1):392–404, 1999. ISSN 0304-8853. doi: https://doi.org/10.1016/S0304-8853(99)00376-5. URL https://www.sciencedirect.com/science/article/pii/S0304885399003765.

[20] K. Ruwisch, T. Pohlmann, M. Hoppe, F. Bertram, P. Shafer, J. Wollschläger, and K. Küpper. Inferface magnetization phenomena in epitaxial thin $Fe_3O_4/Co_xFe_{3-x}O_4$ bilayers. *The Journal of Physical Chemistry C*, 125(42):23327–23337, 2021. doi: 10.1021/acs.jpcc.1c05274. URL https://doi.org/10.1021/acs.jpcc.1c05274.

[21] G. Lavorato, E. Winkler, B. Rivas-Murias, and F. Rivadulla. Thickness dependence of exchange coupling in epitaxial $Fe_3O_4/CoFe_2O_4$ soft/hard magnetic bilayers. *Phys. Rev. B*, 94:054405, Aug 2016. doi: 10.1103/PhysRevB.94.054405. URL https://link.aps.org/doi/10.1103/PhysRevB.94.054405.

[22] Keith P. McKenna, Florian Hofer, Daniel Gilks, Vlado K. Lazarov, Chunlin Chen, Zhongchang Wang, and Yuichi Ikuhara. Atomic-scale structure and properties of highly stable antiphase boundary defects in Fe_3O_4. *Nature Communications*, 5 (1):5740, Dec 2014. ISSN 2041-1723. doi: 10.1038/ncomms6740. URL https://doi.org/10.1038/ncomms6740.

[23] W Eerenstein, T.T.M Palstra, and T Hibma. Spin-valve behaviour of anti-ferromagnetic boundaries in ultrathin magnetite films. *Thin Solid Films*, 400(1):90–94, 2001. ISSN 0040-6090. doi: https://doi.org/10.1016/S0040-6090(01)01465-1. URL https://www.sciencedirect.com/science/article/pii/S0040609001014651. Proceedings of Symposium N on Ultrathin Oxides.

[24] W. Eerenstein, T. T. M. Palstra, T. Hibma, and S. Celotto. Diffusive motion of antiphase domain boundaries in Fe_3O_4 films. *Phys. Rev. B*, 68:014428, Jul 2003. doi: 10.1103/PhysRevB.68.014428. URL https://link.aps.org/doi/10.1103/PhysRevB.68.014428.

[25] Susana Gota, Eric Guiot, Michèle Henriot, and Martine Gautier-Soyer. Atomic-oxygen-assisted mbe growth of α-Fe_2O_3 on α-Al_2O_3(0001): Metastable FeO(111)-like phase at subnanometer thicknesses. *Phys. Rev. B*, 60:14387–14395, Nov 1999. doi: 10.1103/PhysRevB.60.14387. URL https://link.aps.org/doi/10.1103/PhysRevB.60.14387.

[26] Ryan Comes, Man Gu, Mikhail Khokhlov, Jiwei Lu, and Stuart A. Wolf. Microstructural and domain effects in epitaxial $CoFe_2O_4$ films on MgO with perpendicular magnetic anisotropy. *Journal of Magnetism and Magnetic Materials*, 324(4):524–527, 2012. ISSN 0304-8853. doi: https://doi.org/10.1016/j.jmmm.2011.08.033. URL https://www.sciencedirect.com/science/article/pii/S0304885311005968.

[27] D. T. Margulies, F. T. Parker, M. L. Rudee, F. E. Spada, J. N. Chapman, P. R. Aitchison, and A. E. Berkowitz. Origin of the anomalous magnetic behavior in single crystal Fe_3O_4 films. *Phys. Rev. Lett.*, 79:5162–5165, Dec 1997. doi: 10.1103/PhysRevLett.79.5162. URL https://link.aps.org/doi/10.1103/PhysRevLett.79.5162.

[28] T. Dhakal, D. Mukherjee, R. Hyde, P. Mukherjee, M. H. Phan, H. Srikanth, and S. Witanachchi. Magnetic anisotropy and field switching in cobalt ferrite thin films deposited by pulsed laser ablation. *Journal of Applied Physics*, 107(5):053914, 2010. doi: 10.1063/1.3327424. URL https://doi.org/10.1063/1.3327424.

[29] J. H. Yin, J. Ding, B. H. Liu, J. B. Yi, X. S. Miao, and J. S. Chen. Magnetic anisotropy and high coercivity of epitaxial Co-ferrite films prepared by pulsed laser deposition. *Journal of Applied Physics*, 101(9):09K509, 2007. doi: 10.1063/1.2709763. URL https://doi.org/10.1063/1.2709763.

[30] S. Blundell. *Magnetism in Condensed Matter*, pages 128–129. Oxford Master Series in Condensed Matter Physics 4. OUP Oxford, 2001. ISBN 9780198505921. URL https://books.google.fr/books?id=Jk5yDwAAQBAJ.

[31] J. M. D. Coey. *Ferromagnetism and exchange*, page 128–194. Cambridge University Press, 2010. doi: 10.1017/CBO9780511845000.006.

[32] R.C. O'Handley. *Modern Magnetic Materials: Principles and Applications*, page 199. Wiley, 1999. ISBN 9780471155669. URL https://books.google.co.uk/books?id=RKV1QgAACAAJ.

[33] Steven H. Simon. *The Oxford solid state basics*. Oxford University Press, Oxford, reprinted (with corrections, twice) edition, 2017. ISBN 978-0-19-968076-4 978-0-19-968077-1.

[34] W. Heisenberg. Mehrkörperproblem und Resonanz in der Quantenmechanik. *Zeitschrift für Physik*, 38(6):411–426, June 1926. ISSN 0044-3328. doi: 10.1007/BF01397160. URL https://doi.org/10.1007/BF01397160.

[35] Paul Adrien Maurice Dirac and Ralph Howard Fowler. On the theory of quantum mechanics. *Proceedings of the Royal Society of London. Series A, Containing Papers of a Mathematical and Physical Character*, 112(762):661–677, 1926. doi: 10.1098/rspa.1926.0133. URL https://royalsocietypublishing.org/doi/abs/10.1098/rspa.1926.0133.

[36] *Introduction to Magnetic Materials*, chapter 4, pages 115–149. John Wiley & Sons, Ltd, 2008. ISBN 9780470386323. doi: https://doi.org/10.1002/9780470386323.ch4. URL https://onlinelibrary.wiley.com/doi/abs/10.1002/9780470386323.ch4.

[37] M. Louis Néel. Propriétés magnétiques des ferrites ; ferrimagnétisme et antiferromagnétisme. *Ann. Phys.*, 12(3):137–198, 1948. doi: 10.1051/anphys/194812030137. URL https://doi.org/10.1051/anphys/194812030137.

[38] J. Bransky and A.A. Hirsch. Magnetic anisotropy in ferromagnetic thin films. *Physica*, 34(3):349–360, 1967. ISSN 0031-8914. doi: https://doi.org/10.1016/0031-8914(67)90002-X. URL https://www.sciencedirect.com/science/article/pii/003189146790002X.

[39] J.P. Joule. XVII. *On the effects of magnetism upon the dimensions of iron and steel bars. The London, Edinburgh, and Dublin Philosophical Magazine and Journal of Science*, 30(199):76–87, February 1847. ISSN 1941-5966, 1941-5974. doi: 10.1080/14786444708645656. URL https://www.tandfonline.com/doi/full/10.1080/14786444708645656.

[40] J. M. D. Coey. *Magnetism and Magnetic Materials*, page 267–274. Cambridge University Press, 2010. doi: 10.1017/CBO9780511845000.006.

[41] *Magnetostriction and the Effects of Stress*, chapter 8, pages 241–273. John Wiley Sons, Ltd, 2008. ISBN 9780470386323. doi: https://doi.org/10.1002/9780470386323.ch8. URL https://onlinelibrary.wiley.com/doi/abs/10.1002/9780470386323.ch8.

[42] R Skomski. Nanomagnetics. *Journal of Physics: Condensed Matter*, 15(20):R841–R896, may 2003. doi: 10.1088/0953-8984/15/20/202. URL https://doi.org/10.1088/0953-8984/15/20/202.

[43] Hans-Benjamin Braun. Topological effects in nanomagnetism: from superparamagnetism to chiral quantum solitons. *Advances in Physics*, 61(1):1–116, 2012. doi: 10.1080/00018732.2012.663070. URL https://doi.org/10.1080/00018732.2012.663070.

[44] Frances Hellman, Axel Hoffmann, Yaroslav Tserkovnyak, Geoffrey S. D. Beach, Eric E. Fullerton, Chris Leighton, Allan H. MacDonald, Daniel C. Ralph, Dario A. Arena, Hermann A. Dürr, Peter Fischer, Julie Grollier, Joseph P. Heremans, Tomas Jungwirth, Alexey V. Kimel, Bert Koopmans, Ilya N. Krivorotov, Steven J. May, Amanda K. Petford-Long, James M. Rondinelli, Nitin Samarth, Ivan K. Schuller, Andrei N. Slavin, Mark D. Stiles, Oleg Tchernyshyov, André Thiaville, and Barry L. Zink. Interface-induced phenomena in magnetism. *Rev. Mod. Phys.*, 89:025006, Jun 2017. doi: 10.1103/RevModPhys.89.025006. URL https://link.aps.org/doi/10.1103/RevModPhys.89.025006.

[45] Hao Zeng, Jing Li, J. P. Liu, Zhong L. Wang, and Shouheng Sun. Exchange-coupled nanocomposite magnets by nanoparticle self-assembly. *Nature*, 420(6914):395–398, November 2002. ISSN 1476-4687. doi: 10.1038/nature01208. URL https://www.nature.com/articles/nature01208.

[46] S. M. Rezende, R. L. Rodríguez-Suárez, and A. Azevedo. Theory of the spin seebeck effect in antiferromagnets. *Phys. Rev. B*, 93:014425, Jan 2016. doi: 10.1103/PhysRevB.93.014425. URL https://link.aps.org/doi/10.1103/PhysRevB.93.014425.

[47] S. A. Wolf, D. D. Awschalom, R. A. Buhrman, J. M. Daughton, S. von Molnár, M. L. Roukes, A. Y. Chtchelkanova, and D. M. Treger. Spintronics: A spin-based electronics vision for the future. *Science*, 294(5546):1488–1495, 2001. doi: 10.1126/science.1065389. URL https://www.science.org/doi/abs/10.1126/science.1065389.

[48] T. Kado. Large room-temperature inverse magnetoresistance in tunnel junctions with a Fe_3O_4 electrode. *Applied Physics Letters*, 92(9):092502, 2008. doi: 10.1063/1.2890852. URL https://doi.org/10.1063/1.2890852.

[49] Jean-Baptiste Moussy. From epitaxial growth of ferrite thin films to spin-polarized tunnelling. *Journal of Physics D: Applied Physics*, 46(14):143001, mar 2013. doi: 10.1088/0022-3727/46/14/143001. URL https://doi.org/10.1088/0022-3727/46/14/143001.

[50] L. Marnitz, K. Rott, S. Niehörster, C. Klewe, D. Meier, S. Fabretti, M. Witziok, A. Krampf, O. Kuschel, T. Schemme, K. Kuepper, J. Wollschläger, A. Thomas, G. Reiss, and T. Kuschel. Sign change in the tunnel magnetoresistance of Fe_3O_4/MgO/Co-Fe-B magnetic tunnel junctions depending on the annealing temperature and the interface treatment. *AIP Advances*, 5(4):047103, 2015. doi: 10.1063/1.4917018. URL https://doi.org/10.1063/1.4917018.

[51] Eiichi Goto, Nobuo Hayashi, Takaaki Miyashita, and Keisuke Nakagawa. Magnetization and switching characteristics of composite thin magnetic films. *Journal of Applied Physics*, 36(9):2951–2958, 1965. doi: 10.1063/1.1714613. URL https://doi.org/10.1063/1.1714613.

[52] T. Leineweber and H. Kronmüller. Micromagnetic examination of exchange coupled ferromagnetic nanolayers. *Journal of Magnetism and Magnetic Materials*, 176(2):145–154, December 1997. ISSN 0304-8853. doi: 10.1016/S0304-8853(97)00601-X. URL https://www.sciencedirect.com/science/article/pii/S030488539700601X.

[53] R. F. Sabiryanov and S. S. Jaswal. Magnetic properties of hard/soft composites: $SmCo_5Co_{1-x}Fe_x$. *Phys. Rev. B*, 58:12071–12074, Nov 1998. doi: 10.1103/PhysRevB.58.12071. URL https://link.aps.org/doi/10.1103/PhysRevB.58.12071.

[54] Eric E. Fullerton, J. S. Jiang, M. Grimsditch, C. H. Sowers, and S. D. Bader. Exchange-spring behavior in epitaxial hard/soft magnetic bilayers. *Phys. Rev. B*, 58:12193–12200, Nov 1998. doi: 10.1103/PhysRevB.58.12193. URL https://link.aps.org/doi/10.1103/PhysRevB.58.12193.

[55] J. S. Jiang, Eric E. Fullerton, M. Grimsditch, C. H. Sowers, and S. D. Bader. Exchange-spring behavior in epitaxial hard/soft magnetic bilayer films. *Journal of Applied Physics*, 83(11):6238–6240, 1998. doi: 10.1063/1.367769. URL https://doi.org/10.1063/1.367769.

[56] W. H. Meiklejohn and C. P. Bean. New magnetic anisotropy. *Phys. Rev.*, 105: 904–913, Feb 1957. doi: 10.1103/PhysRev.105.904. URL https://link.aps.org/doi/10.1103/PhysRev.105.904.

[57] W. H. Meiklejohn and C. P. Bean. New magnetic anisotropy. *Phys. Rev.*, 102: 1413–1414, Jun 1956. doi: 10.1103/PhysRev.102.1413. URL https://link.aps.org/doi/10.1103/PhysRev.102.1413.

[58] A.E. Berkowitz and Kentaro Takano. Exchange anisotropy — a review. *Journal of Magnetism and Magnetic Materials*, 200(1):552–570, 1999. ISSN 0304-8853. doi: https://doi.org/10.1016/S0304-8853(99)00453-9. URL https://www.sciencedirect.com/science/article/pii/S0304885399004539.

[59] J Nogués and Ivan K Schuller. Exchange bias. *Journal of Magnetism and Magnetic Materials*, 192(2):203–232, 1999. ISSN 0304-8853. doi: https://doi.org/10.1016/S0304-8853(98)00266-2. URL https://www.sciencedirect.com/science/article/pii/S0304885398002662.

[60] K. O'Grady, L.E. Fernandez-Outon, and G. Vallejo-Fernandez. A new paradigm for exchange bias in polycrystalline thin films. *Journal of Magnetism and Magnetic Materials*, 322(8):883–899, 2010. ISSN 0304-8853. doi: https://doi.org/10.1016/j.jmmm.2009.12.011. URL https://www.sciencedirect.com/science/article/pii/S0304885309011561.

[61] S. S. P. Parkin, K. P. Roche, M. G. Samant, P. M. Rice, R. B. Beyers, R. E. Scheuerlein, E. J. O'Sullivan, S. L. Brown, J. Bucchigano, D. W. Abraham, Yu Lu, M. Rooks, P. L. Trouilloud, R. A. Wanner, and W. J. Gallagher. Exchange-biased magnetic tunnel junctions and application to nonvolatile magnetic random access memory (invited). *Journal of Applied Physics*, 85(8):5828–5833, 1999. doi: 10.1063/1.369932. URL https://doi.org/10.1063/1.369932.

[62] Ratnesh Gupta, K. Sangeeth, M. Gupta, R. J. Choudhary, A. Sagdeo, F. Singh, and Ajay Gupta. Magnetic properties of exchange-biased FeCo/CoO bilayer and its electronic structure. *Applied Physics A*, 128(4):342, March 2022. ISSN 1432-0630. doi: 10.1007/s00339-022-05464-6. URL https://doi.org/10.1007/s00339-022-05464-6.

[63] D J Adams, D Cimpoesu, S Benit, D Maurin, P R Kern, M Carara, and L Spinu. Critical curves in NiFe/FeMn bilayers with varying antiferromagnetic layer thickness. *Journal of Physics D: Applied Physics*, 55(6):065002, nov 2021. doi: 10.1088/1361-6463/ac30bb. URL https://doi.org/10.1088/1361-6463/ac30bb.

[64] Ali C. Basaran, T. Saerbeck, J. de la Venta, H. Huckfeldt, A. Ehresmann, and Ivan K. Schuller. Exchange bias: The antiferromagnetic bulk matters. *Applied Physics Letters*, 105(7):072403, 2014. doi: 10.1063/1.4893457. URL https://doi.org/10.1063/1.4893457.

[65] T. Qian, G. Li, T. Zhang, T. F. Zhou, X. Q. Xiang, X. W. Kang, and X. G. Li. Exchange bias tuned by cooling field in phase separated $Y_{0.2}Ca_{0.8}MnO_3$. *Applied Physics Letters*, 90(1):012503, 2007. doi: 10.1063/1.2426887. URL https://doi.org/10.1063/1.2426887.

[66] De-Hua Han, Jian-Gang Zhu, and Jack H. Judy. NiFe/NiO bilayers with high exchange coupling and low coercive fields. *Journal of Applied Physics*, 81(8):4996–4998, 1997. doi: 10.1063/1.364964. URL https://doi.org/10.1063/1.364964.

[67] R. F. L. Evans, D. Bate, R. W. Chantrell, R. Yanes, and O. Chubykalo-Fesenko. Influence of interfacial roughness on exchange bias in core-shell nanoparticles. *Phys. Rev. B*, 84:092404, Sep 2011. doi: 10.1103/PhysRevB.84.092404. URL https://link.aps.org/doi/10.1103/PhysRevB.84.092404.

[68] T. Thomson. 10 - magnetic properties of metallic thin films. In Katayun Barmak and Kevin Coffey, editors, *Metallic Films for Electronic, Optical and Magnetic Applications*, pages 454–546. Woodhead Publishing, 2014. ISBN 978-0-85709-057-7. doi: https://doi.org/10.1533/9780857096296.2.454. URL https://www.sciencedirect.com/science/article/pii/B9780857090577500103.

[69] Òscar Iglesias, Amílcar Labarta, and Xavier Batlle. Exchange Bias Phenomenology and Models of Core/Shell Nanoparticles. *Journal of Nanoscience and Nanotechnology*, 8(6):2761–2780, June 2008. doi: 10.1166/jnn.2008.18306.

[70] J. Nogués, J. Sort, V. Langlais, V. Skumryev, S. Suriñach, J.S. Muñoz, and M.D. Baró. Exchange bias in nanostructures. *Physics Reports*, 422(3):65–117, 2005. ISSN 0370-1573. doi: https://doi.org/10.1016/j.physrep.2005.08.004. URL https://www.sciencedirect.com/science/article/pii/S0370157305003303.

[71] R L Stamps. Mechanisms for exchange bias. *Journal of Physics D: Applied Physics*, 33(23):R247–R268, nov 2000. doi: 10.1088/0022-3727/33/23/201. URL https://doi.org/10.1088/0022-3727/33/23/201.

[72] Miguel Kiwi. Exchange bias theory. *Journal of Magnetism and Magnetic Materials*, 234(3):584–595, 2001. ISSN 0304-8853. doi: https://doi.org/10.1016/S0304-8853(01)00421-8. URL https://www.sciencedirect.com/science/article/pii/S0304885301004218.

[73] T. C. Schulthess and W. H. Butler. Consequences of spin-flop coupling in exchange biased films. *Phys. Rev. Lett.*, 81:4516–4519, Nov 1998. doi: 10.1103/PhysRevLett.81.4516. URL https://link.aps.org/doi/10.1103/PhysRevLett.81.4516.

[74] Miroslavna Kovylina, Montserrat García del Muro, Zorica Konstantinović, Manuel Varela, Òscar Iglesias, Amílcar Labarta, and Xavier Batlle. Controlling exchange bias in Co-CoO_x nanoparticles by oxygen content. *Nanotechnology*, 20(17):175702, apr 2009. doi: 10.1088/0957-4484/20/17/175702. URL https://doi.org/10.1088/0957-4484/20/17/175702.

[75] D. Lederman, J. Nogués, and Ivan K. Schuller. Exchange anisotropy and the antiferromagnetic surface order parameter. *Phys. Rev. B*, 56:2332–2335, Aug 1997. doi: 10.1103/PhysRevB.56.2332. URL https://link.aps.org/doi/10.1103/PhysRevB.56.2332.

[76] A. V. Ramos, T. S. Santos, G. X. Miao, M.-J. Guittet, J.-B. Moussy, and J. S. Moodera. Influence of oxidation on the spin-filtering properties of $CoFe_2O_4$ and the resultant spin polarization. *Phys. Rev. B*, 78:180402, Nov 2008. doi: 10.1103/PhysRevB.78.180402. URL https://link.aps.org/doi/10.1103/PhysRevB.78.180402.

[77] M Foerster, F Rigato, K Bouzehouane, and J Fontcuberta. Tunnel transport through $CoFe_2O_4$ barriers investigated by conducting atomic force microscopy. *Journal of Physics D: Applied Physics*, 43(29):295001, jul 2010. doi: 10.1088/0022-3727/43/29/295001. URL https://doi.org/10.1088/0022-3727/43/29/295001.

[78] G. Hu and Y. Suzuki. Negative spin polarization of Fe_3O_4 in magnetite/manganite-based junctions. *Phys. Rev. Lett.*, 89:276601, Dec 2002. doi: 10.1103/PhysRevLett.89.276601. URL https://link.aps.org/doi/10.1103/PhysRevLett.89.276601.

[79] A. Pratt, M. Kurahashi, X. Sun, D. Gilks, and Y. Yamauchi. Direct observation of a positive spin polarization at the (111) surface of magnetite. *Phys. Rev. B*, 85:180409, May 2012. doi: 10.1103/PhysRevB.85.180409. URL https://link.aps.org/doi/10.1103/PhysRevB.85.180409.

[80] U. Lüders, M. Bibes, K. Bouzehouane, E. Jacquet, J.-P. Contour, S. Fusil, J.-F. Bobo, J. Fontcuberta, A. Barthélémy, and A. Fert. Spin filtering through ferrimagnetic $NiFe_2O_4$ tunnel barriers. *Applied Physics Letters*, 88(8):082505, 2006. doi: 10.1063/1.2172647. URL https://doi.org/10.1063/1.2172647.

[81] Y. Suzuki, R. B. van Dover, E. M. Gyorgy, Julia M. Phillips, V. Korenivski, D. J. Werder, C. H. Chen, R. J. Cava, J. J. Krajewski, W. F. Peck, and K. B. Do.

Structure and magnetic properties of epitaxial spinel ferrite thin films. *Applied Physics Letters*, 68(5):714–716, 1996. doi: 10.1063/1.116601. URL https://doi.org/10.1063/1.116601.

[82] Y.K. Fetisov, A.A. Bush, K.E. Kamentsev, A.Y. Ostashchenko, and G. Srinivasan. Ferrite-piezoelectric multilayers for magnetic field sensors. *IEEE Sensors Journal*, 6(4):935–938, 2006. doi: 10.1109/JSEN.2006.877989.

[83] G. Kh. Rozenberg, Y. Amiel, W. M. Xu, M. P. Pasternak, R. Jeanloz, M. Hanfland, and R. D. Taylor. Structural characterization of temperature- and pressure-induced inverse↔normal spinel transformation in magnetite. *Phys. Rev. B*, 75:020102, Jan 2007. doi: 10.1103/PhysRevB.75.020102. URL https://link.aps.org/doi/10.1103/PhysRevB.75.020102.

[84] P. Chandramohan, M.P. Srinivasan, S. Velmurugan, and S.V. Narasimhan. Cation distribution and particle size effect on raman spectrum of $CoFe_2O_4$. *Journal of Solid State Chemistry*, 184(1):89–96, 2011. ISSN 0022-4596. doi: https://doi.org/10.1016/j.jssc.2010.10.019. URL https://www.sciencedirect.com/science/article/pii/S0022459610004767.

[85] G. A. Sawatzky, F. VAN DER Woude, and A. H. Morrish. Cation distributions in octahedral and tetrahedral sites of the ferrimagnetic spinel $CoFe_2O_4$. *Journal of Applied Physics*, 39(2):1204–1205, 1968. doi: 10.1063/1.1656224. URL https://doi.org/10.1063/1.1656224.

[86] M. E. Fleet. The structure of magnetite: two annealed natural magnetites, $Fe_{3.005}O_4$ and $Fe_{2.96}Mg_{0.04}O_4$. *Acta Crystallographica Section C*, 40(9):1491–1493, Sep 1984. doi: 10.1107/S0108270184008489. URL https://doi.org/10.1107/S0108270184008489.

[87] Koichi Momma and Fujio Izumi. *VESTA3* for three-dimensional visualization of crystal, volumetric and morphology data. *Journal of Applied Crystallography*, 44 (6):1272–1276, Dec 2011. doi: 10.1107/S0021889811038970. URL https://doi.org/10.1107/S0021889811038970.

[88] E. W. Gorter. Magnetization in Ferrites: Saturation Magnetization of Ferrites with Spinel Structure. *Nature*, 165(4203):798–800, May 1950. ISSN 1476-4687. doi: 10.1038/165798a0. URL https://www.nature.com/articles/165798a0. Number: 4203 Publisher: Nature Publishing Group.

[89] H.A Kramers. L'interaction entre les atomes magnétogènes dans un cristal paramagnétique. *Physica*, 1(1):182–192, 1934. ISSN 0031-8914. doi: https://doi.org/10.

1016/S0031-8914(34)90023-9. URL https://www.sciencedirect.com/science/article/pii/S0031891434900239.

[90] P. W. Anderson. Antiferromagnetism. Theory of superexchange interaction. *Phys. Rev.*, 79:350–356, Jul 1950. doi: 10.1103/PhysRev.79.350. URL https://link.aps.org/doi/10.1103/PhysRev.79.350.

[91] Sam Jin Kim, Seung Wha Lee, and Chul Sung Kim. Mössbauer studies on exchange interactions in $CoFe_2O_4$. *Japanese Journal of Applied Physics*, 40(Part 1, No. 8): 4897–4902, aug 2001. doi: 10.1143/jjap.40.4897. URL https://doi.org/10.1143/jjap.40.4897.

[92] R. Kikuchi and John W. Cahn. Theory of interphase and antiphase boundaries in f.c.c. alloys. *Acta Metallurgica*, 27:1337–1353, 1979.

[93] James M. Howe. 14 - structure, composition and energy of solid–solid interfaces. In David E. Laughlin and Kazuhiro Hono, editors, *Physical Metallurgy (Fifth Edition)*, pages 1317–1451. Elsevier, Oxford, fifth edition edition, 2014. ISBN 978-0-444-53770-6. doi: https://doi.org/10.1016/B978-0-444-53770-6.00014-9. URL https://www.sciencedirect.com/science/article/pii/B9780444537706000149.

[94] W. Eerenstein, T. T. M. Palstra, S. S. Saxena, and T. Hibma. Spin-polarized transport across sharp antiferromagnetic boundaries. *Phys. Rev. Lett.*, 88:247204, Jun 2002. doi: 10.1103/PhysRevLett.88.247204. URL https://link.aps.org/doi/10.1103/PhysRevLett.88.247204.

[95] Amit V. Singh, Behrouz Khodadadi, Jamileh Beik Mohammadi, Sahar Keshavarz, Tim Mewes, Devendra Singh Negi, Ranjan Datta, Zbigniew Galazka, Reinhard Uecker, and Arunava Gupta. Bulk single crystal-like structural and magnetic characteristics of epitaxial spinel ferrite thin films with elimination of antiphase boundaries. *Advanced Materials*, 29(30):1701222, 2017. doi: https://doi.org/10.1002/adma.201701222. URL https://onlinelibrary.wiley.com/doi/abs/10.1002/adma.201701222.

[96] M. Luysberg, R. G. S. Sofin, S. K. Arora, and I. V. Shvets. Strain relaxation in $Fe_3O_4/MgAl_2O_4$ heterostructures: Mechanism for formation of antiphase boundaries in an epitaxial system with identical symmetries of film and substrate. *Phys. Rev. B*, 80:024111, Jul 2009. doi: 10.1103/PhysRevB.80.024111. URL https://link.aps.org/doi/10.1103/PhysRevB.80.024111.

[97] Keith P. McKenna, Florian Hofer, Daniel Gilks, Vlado K. Lazarov, Chunlin Chen, Zhongchang Wang, and Yuichi Ikuhara. Atomic-scale structure and properties of highly stable antiphase boundary defects in Fe_3O_4. *Nature Communications*,

5(1):5740, December 2014. ISSN 2041-1723. doi: 10.1038/ncomms6740. URL https://www.nature.com/articles/ncomms6740. Number: 1 Publisher: Nature Publishing Group.

[98] R. M. Bozorth, Elizabeth F. Tilden, and Albert J. Williams. Anisotropy and magnetostriction of some ferrites. *Phys. Rev.*, 99:1788–1798, Sep 1955. doi: 10.1103/PhysRev.99.1788. URL https://link.aps.org/doi/10.1103/PhysRev.99.1788.

[99] D.C. Jiles and C.C.H. Lo. The role of new materials in the development of magnetic sensors and actuators. *Sensors and Actuators A: Physical*, 106(1):3–7, 2003. ISSN 0924-4247. doi: https://doi.org/10.1016/S0924-4247(03)00255-3. URL https://www.sciencedirect.com/science/article/pii/S0924424703002553. Proceedings of the 4th European Magnetic Sensors and Actuators Conference.

[100] Z. Szotek, W. M. Temmerman, D. Ködderitzsch, A. Svane, L. Petit, and H. Winter. Electronic structures of normal and inverse spinel ferrites from first principles. *Phys. Rev. B*, 74:174431, Nov 2006. doi: 10.1103/PhysRevB.74.174431. URL https://link.aps.org/doi/10.1103/PhysRevB.74.174431.

[101] Y. Kitamoto, S. Kantake, F. Shirasaki, M. Abe, and M. Naoe. Co ferrite films with excellent perpendicular magnetic anisotropy and high coercivity deposited at low temperature. *Journal of Applied Physics*, 85(8):4708–4710, 1999. doi: 10.1063/1.370455. URL https://doi.org/10.1063/1.370455.

[102] A. Lisfi and C. M. Williams. Magnetic anisotropy and domain structure in epitaxial $CoFe_2O_4$ thin films. *Journal of Applied Physics*, 93(10):8143–8145, 2003. doi: 10.1063/1.1541651. URL https://doi.org/10.1063/1.1541651.

[103] W. Huang, L.X. Zhou, H.Z. Zeng, X.H. Wei, J. Zhu, Y. Zhang, and Y.R. Li. Epitaxial growth of the $CoFe_2O_4$ film on $SrTiO_3$ and its characterization. *Journal of Crystal Growth*, 300(2):426–430, 2007. ISSN 0022-0248. doi: https://doi.org/10.1016/j.jcrysgro.2007.01.004. URL https://www.sciencedirect.com/science/article/pii/S0022024807000619.

[104] B. H. Liu and J. Ding. Strain-induced high coercivity in $CoFe_2O_4$ powders. *Applied Physics Letters*, 88(4):042506, 2006. doi: 10.1063/1.2161808. URL https://doi.org/10.1063/1.2161808.

[105] C. Gatel, B. Warot-Fonrose, S. Matzen, and J.-B. Moussy. Magnetism of $CoFe_2O_4$ ultrathin films on $MgAl_2O_4$ driven by epitaxial strain. *Applied Physics Letters*, 103(9):092405, 2013. doi: 10.1063/1.4819178. URL https://doi.org/10.1063/1.4819178.

[106] A. Lisfi, C. M. Williams, L. T. Nguyen, J. C. Lodder, A. Coleman, H. Corcoran, A. Johnson, P. Chang, A. Kumar, and W. Morgan. Reorientation of magnetic anisotropy in epitaxial cobalt ferrite thin films. *Phys. Rev. B*, 76:054405, Aug 2007. doi: 10.1103/PhysRevB.76.054405. URL https://link.aps.org/doi/10.1103/PhysRevB.76.054405.

[107] S. Matzen, J.-B. Moussy, R. Mattana, F. Petroff, C. Gatel, B. Warot-Fonrose, J. C. Cezar, A. Barbier, M.-A. Arrio, and Ph. Sainctavit. Restoration of bulk magnetic properties by strain engineering in epitaxial $CoFe_2O_4$ (001) ultrathin films. *Applied Physics Letters*, 99(5):052514, 2011. doi: 10.1063/1.3622307. URL https://doi.org/10.1063/1.3622307.

[108] W. Huang, J. Zhu, H. Z. Zeng, X. H. Wei, Y. Zhang, and Y. R. Li. Strain induced magnetic anisotropy in highly epitaxial $CoFe_2O_4$ thin films. *Applied Physics Letters*, 89(26):262506, 2006. doi: 10.1063/1.2424444. URL https://doi.org/10.1063/1.2424444.

[109] Ze Zhang and Sashi Satpathy. Electron states, magnetism, and the verwey transition in magnetite. *Phys. Rev. B*, 44:13319–13331, Dec 1991. doi: 10.1103/PhysRevB.44.13319. URL https://link.aps.org/doi/10.1103/PhysRevB.44.13319.

[110] Stuart S. P. Parkin, Christian Kaiser, Alex Panchula, Philip M. Rice, Brian Hughes, Mahesh Samant, and See-Hun Yang. Giant tunnelling magnetoresistance at room temperature with MgO (100) tunnel barriers. *Nature Materials*, 3(12):862–867, December 2004. ISSN 1476-4660. doi: 10.1038/nmat1256. URL https://www.nature.com/articles/nmat1256. Number: 12 Publisher: Nature Publishing Group.

[111] Friedrich Walz. The verwey transition - a topical review. *Journal of Physics: Condensed Matter*, 14(12):R285–R340, mar 2002. doi: 10.1088/0953-8984/14/12/203. URL https://doi.org/10.1088/0953-8984/14/12/203.

[112] E. J. Verwey, P. W. Haayman, and F. C. Romeijn. Physical properties and cation arrangement of oxides with spinel structures ii. electronic conductivity. *The Journal of Chemical Physics*, 15(4):181–187, 1947. doi: 10.1063/1.1746466. URL https://doi.org/10.1063/1.1746466.

[113] J. P. Wright, J. P. Attfield, and P. G. Radaelli. Long range charge ordering in magnetite below the verwey transition. *Phys. Rev. Lett.*, 87:266401, Dec 2001. doi: 10.1103/PhysRevLett.87.266401. URL https://link.aps.org/doi/10.1103/PhysRevLett.87.266401.

[114] W. A. Yager, J. K. Galt, and F. R. Merritt. Ferromagnetic resonance in two nickel-iron ferrites. *Phys. Rev.*, 99:1203–1210, Aug 1955. doi: 10.1103/PhysRev.99.1203. URL https://link.aps.org/doi/10.1103/PhysRev.99.1203.

[115] Daniel Fritsch and Claude Ederer. First-principles calculation of magnetoelastic coefficients and magnetostriction in the spinel ferrites $CoFe_2O_4$ and $NiFe_2O_4$. *Phys. Rev. B*, 86:014406, Jul 2012. doi: 10.1103/PhysRevB.86.014406. URL https://link.aps.org/doi/10.1103/PhysRevB.86.014406.

[116] Ying Liu, Zhiheng Mei, Yizhong Guo, Peng Zhou, Yajun Qi, Kun Liang, Zhijun Ma, Zhengcai Xia, Amitava Adhikary, Cunzheng Dong, NianXiang Sun, Gopalan Srinivasan, and Tianjin Zhang. Evidence for strain control of magnetic anisotropy in epitaxial nickel ferrite thin films grown on strontium titanate substrates. *Materials Research Bulletin*, 138:111214, 2021. ISSN 0025-5408. doi: https://doi.org/10.1016/j.materresbull.2021.111214. URL https://www.sciencedirect.com/science/article/pii/S0025540821000118.

[117] S. Venzke, R. B. van Dover, Julia M. Phillips, E. M. Gyorgy, T. Siegrist, C-H. Chen, D. Werder, R. M. Fleming, R. J. Felder, E. Coleman, and et al. Epitaxial growth and magnetic behavior of $NiFe_2O_4$ thin films. *Journal of Materials Research*, 11 (5):1187–1198, 1996. doi: 10.1557/JMR.1996.0153.

[118] Chuanbin Wang, Shihang Liu, Junwei Shi, and Qiang Shen. Enhanced magnetic properties of $NiFe_2O_4$ thin films deposited on bczt-buffered $SrTiO_3$ substrate. *AIP Advances*, 12(4):045302, 2022. doi: 10.1063/5.0088002. URL https://doi.org/10.1063/5.0088002.

[119] Viktor E. Bursian, Andrey K. Kaveev, Alexander M. Korovin, Boris B. Krichevtsov, Leonid V. Lutsev, Sergey M. Suturin, Masahiro Sawada, and Nikolai S. Sokolov. Bulk-like dynamic magnetic properties of nickel ferrite epitaxial thin films grown on $SrTiO_3$(001) substrates. *IEEE Magnetics Letters*, 10:1–5, 2019. doi: 10.1109/LMAG.2019.2930597.

[120] Panagiota Bougiatioti, Orestis Manos, Christoph Klewe, Daniel Meier, Niclas Teichert, Jan-Michael Schmalhorst, Timo Kuschel, and Günter Reiss. Electrical transport and optical band gap of nife2ox thin films. *Journal of Applied Physics*, 122 (22):225101, 2017. doi: 10.1063/1.4999428. URL https://doi.org/10.1063/1.4999428.

[121] Ž. Cvejić, E. urić, G. Ivković Ivandekić, B. Bajac, P. Postolache, L. Mitoseriu, V.V. Srdić, and S. Rakić. The effect of annealing on microstructure and cation distribution of $NiFe_2O_4$. *Journal of Alloys and Compounds*, 649:1231–1238, 2015.

ISSN 0925-8388. doi: https://doi.org/10.1016/j.jallcom.2015.07.238. URL https://www.sciencedirect.com/science/article/pii/S0925838815306368.

[122] Y. Suzuki, R. B. van Dover, E. M. Gyorgy, Julia M. Phillips, and R. J. Felder. Exchange coupling in single-crystalline spinel-structure (Mn,Zn)Fe_2O_4/$CoFe_2O_4$ bilayers. *Phys. Rev. B*, 53:14016–14019, Jun 1996. doi: 10.1103/PhysRevB.53.14016. URL https://link.aps.org/doi/10.1103/PhysRevB.53.14016.

[123] Detian Yang, Yu Yun, Arjun Subedi, Nicholas E. Rogers, David M. Cornelison, Peter A. Dowben, and Xiaoshan Xu. Colossal intrinsic exchange bias from interfacial reconstruction in epitaxial $CoFe_2O_4$/Al_2O_3 thin films. *Physical Review B*, 103(22), jun 2021. doi: 10.1103/physrevb.103.224405. URL https://doi.org/10.1103%2Fphysrevb.103.224405.

[124] P. A. A. van der Heijden, P. J. H. Bloemen, J. M. Metselaar, R. M. Wolf, J. M. Gaines, J. T. W. M. van Eemeren, P. J. van der Zaag, and W. J. M. de Jonge. Interlayer coupling between Fe_3O_4 layers separated by an insulating nonmagnetic MgO layer. *Phys. Rev. B*, 55:11569–11575, May 1997. doi: 10.1103/PhysRevB.55.11569. URL https://link.aps.org/doi/10.1103/PhysRevB.55.11569.

[125] Ji Wang, Chen Chen, Biao Xu, Qingyu Xu, Ruobai Liu, Yuan Yuan, Linao Huang, Tianyu Liu, Lujun Wei, Biao You, Wei Zhang, and Jun Du. Temperature dependence of exchange bias in $NiFe_2O_4$/$BiFeO_3$ bilayers. *Applied Surface Science*, 517:146165, 2020. ISSN 0169-4332. doi: https://doi.org/10.1016/j.apsusc.2020.146165. URL https://www.sciencedirect.com/science/article/pii/S0169433220309211.

[126] Mikko Ritala and Markku Leskelä. Chapter 2 - atomic layer deposition. In Hari Singh Nalwa, editor, *Handbook of Thin Films*, pages 103–159. Academic Press, Burlington, 2002. ISBN 978-0-12-512908-4. doi: https://doi.org/10.1016/B978-012512908-4/50005-9. URL https://www.sciencedirect.com/science/article/pii/B9780125129084500059.

[127] Milton Ohring. Chapter 6 - chemical vapor deposition. In Milton Ohring, editor, *Materials Science of Thin Films (Second Edition)*, pages 277–355. Academic Press, San Diego, second edition edition, 2002. ISBN 978-0-12-524975-1. doi: https://doi.org/10.1016/B978-012524975-1/50009-4. URL https://www.sciencedirect.com/science/article/pii/B9780125249751500094.

[128] Floriana Craciun, Thomas Lippert, and Maria Dinescu. *Pulsed Laser Deposition: Fundamentals, Applications, and Perspectives*, pages 1–33. Springer International Publishing, Cham, 2020. ISBN 978-3-319-69537-2. doi: 10.1007/

978-3-319-69537-2_27-2. URL https://doi.org/10.1007/978-3-319-69537-2_27-2.

[129] Hartmut Zabel, Katharina Theis-Bröhl, and Boris P. Toperverg. *Polarized Neutron Reflectivity and Scattering from Magnetic Nanostructures and Spintronic Materials*. John Wiley and Sons, Ltd, 2007. ISBN 9780470022184. doi: https://doi.org/10.1002/9780470022184.hmm303. URL https://onlinelibrary.wiley.com/doi/abs/10.1002/9780470022184.hmm303.

[130] Boris P. Toperverg and Hartmut Zabel. Chapter 6 - neutron scattering in nanomagnetism. In Felix Fernandez-Alonso and David L. Price, editors, *Neutron Scattering - Magnetic and Quantum Phenomena*, volume 48 of *Experimental Methods in the Physical Sciences*, pages 339–434. Academic Press, 2015. doi: https://doi.org/10.1016/B978-0-12-802049-4.00006-3. URL https://www.sciencedirect.com/science/article/pii/B9780128020494000063.

[131] F. Mezei. La nouvelle vague in polarized neutron scattering. *Physica B+C*, 137(1):295–308, 1986. ISSN 0378-4363. doi: https://doi.org/10.1016/0378-4363(86)90335-9. URL https://www.sciencedirect.com/science/article/pii/0378436386903359.

[132] Frédéric Ott. Neutron surface scattering. Application to magnetic thin films. *École thématique de la Société Française de la Neutronique*, 13:02004, 2014. ISSN 2107-7223, 2107-7231. doi: 10.1051/sfn/20141302004. URL http://www.neutron-sciences.org/10.1051/sfn/20141302004.

[133] Thomas Saerbeck. Chapter three - magnetic exchange phenomena probed by neutron scattering. volume 65 of *Solid State Physics*, pages 237–352. Academic Press, 2014. doi: https://doi.org/10.1016/B978-0-12-800175-2.00003-0. URL https://www.sciencedirect.com/science/article/pii/B9780128001752000030.

[134] G. L. Squires. *Introduction to the Theory of Thermal Neutron Scattering*, page 1–9. Cambridge University Press, 3rd edition, 2012. doi: 10.1017/CBO9781139107808.002.

[135] Kevin Yager. Neutron scattering lengths. http://gisaxs.com/index.php?title=File:Output-elements.png&oldid=401/, 2014. URL http://gisaxs.com/index.php?title=File:Output-elements.png&oldid=401.

[136] B.L. Henke, E.M. Gullikson, and J.C. Davis. X-ray interactions: Photoabsorption, scattering, transmission, and reflection at e = 50-30,000 ev, z = 1-92. *Atomic Data and Nuclear Data Tables*, 54(2):181–342, 1993. ISSN 0092-640X. doi: https://doi.

org/10.1006/adnd.1993.1013. URL https://www.sciencedirect.com/science/article/pii/S0092640X83710132.

[137] U. W. Arndt, D. C. Creagh, R. D. Deslattes, J. H. Hubbell, P. Indelicato, E. G. Kessler, and E. Lindroth. *X-rays*, chapter 4.2, pages 191–258. John Wiley Sons, Ltd, 2006. ISBN 9780470685754. doi: https://doi.org/10.1107/97809553602060000592. URL https://onlinelibrary.wiley.com/doi/abs/10.1107/97809553602060000592.

[138] C. Fermon, F. Ott, and A. Menelle. *Neutron Reflectometry*, pages 183–234. Springer Berlin Heidelberg, Berlin, Heidelberg, 2009. ISBN 978-3-540-88588-7. doi: 10.1007/978-3-540-88588-7_5. URL https://doi.org/10.1007/978-3-540-88588-7_5.

[139] D. S. Sivia. 93 Surfaces, interfaces and reflectivity. In *Elementary Scattering Theory: For X-ray and Neutron Users*. Oxford University Press, 01 2011. ISBN 9780199228676. doi: 10.1093/acprof:oso/9780199228676.003.0004. URL https://doi.org/10.1093/acprof:oso/9780199228676.003.0004.

[140] D. S. Sivia. 63 The basics of X-ray and neutron scattering. In *Elementary Scattering Theory: For X-ray and Neutron Users*. Oxford University Press, 01 2011. ISBN 9780199228676. doi: 10.1093/acprof:oso/9780199228676.003.0003. URL https://doi.org/10.1093/acprof:oso/9780199228676.003.0003.

[141] Landau Lev Davidovic, Lifsic Evgenij M., and Landau Lev Davidovic. *The classical theory of Fields*. Pergamon Press, 1975.

[142] G. P. Felcher, R. O. Hilleke, R. K. Crawford, J. Haumann, R. Kleb, and G. Ostrowski. Polarized neutron reflectometer: A new instrument to measure magnetic depth profiles. *Review of Scientific Instruments*, 58(4):609–619, 1987. doi: 10.1063/1.1139225. URL https://doi.org/10.1063/1.1139225.

[143] C.F. Majkrzak. Polarized neutron scattering methods and studies involving artificial superlattices. *Physica B: Condensed Matter*, 156-157:619–626, 1989. ISSN 0921-4526. doi: https://doi.org/10.1016/0921-4526(89)90748-5. URL https://www.sciencedirect.com/science/article/pii/0921452689907485.

[144] C.F. Majkrzak. Polarized neutron reflectometry. *Physica B: Condensed Matter*, 173(1):75–88, 1991. ISSN 0921-4526. doi: https://doi.org/10.1016/0921-4526(91)90037-F. URL https://www.sciencedirect.com/science/article/pii/092145269190037F.

[145] Varley F. Sears. Neutron scattering lengths and cross sections. *Neutron News*, 3 (3):26–37, 1992. doi: 10.1080/10448639208218770. URL https://doi.org/10.1080/10448639208218770.

[146] L. Névot and P. Croce. Caractérisation des surfaces par réflexion rasante de rayons X. Application à l'étude du polissage de quelques verres silicates. *Revue de Physique Appliquée*, 15(3):761–779, March 1980. ISSN 0035-1687, 2777-3671. doi: 10.1051/rphysap:01980001503076100. URL http://dx.doi.org/10.1051/rphysap:01980001503076100. Publisher: Société Française de Physique.

[147] M. Björck and G. Andersson. *J. Appl. Cryst.*, 2007. URL http://genx.sf.net.

[148] Thomas Saerbeck, Robert Cubitt, Andrew Wildes, Giuliana Manzin, Ken H. Andersen, and Philipp Gutfreund. Recent upgrades of the neutron reflectometer D17 at ILL. *Journal of Applied Crystallography*, 51(2):249–256, Apr 2018. doi: 10.1107/S160057671800239X. URL https://doi.org/10.1107/S160057671800239X.

[149] R. Cubitt and G. Fragneto. D17: the new reflectometer at the ILL. *Applied Physics A*, 74(1):s329–s331, December 2002. ISSN 1432-0630. doi: 10.1007/s003390201611. URL https://doi.org/10.1007/s003390201611.

[150] Alexei Vorobiev, Anton Devishvilli, Gunnar Palsson, Håkan Rundlöf, Niklas Johansson, Anders Olsson, Andrew Dennison, Max Wollf, Benjamin Giroud, Olivier Aguettaz, and Björgvin Hjörvarsson. Recent upgrade of the polarized neutron reflectometer super adam. *Neutron News*, 26(3):25–26, 2015. doi: 10.1080/10448632.2015.1057054. URL https://doi.org/10.1080/10448632.2015.1057054.

[151] A. Stunault, K.H. Andersen, S. Roux, T. Bigault, K. Ben-Saidane, and H.M. Rønnow. New solid state polarizing bender for cold neutrons. *Physica B: Condensed Matter*, 385-386:1152–1154, 2006. ISSN 0921-4526. doi: https://doi.org/10.1016/j.physb.2006.05.396. URL https://www.sciencedirect.com/science/article/pii/S0921452606012877.

[152] Philipp Gutfreund, Thomas Saerbeck, Miguel A. Gonzalez, Eric Pellegrini, Mark Laver, Charles Dewhurst, and Robert Cubitt. Towards generalized data reduction on a chopper-based time-of-flight neutron reflectometer. *Journal of Applied Crystallography*, 51(3):606–615, Jun 2018. doi: 10.1107/S160057671800448X. URL https://doi.org/10.1107/S160057671800448X.

[153] GitHub - Alexey-Klechikov/pySAred: SuperADAM hdf5 files reduction software. URL https://github.com/Alexey-Klechikov/pySAred.

[154] Giuseppe Iadonisi, Giovanni Cantele, and Maria Luisa Chiofalo. *Crystals and Nanosystems Structure*, pages 1–96. Springer Milan, Milano, 2014. ISBN 978-88-470-2805-0. doi: 10.1007/978-88-470-2805-0_1. URL https://doi.org/10.1007/978-88-470-2805-0_1.

[155] B Warren. *X-ray diffraction*. Addison-Wesley, 1969.

[156] *Diffraction by perfect crystals*, chapter 6, pages 207–238. John Wiley Sons, Ltd, 2011. ISBN 9781119998365. doi: https://doi.org/10.1002/9781119998365.ch6. URL https://onlinelibrary.wiley.com/doi/abs/10.1002/9781119998365.ch6.

[157] JOHN M. COWLEY. Chapter 8 - diffraction by perfect crystals. In JOHN M. COWLEY, editor, *Diffraction Physics (Third Edition)*, North-Holland Personal Library, pages 167–187. North-Holland, Amsterdam, third edition edition, 1995. doi: https://doi.org/10.1016/B978-044482218-5/50010-9. URL https://www.sciencedirect.com/science/article/pii/B9780444822185500109.

[158] B. Ingham and M.F. Toney. 1 - x-ray diffraction for characterizing metallic films. In Katayun Barmak and Kevin Coffey, editors, *Metallic Films for Electronic, Optical and Magnetic Applications*, pages 3–38. Woodhead Publishing, 2014. ISBN 978-0-85709-057-7. doi: https://doi.org/10.1533/9780857096296.1.3. URL https://www.sciencedirect.com/science/article/pii/B9780857090577500012.

[159] George Harrington and José Santiso. Back-to-basics tutorial: X-ray diffraction of thin films. *Journal of Electroceramics*, 47:1–23, 12 2021. doi: 10.1007/s10832-021-00263-6.

[160] Dmitri Litvinov, Thomas O'Donnell, and Roy Clarke. In situ thin-film texture determination. *Journal of Applied Physics*, 85(4):2151–2156, 1999. doi: 10.1063/1.369519. URL https://doi.org/10.1063/1.369519.

[161] I. K. Robinson. Crystal truncation rods and surface roughness. *Phys. Rev. B*, 33:3830–3836, Mar 1986. doi: 10.1103/PhysRevB.33.3830. URL https://link.aps.org/doi/10.1103/PhysRevB.33.3830.

[162] Aaron M. Miller, Mellie Lemon, Marisa A. Choffel, Sarah R. Rich, Fischer Harvel, and David C. Johnson. Extracting information from x-ray diffraction patterns containing laue oscillations. *Zeitschrift für Naturforschung B*, 77(4-5):313–322, 2022. doi: doi:10.1515/znb-2022-0020. URL https://doi.org/10.1515/znb-2022-0020.

[163] Enrico Schierle. *Antiferromagnetism in Thin Films Studied by Resonant Magnetic Soft X-Ray Scattering*. PhD thesis, 2007. URL http://dx.doi.org/10.17169/refubium-11239.

[164] P Scherrer. Nachrichten von der königlichen gesellschaft der wissenschaft zu. *Göttingen, Mathematisch-physikalische Klasse*, 1:98, 1918.

[165] S. N. Danilchenko, O. G. Kukharenko, C. Moseke, I. Yu. Protsenko, L. F. Sukhodub, and B. Sulkio-Cleff. Determination of the bone mineral crystallite size and lattice strain from diffraction line broadening. *Crystal Research and Technology*, 37(11):1234–1240, 2002. doi: https://doi.org/10.1002/1521-4079(200211)37:11⟨1234::AID-CRAT1234⟩3.0.CO;2-X. URL https://onlinelibrary.wiley.com/doi/abs/10.1002/1521-4079%28200211%2937%3A11%3C1234%3A%3AAID-CRAT1234%3E3.0.CO%3B2-X.

[166] Hosein Kafashan. X-ray Diffraction Line Profile Analysis of Undoped and Se-Doped SnS Thin Films Using Scherrer's, Williamson–Hall and Size–Strain Plot Methods. *Journal of Electronic Materials*, 48(2):1294–1309, February 2019. ISSN 1543-186X. doi: 10.1007/s11664-018-6791-7. URL https://doi.org/10.1007/s11664-018-6791-7.

[167] J. I. Langford and A. J. C. Wilson. Scherrer after sixty years: A survey and some new results in the determination of crystallite size. *Journal of Applied Crystallography*, 11(2):102–113, Apr 1978. doi: 10.1107/S0021889878012844. URL https://doi.org/10.1107/S0021889878012844.

[168] Ahmad Monshi, Mohammad Reza Foroughi, and Mohammad Reza Monshi. Modified scherrer equation to estimate more accurately nano-crystallite size using xrd. *World J Nano Sci Eng, 2012, 2: 154*, 160, 2012. doi: 10.4236/wjnse.2012.23020.

[169] Simon Foner. Versatile and sensitive vibrating-sample magnetometer. *Review of Scientific Instruments*, 30(7):548–557, 1959. doi: 10.1063/1.1716679. URL https://doi.org/10.1063/1.1716679.

[170] Michael Faraday. V. experimental researches in electricity. *Philosophical Transactions of the Royal Society of London*, 122:125–162, 1832. doi: 10.1098/rstl.1832.0006. URL https://royalsocietypublishing.org/doi/abs/10.1098/rstl.1832.0006.

[171] Randy K. Dumas and Tom Hogan. *Recent Advances in SQUID Magnetometry*, pages 39–62. Springer International Publishing, Cham, 2021. ISBN 978-3-030-70443-8. doi: 10.1007/978-3-030-70443-8_3. URL https://doi.org/10.1007/978-3-030-70443-8_3.

[172] Caroline A. Schneider, Wayne S. Rasband, and Kevin W. Eliceiri. NIH Image to ImageJ: 25 years of image analysis. *Nature Methods*, 9(7):671–675, July 2012. ISSN 1548-7105. doi: 10.1038/nmeth.2089. URL https://www.nature.com/articles/nmeth.2089. Number: 7 Publisher: Nature Publishing Group.

[173] Fabio Luis Zabotto, Alexandre José Gualdi, Jose Antonio Eiras, Adilson Jesus Aparecido de Oliveira, and Ducinei Garcia. Influence of the sintering temperature on the magnetic and electric properties of $NiFe_2O_4$ ferrites. *Materials Research*, 15(3):428–433, May 2012. ISSN 1980-5373, 1516-1439. doi: 10.1590/S1516-14392012005000043. URL http://www.scielo.br/scielo.php?script=sci_arttext&pid=S1516-14392012000300014&lng=en&tlng=en.

[174] Mariona Coll, Josep M. Montero Moreno, Jaume Gazquez, Kornelius Nielsch, Xavier Obradors, and Teresa Puig. Low temperature stabilization of nanoscale epitaxial spinel ferrite thin films by atomic layer deposition. *Advanced Functional Materials*, 24(34):5368–5374, 2014. doi: https://doi.org/10.1002/adfm.201400517. URL https://onlinelibrary.wiley.com/doi/abs/10.1002/adfm.201400517.

[175] J.C. Slonczewski. Magnetocrystalline anisotropy of cobalt-substituted manganese ferrite. *Journal of Physics and Chemistry of Solids*, 18(2):269–271, 1961. ISSN 0022-3697. doi: https://doi.org/10.1016/0022-3697(61)90178-0. URL https://www.sciencedirect.com/science/article/pii/0022369761901780.

[176] Lance Horng, G Chern, M.C Chen, P.C Kang, and D.S Lee. Magnetic anisotropic properties in Fe_3O_4 and $CoFe_2O_4$ ferrite epitaxy thin films. *Journal of Magnetism and Magnetic Materials*, 270(3):389–396, 2004. ISSN 0304-8853. doi: https://doi.org/10.1016/j.jmmm.2003.09.005. URL https://www.sciencedirect.com/science/article/pii/S0304885303007388.

[177] Chengxi Zhao, Anming Gao, Yansong Yang, Cheng Tu, Ankita Bhutani, Kathy A. Walsh, Songbin Gong, and Daniel P. Shoemaker. High-quality $CoFe_2O_4$ thin films with large coercivity grown via a wet chemical route. *AIP Advances*, 9(3):035126, 2019. doi: 10.1063/1.5085232. URL https://doi.org/10.1063/1.5085232.

[178] J.G.S. Duque, E.A. Souza, C.T. Meneses, and L. Kubota. Magnetic properties of $NiFe_2O_4$ nanoparticles produced by a new chemical method. *Physica B: Condensed Matter*, 398(2):287–290, 2007. ISSN 0921-4526. doi: https://doi.org/10.1016/j.physb.2007.04.030. URL https://www.sciencedirect.com/science/article/pii/S0921452607002980.

[179] M. Grigorova, H.J. Blythe, V. Blaskov, V. Rusanov, V. Petkov, V. Masheva, D. Nihtianova, Ll.M. Martinez, J.S. Muñoz, and M. Mikhov. Magnetic properties and mössbauer spectra of nanosized $CoFe_2O_4$ powders. *Journal of Magnetism and Magnetic Materials*, 183(1):163–172, 1998. ISSN 0304-8853. doi: https://doi.org/10.1016/S0304-8853(97)01031-7. URL https://www.sciencedirect.com/science/article/pii/S0304885397010317.

[180] F. Rigato, J. Geshev, V. Skumryev, and J. Fontcuberta. The magnetization of epitaxial nanometric $CoFe_2O_4$(001) layers. *Journal of Applied Physics*, 106 (11):113924, 2009. doi: 10.1063/1.3267873. URL https://doi.org/10.1063/1.3267873.

Appendix A

$NiFe_2O_4$ lower layer thickness invesitgation

Following the thickness-dependent effects observed in the bilayer in Chapter 4, we have begun a new investigation into how lowering the thickness of the bottom layer of the bilayer will affect the magnetic properties of the individual layers and bilayer overall. Here we present some preliminary results into new bilayers, meaning several key measurements are missing and we do not make a lengthy analysis. New bilayers C27N8 CFO (268 Å ± 12 Å)/NFO (79 Å ± 6 Å) /ALO[001] and C21N4 CFO (212 Å ± 1 Å)/ NFO (212 Å ± 3 Å)/ALO[001] have been grown.

XRD on C27N8 and C21N4 can is shown in figure A.1. Only NFO and CFO [111] sample Bragg peaks were present in the measured 2θ range, showing all films are [111] orientated along the surface normal and not amorphous or polycrystalline.

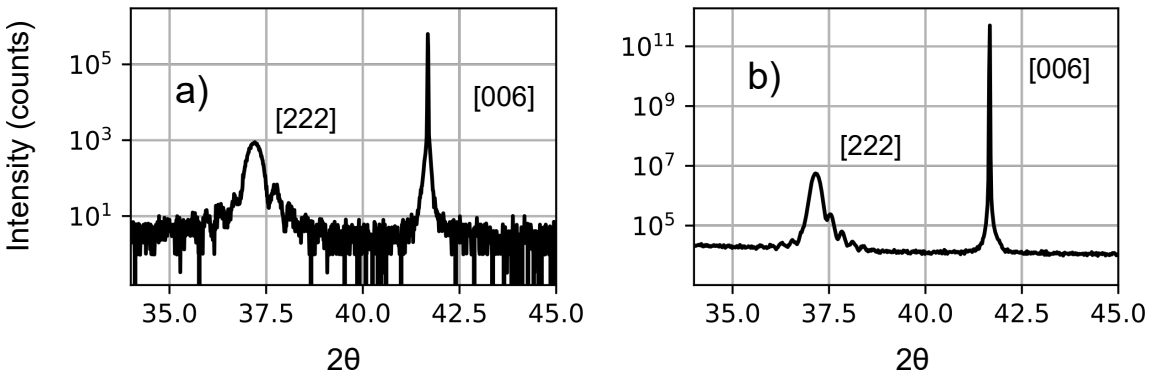

Figure A.1: XRD performed on C27N8 a) and C21N4 b)

CFO and NFO have bulk lattice parameters of a_{CFO}= 8.383 Å [14] and a_{NFO}=8.346 Å [15], with expected [222] Bragg peaks of $2\theta_{CFO} = 37.123°$ and $2\theta_{NFO} = 37.292°$. Using the Bragg scattering equation, described in section 2.3.4, with Miller indices of [h k l] = [2 2 2] for a cubic system and a copper x-ray source of λ=1.5406 Å, we have calculated the lattice constants of the films. To estimate the strain, $\epsilon = \frac{\Delta d}{d} \times 100$, of the films from the

fitted peak values, we have calculated the expected lattice constant based on the ratio of CFO and NFO in the films. We calculate the measured lattice constant of C21N4 as 8.367 Å ± 0.001 Å. The calculated expected lattice constant for C21N4 is 8.377 Å, giving a strain of -0.120 %. C27N8 showed a measured lattice constant of 8.375 Å ± 0.001 Å, with an expected lattice constant of 8.375 Å, showing a strain of 0.007 %.

Figures A.2 and A.3 show fitted XRR and PNR profiles from C27N8 and C21N4, at room temperature (RT) for XRR and 5 K for PNR, as a function of momentum transfer Q_z. For C27N8 the best and most simple model was, starting from the substrate, a layer of NFO, a layer of CFO and a surface layer. For N27C26 the best and most simple model was, starting from the substrate, a layer of CFO, then a layer of NFO. Both models were fitted with five independent regions of magnetization. In C27N8s model, two regions of magnetic freedom were given to the NFO layer, two to the CFO layer and one to the surface. In C21N4s model, two regions of magnetic freedom were given to the NFO layer, and three were given to the CFO layer to give an equivalent level of freedom between C27N8 and C21N4 models. Both samples were measured after field reversal to -3 T.

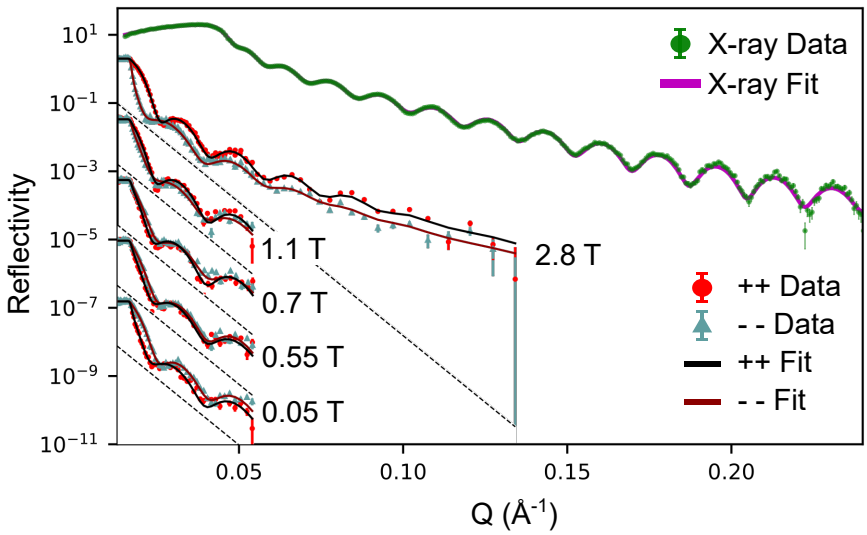

Figure A.2: PNR and XRR performed on C27N8. PNR was performed at 5 K at 2.8T and then after field reversal at 3 T, between 0.05 T to 1.1 T

Figures A.4 and A.5 show modelled M and N-SLD profiles of C27N8 and C21N4.

Tabel A.1 shows layer thickness, RMS roughness, N-SLD and M-SLD from the refined models of C27N8 and C21N4.

One immediate interesting result is that the magnetic gradient in NFO in C19N21 during magnetic switching, discussed in Chapter 4, is present in NFO in C21N4 and C27N21. Figure A.6 shows a comparison of these bilayers at 5 K and after field reversal, at 0.55 T. It can be seen that the magnetisation gradient in NFO goes throughout the NFO layer in C21N4 and C27N8, but relaxes in C19N21.

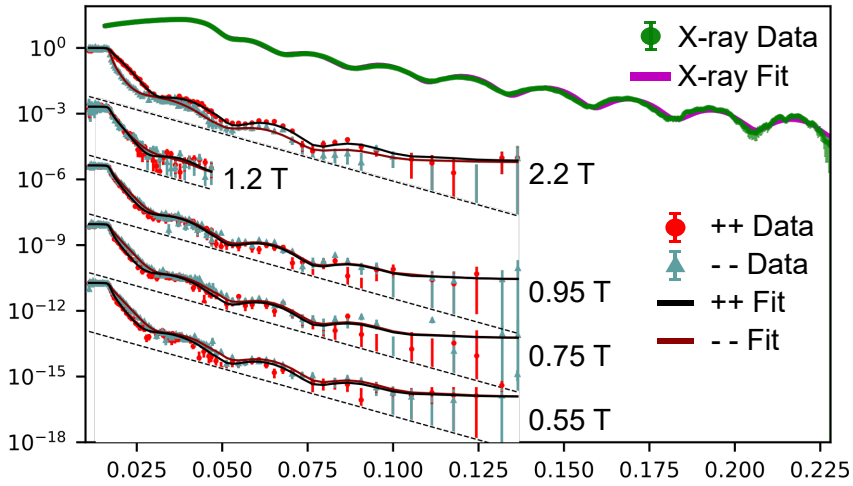

Figure A.3: PNR and XRR performed on C21N4. PNR was performed at 5 K at 2.2T and then after field reversal at 3 T, between 0.55 T to 1.2 T

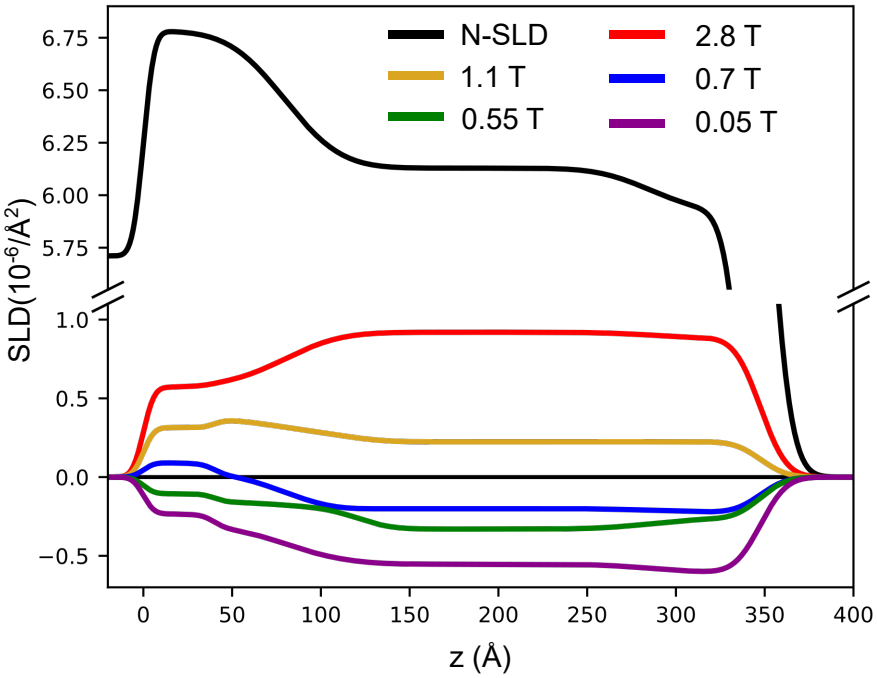

Figure A.4: Modelled N and M-SLD of C27N8 at 2.8 T and after field reversal at 3 T, between 0.05 T to 1.1 T

Sample	Material	Thickness (Å)	σ (Å)	NSLD (10^{-6}/Å^2)	M-SLD (10^{-6}/Å^2)
C27N8	NFO	79 ± 6	25 ± 6	6.77± 0.04	0.569± 0.098
	CFO	205.9 ± 12	15 ± 1	6.15 ± 0.03	0.920± 0.029
C21N4	NFO	40 ± 1	8.82 ± 6	6.66 ± 0.01	0.496± 0.051
	CFO	267.7± 3	15 ± 1	6.09 ± 0.03	0.803± 0.022

Table A.1: Layer thickness, RMS roughness, NSLD and M-SLD of C27N8 and C21N4

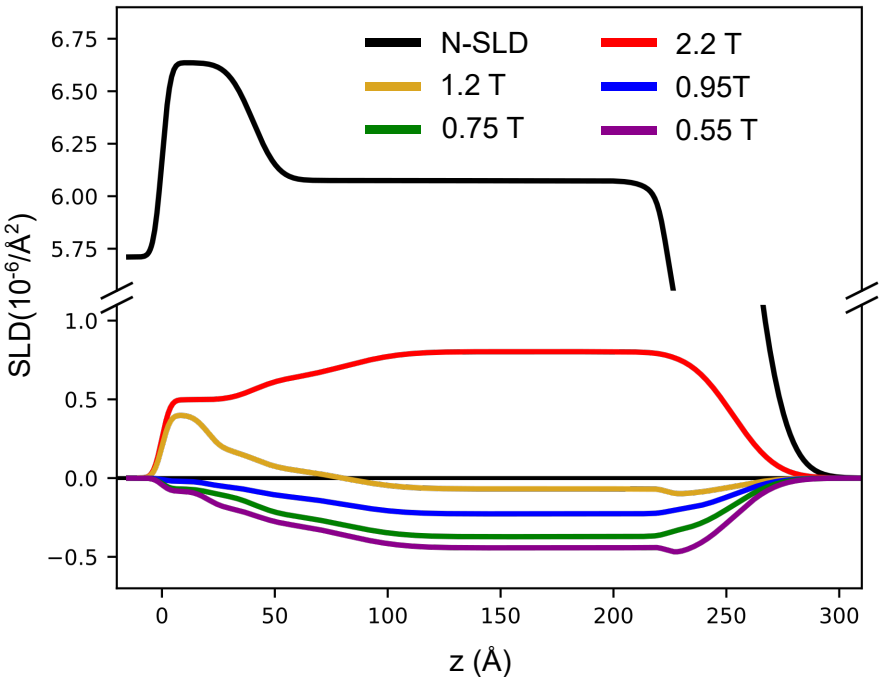

Figure A.5: Modelled N and M-SLD of C27N8 at 2.2 T and after field reversal at 3 T, between 0.55 T to 1.1 T

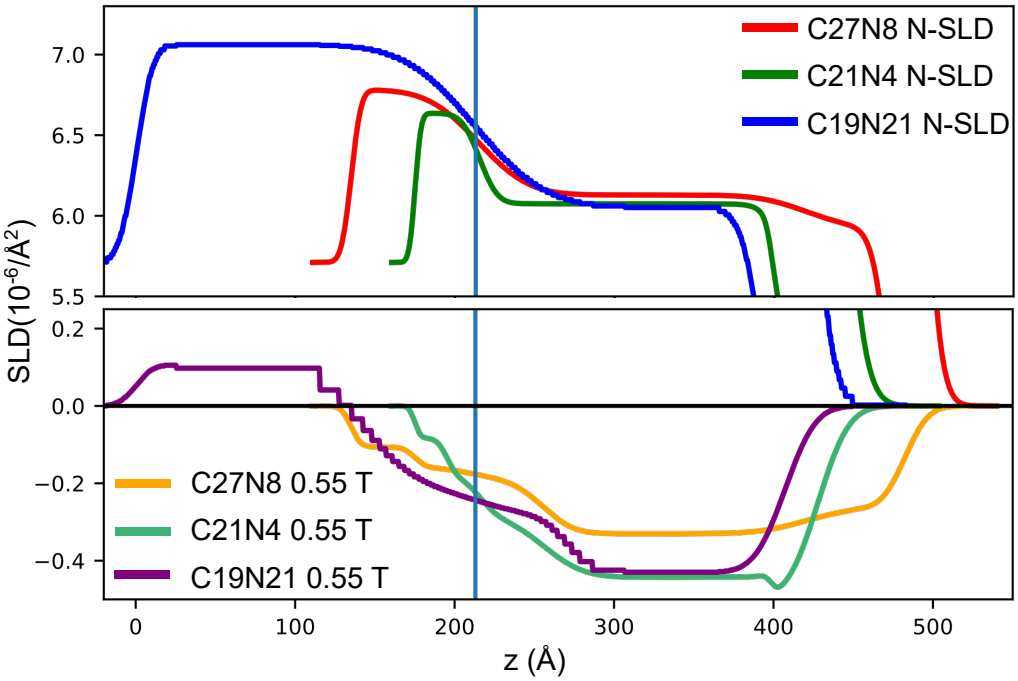

Figure A.6: N and M-SLD profiles of C19N21, C21N4 and C27N8 measured at 5 K and 0.55 T after field reversal.